

**SYSTEM-LEVEL INTERACTIONS BETWEEN ROCKING WALLS
AND HOLLOW-CORE SLABS**

**SYSTEM-LEVEL INTERACTIONS BETWEEN ROCKING WALLS
AND HOLLOW-CORE SLABS**

By

Oscar Camarillo Garduño

B.Eng.

A Thesis Submitted to the School of Graduate Studies in Partial Fulfilment of the
Requirements for the Degree of Master of Applied Science

Master of Applied Science (2022)
(Civil Engineering)

McMaster University
Hamilton, Ontario, Canada

TITLE: SYSTEM-LEVEL INTERACTIONS BETWEEN
ROCKING WALLS AND HOLLOW-CORE
SLABS

AUTHOR: Oscar Camarillo Garduño

SUPERVISORS: Dr. Lydell Andree Wiebe
Dr. Mohamed Ezzeldin

PAGES: 142 pages (xiii,128)

Abstract

Conventional fixed base walls are typically characterized by yielding that results in permanent damage, residual drifts and costly losses due to the service shutdown for structural repairs. Controlled rocking masonry walls have been developed as a solution to prevent structural damage when seismic events take place. These systems purposely allow the wall to rock from its foundation and have an uplift at the base, thus replacing the typical yielding at the base of conventional fixed-base walls. Controlled rocking masonry walls have traditionally been controlled by using unbonded post-tensioning strands to provide the self-centering behaviour. Although post-tensioning has shown favourable results, its implementation is difficult in practical applications, and post-tensioning losses due to yielding of the strands at large deformations can reduce their self-centering ability. In order to overcome such issues, an alternative controlled rocking system for masonry walls was developed recently, which is designed to self-center through vertical gravity loads only, instead of the post-tensioning tendons. The rocking response of this alternative system is controlled by using energy dissipation devices, so the system is referred to as Energy Dissipation-Controlled Rocking Masonry Walls (ED-CRMWs). The vertical gravity loads are primarily transferred to the ED-CRMWs from the floor slab at each level. Therefore, the wall-slab interaction should be investigated in order to ensure a fully resilient system.

In this regard, the current study identifies and categorizes the potential issues that are expected to occur due to the interaction between the wall rocking mechanism and the floor slab, and then investigates the most common of these issues using a parametric study. The parametric study focuses on the vertical incompatibility of displacements that a hollow-core slab suffers when its supporting walls uplift by different displacements during seismic events. Three different spans, four different cross-sections and two different alternatives of prestress configurations are considered in this study. The models were developed using ABAQUS 6.18 commercial software. The results show the cracking/yielding behaviour of the slabs and their displacement capacities at five different stages. The obtained results are promising for the usage of hollow-core slabs on ED-CRMWs or similar systems that require this interaction, as the range of displacement capacities can accommodate many of the vertical displacement incompatibilities expected in many potential situations.

Acknowledgments

I truly feel lucky to have been supervised by Dr. Lydell Wiebe and Dr. Mohamed Ezzeldin, for their endless support and their undeniably high standards. Thanks for all the given observations, questions, and advice.

I would not have been where I am today if it weren't for my parents, Oscar Camarillo Ledezma and Fabiola Garduño Trejo, and my brother Eduardo Camarillo Garduño. I will be eternally thankful for the inexhaustible support and love that they can provide all the way from Mexico. I have learned the best from each of them and all my achievements are a complex reflection formed by specific qualities of each of them.

(Spanish version)

Me siento verdaderamente afortunado de haber sido supervisado por Dr. Lydell Wiebe y Dr. Mohamed Ezzeldin, y me siento agradecido por su interminable apoyo y sus innegables altos estándares. Muchas gracias por todas las observaciones, preguntas y consejos que me dieron.

Yo no estaría donde estoy hoy si no fuera por mis padres, Oscar Camarillo Ledezma y Fabiola Garduño Trejo, y por mi hermano Eduardo Camarillo Garduño. Estaré eternamente agradecido por su incasable apoyo y amor que me han dado desde México. He aprendido lo mejor de cada uno de ellos y mis éxitos son el reflejo conformado por específicas cualidades de cada uno de ellos.

Table of Contents

Abstract.....	iii
Acknowledgements	iv
Table of Contents	v
List of Figures.....	vii
List of Tables	xii
Declaration of Academic Achievement	xiii
Chapter 1: Introduction and literature review.....	1
1.1 Introduction	1
1.2 Hollow-core Slab.....	3
1.3 Diaphragm-Wall Interaction.....	4
1.4 Masonry Diaphragm-Wall Connections.....	6
1.4.1 Precast Hollow-core Slab to Wall Fixed Connection	6
1.4.2 Cast-in-place to Wall Connection	9
1.5 Previous Studies of Rocking Wall Systems With a Focus on the Diaphragm- Wall Interaction.....	10
1.5.1 Shake-table Tests of Confined-masonry Rocking Walls With Supplementary Hysteretic Damping (Toranzo et al. 2009).....	10
1.5.2 Self-centering Precast Concrete Walls for Buildings in Regions With Low to High Seismicity (Henry 2011).....	14
1.5.3 Study on Interaction between Rocking-Wall System and Surrounding Structure (Liu 2016)	16
1.6 Previous Studies on Finite Element Modelling for Prestressed Concrete Elements.....	22
1.7 Hollow-core Slabs and Modes of Failure	24
1.7.1 Loss of Support.....	24
1.7.2 Flexure-Shear Failure in Positive Moment.....	25
1.7.3 Flexure and Flexure-Shear Failure in Negative Moment.....	27

1.7.4	Torsional Failure	28
1.8	Objectives	30
Chapter 2: Potential wall-diaphragm issues in rocking masonry wall buildings.....		32
2.1	Situation A: A Rocking wall with adjacent walls	33
2.2	Situation B: Hollow-core units with adjacent pairs of rocking walls	34
2.3	Situation C.1 & C.2: Hollow-core units supported by rocking walls of different lengths and rocking at the same angle	35
2.4	Situation D.1 and D.2: Hollow-core units supported by rocking walls rotating at different angles	38
2.5	Summary	42
Chapter 3: Model Development and Validation		45
3.1	Model overall description	45
3.2	FEM Development	47
3.2.1	Interactions and constraints	53
3.2.2	Element Type	56
3.2.3	Prestress and Boundary Conditions	58
3.2.4	Material properties.....	62
3.3	FEM Validation.....	72
3.3.1	Experimental test overview (Pachalla & Prakash, 2018)	72
3.3.2	Validated model	74
Chapter 4: Parametric Study		88
4.1	Overview	88
4.2	Hollow-core geometries and nomenclature	89
4.2.1	Hollow-core Geometries.....	90
4.3	Material properties.....	94
4.3.1	Concrete.....	94
4.3.2	Strands	98

4.3.3	Reinforcement steel	98
4.4	Results	100
4.4.1	Reference Specimen: 203-HC-(7-0 S) (2-meter span)	100
4.4.2	Effect of the span length	105
4.4.3	Effect of hollow-core depth	108
4.4.4	Effect of adding top prestressing	110
4.4.5	Outlier cases	113
4.4.6	Tables of results	115
Chapter 5:	Conclusion and Recommendations	118
5.1	Conclusions	118
5.2	Recommendations	120
References:	122

List of Figures

Figure 1.1.	Forces acting on an unbonded PT masonry wall (Schultz & Kalliontzis, 2017)	2
Figure 1.2.	Slotted wall-to-floor V connector (Watkins, 2017)	2
Figure 1.3.	Elevation view showing the prototype's FEM displacement shape (magnified 3 times) (Henry et al. 2012)	5
Figure 1.4.	Transversal view of an interior masonry wall with a bearing hollow-core slab and its detailing (Smith et al. 2020)	7
Figure 1.5.	Transversal view of an exterior masonry wall with a hollow-core slab and its detailing (Smith et al. 2020)	8
Figure 1.6	Simply Supported connection	8
Figure 1.7.	Front view of a bearing masonry wall with a cast-in-place slab (Ashour and El-Dakhkhni 2016)	9
Figure 1.8.	(a) The geometry of hysteretic energy dissipation devices and (b) detailing of the confining columns (Toranzo et al. 2009)	11
Figure 1.9.	General dimensions and the position that the shallow (G1) and deep (G2) grooves were placed. (C stands for no groove). (Toranzo et al. 2009)	12
Figure 1.10.	Reinforcement mesh of the slab with shallow grooves (1st and 3rd floor) and the deeper groover (2nd-floor slab) (Toranzo et al. 2009)	12
Figure 1.11.	Reinforcing detailing at the base of exterior columns (Toranzo et al. 2009)	13
Figure 1.12	Comparison of the damage between slabs without grooves, with shallow grooves and with deeper grooves. (Toranzo et al. 2009)	13

Figure 1.13. PreWEC wall System (Henry, 2011)	14
Figure 1.14. Slotted connection used on parallel precast slabs (isolated connection) (Henry, 2011).....	15
Figure 1.15. Principal strains contours on cast-in-place diaphragm-wall connection at 2% lateral drift (Left: Concrete; Right: Reinforcing steel) (Henry 2011)	16
Figure 1.16. Comparison of responses between the FEM with an isolated floor, cast-in-place floor and considering the wall without any floors (Henry 2011).....	16
Figure 1.17. Elevation view of specimen PFS1 (Liu 2016).....	18
Figure 1.18. Elevation view of specimen PFS2 (Liu 2016).....	18
Figure 1.19. Comparison of the hysteresis loop between the specimen PFS1 and the numerical model of the isolated PreWEC system at 2% drift (Liu 2016).....	19
Figure 1.20. Specimen PFS2 force-displacement response (isolated wall-floor connection) (Liu 2016)	19
Figure 1.21. Crack map and localized damage at the wall-floor connection after the test (Specimen PFS1) (Liu 2016)	20
Figure 1.22. Drift level markers beneath the hollow-core units show no damage on specimen PFS2 (Liu 2016).....	21
Figure 1.23. Specimen PFS2 cracks due to rebar discontinuity (Liu 2016).....	21
Figure 1.24. Torsion of a seating beam (Jensen, 2006)	24
Figure 1.25. Failure mechanisms with (a) and without (b) topping delamination (Jensen, 2006).....	25
Figure 1.26. Flexure-Shear failure mechanism (Jensen, 2006).....	26
Figure 1.27. Flexure-Shear Failure (Bull and Matthew, 2003).....	26
Figure 1.28. (a) Flexure failure mechanism and (b) Flexure failure mechanism (Khanal, 2019).....	27
Figure 1.29. Flexure-Shear failure mechanism (Jensen, 2006).....	28
Figure 1.30. Distribution and redistribution of stresses in a hollow-core unit with torsional effects (Jensen, 2006)	29
Figure 1.31. Hollow-core unit converted into I beams (Fenwick et al. 2010).....	29
Figure 2.1. Floor plan with potential situations in a masonry building with rocking walls.....	32
Figure 2.2. (a) Isometric view of a rocking wall with adjacent walls and hollow-core slabs. (b) Elevation view with the overlapping due to the rocking of the wall	33
Figure 2.3. (a) Isometric view of hollow-core units with adjacent walls of rocking walls “coupled”. (b) Elevation view shows the rocking of the walls and the incompatibility of displacements between the hollow-cores. (c) Zoom of the displacement incompatibility.	34

Fig 2.4. Situation C.1: (a) Isometric view of the two walls with different lengths. (b) Top edge elevation views of the two walls with different lengths rocking in direction 1 (on the same pivot point). (c) Top edge elevation views of the two walls with different lengths rocking in direction 2 (on a different pivot point). (d) Zoom of the displacement incompatibility in (c).....	36
Fig 2.5. Situation C.2: (a) Isometric view of the two walls with different lengths (not aligned). (b) Top edge elevation views of the two walls with different lengths rocking in direction 1. (c) Zoom of the displacement incompatibility in (b). (d) Top edge elevation views of the two walls with different lengths rocking in direction 2. (e) Zoom of the displacement incompatibility in (d).....	37
Figure 2.6. (a) Isometric view of the two rocking walls of the same length and aligned with each other. (b) Top edge elevation view of the two walls with the same length and rotating at different angles. $\theta_1 < \theta_2$	39
Figure 2.7. (a) Isometric view of the two rocking walls with different lengths and aligned with each other. (b) Top edge elevation view of the two walls with different lengths and rotating in direction 1 when the longer wall rotates at a bigger angle. (c) Top edge elevation view of the two walls with different lengths and rotating in direction 2 when the longer wall rotates at a bigger angle. (d) Zoom of the combination of vertical displacement and angular displacement incompatibilities in (c). $\theta_1 < \theta_2$	40
Figure 3.1. Fixed masonry wall – hollow-core connection.....	46
Figure 3.2. Simplified fixed/rigid connection for the FEM formulation.....	46
Figure 3.3. Rebar and prestressing steel in the hollow-core slab system.....	47
Figure 3.4. FEM formulation followed procedure in ABAQUS.....	48
Figure 3.5. Illustrations of a 203 mm hollow-core (with fixed connection) model assembly. (a) Isometric view. (b) Cross-section view.....	49
Figure 3.6. Illustration of the meshed 203 mm hollow-core model with fixed connection. (a) Isometric view. (b) Cross-section view. (c) Zoom of a meshed strand cross-section....	50
Figure 3.7. Surface to surface contact, ABAQUS (6.14).....	54
Figure 3.8. Comparison of stresses between default and calculated interface stiffness of a HC 203, with core diameters of 139 mm and 7 – 12.7 mm diameter strands with a prestress of 700 MPa.....	55
Figure 3.9. Assigned constraints to the model.....	56
Figure 3.10 Representation of the Hoyer effect (Briere et al. 2013).....	57
Figure 3.11. Boundary conditions at the prestress step.....	61
Figure 3.12. Boundary conditions at the displacement step.....	61
Figure 3.13. Applied displacement at a reference point.....	62
Figure 3.14 Family of hyperbolic flow potentials in the p-q plane, ABAQUS (6.14)	63
Figure 3.15 Yield surfaces in the deviatoric plane, corresponding to different values of K_c , (ABAQUS (6.14))	64

Figure 3.16 Concrete stress-strain relationship in compression, (ABAQUS (6.14))	66
Figure 3.17 Concrete stress-strain relationship in tension, (ABAQUS (6.14))	68
Figure 3.18. True stress-true strain relationship, (ABAQUS (6.14))	69
Figure 3.19. Strain-Stress curve (Chang et al. 1996)	71
Figure 3.20. Hollow-core slab cross-section (Pachalla and Prakash, 2018)	73
Figure 3.21. Test setup (Pachalla and Prakash, 2018)	73
Figure 3.22. Hollow-core slab cross-section (Validation Model)	74
Figure 3.23. a) Partition of the hollow-core slab. b) Meshing of the hollow-core slab. c) Zoom of the strand's meshing	75
Figure 3.24. Boundary conditions and loading in validated model	76
Figure 3.25. Compressive stress-strain relationship $f'_c=34$ MPa (Chang and Mander 1994)	77
Figure 3.26. Tensile stress-strain relationship $f_t=2.38$ MPa (Chang and Mander 1994)	78
Figure 3.27. Strand stress-strain relationship for a Grade 1860, 7-wire low relaxation strand.	78
Figure 3.28. Cylinder with boundary and loading conditions	82
Figure 3.29. Comparison between Chang and Mander (1994) constitutive model vs ABAQUS explicit cylinder test, $f'_c=34$	83
Figure 3.30. Camber displacement (mm) due to prestress (Pachalla and Prakash, 2018)	84
Figure 3.31 Camber displacement (mm) due to prestress (Validation Model)	85
Figure 3.32. Load-displacement relationship comparison	85
Figure 3.33. Longitudinal stresses at the bottom of the slab (Theoretical values vs Validation model)	86
Figure 3.34 Load-Displacement response (Viscosity parameter comparison)	87
Figure 4.1 Hollow-core cross-sections. All Geometries were obtained from Coreslabs (2009)	90
Figure 4.2. Compressive stress-strain relationship $f'_c=40$ MPa (Chang and Mander 1994)	95
Figure 4.3. Tensile stress-strain relationship $f_t=4$ MPa (Chang and Mander 1994)	95
Figure 4.4. 400W - Reinforcement steel stress-strain relationship	98
Figure 4.5. 203-HC-(7-0 S)-2 at the beginning of the incompatibility of the displacement step. The yielding areas are shown in gray colour	102
Figure 4.6. 203-HC-(7-0 S)-2 (at the non-displaced end, representing relative upward motion) at 10% damage. The yielding areas are shown in gray colour	102
Figure 4.7. 203-HC-(7-0 S)-2 (at the non-displaced end, representing relative upward motion) at 20% damage. The yielding areas are shown in gray colour	103
Figure 4.8. 203-HC-(7-0 S)-2 (Fixed end) at 30% damage. The yielding areas are shown in gray colour	103

Figure 4.9. 203-HC-(7-0 S)-2 (at the non-displaced end, representing relative upward motion) at the failure stage. The yielding areas are shown in gray colour.....	104
Figure 4.10. 203-HC-(7-0 S)-2 (displacement end, representing a relative downward motion) at the 30% damage stage. The yielding areas are shown in gray colour.....	104
Figure 4.11. 203-HC-(7-0 S)-2 (prestress being applied at the hollow-core and topping) showing a continuous strain behaviour between the topping and the slab with a) “non-continuous” and b) “continuous” meshing configurations between them.....	105
Figure 4.12. 203-HC-(7-0 S)-2 at 30% damage stage. The yielding areas (cracks) are shown in gray colour.	106
Figure 4.13. 203-HC-(7-0 S)-5 at 30% damage stage. The yielding areas are shown in gray colour.	107
Figure 4.14. 203-HC-(7-0 S)-8 at 30% damage stage. The yielding areas are shown in gray colour.	107
Figure 4.15. Displacement capacity by span length (203 HC (7-0 S)) at 30% damage and failure stage.....	108
Figure 4.16. Displacement-damage relationship (HC with prestressing only at the bottom)-2-meter span.....	109
Figure 4.17. Displacement-damage relationship (HC with prestressing only at the bottom)-5-meter span.....	109
Figure 4.18. Displacement-damage relationship (HC with prestressing only at the bottom)-8-meter span. *.....	110
Figure 4.19. 203 HC (7-5 S)-2 at failure stage	111
Figure 4.20. Displacement-damage relationship comparison between HCs with prestressing only at the bottom and HCs with prestressing at the top and bottom)-2-meter span.	112
Figure 4.21. Displacement-damage relationship comparison between HCs with prestressing only at the bottom and HCs with prestressing at the top and bottom)-5-meter span.	112
Figure 4.22. Displacement-damage relationship comparison between HCs with prestressing only at the bottom and HCs with prestressing at the top and bottom)-8-meter span.	113
Figure 4.23. Yielding on the cross-sectional face at the failure stage (254-HC-(10-0 S)-8).....	114
Figure 4.24. Yielding on the cross-sectional face and a downwards diagonal crack developing at 30% damage stage (355-HC-(13-0 S)-8)	114
Figure 4.25. Example dimensions: a) Isometric and elevation view before rocking; b) Elevation view when rocking	116

List of Tables

Table 2.1 Summary of situations discussed above.	42
Table 3.1 Summary of the concrete-strand interaction properties	55
Table 3.2 Constraints summary.....	55
Table 3.3 Estimate of lump sum losses (MPa) (CSA Group (4), 2019).....	59
Table 3.4 Summary of the boundary conditions for the prestress step.	59
Table 3.5 Summary of the boundary conditions for the displacement incompatibility step.....	60
Table 3.6. Cross-sectional details comparison	75
Table 3.7 Material Properties and ABAQUS input for the Hollow-core slab (Concrete).....	79
Table 3.8 Stress-strain relationship data for concrete $f'_c=34$ MPa and $f_t=2.38$ MPa.....	80
Table 3.9 Material properties and ABAQUS input for the prestressing strands.	81
Table 4.1. List of Models in Parametric Study.....	93
Table. 4.2 Stress-strain relationship data for concrete $f'_c=40$ MPa and $f_t=4$ MPa	96
Table 4.3. Material Properties and ABAQUS input for the Hollow-core slab and the topping (Concrete).....	97
Table 4.4 Material properties and ABAQUS input for the prestressing strands	99
Table 4.5. Displacement capacities with 2 m span.....	117
Table 4.6. Displacement capacities with 5 m span.....	117
Table 4.7. Displacement capacities with 8 m span.....	117

Declaration of Academic Achievement

All ABAQUS models and Excel Spreadsheets that were used, shown and discussed herein were developed by Oscar Camarillo Garduño. Each draft of this thesis was produced by Oscar Camarillo Garduño. Advice, revisions, suggestions, and guidance were provided by the academic supervisors Dr. Lydell Wiebe and Dr. Mohamed Ezzeldin. All the presented information from external sources (including figures and tables) in this thesis has been cited and referenced accordingly. All other materials are the product of the work of Oscar Camarillo Garduño.

Chapter 1: Introduction and Literature Review

1.1 Introduction

Conventional fixed-base shear walls are typically designed to dissipate energy in the form of plastic deformations in response to lateral loads. This design philosophy causes permanent damage to the structural system and residual drifts that can lead to costly repairs, delays due to rehabilitation of the building after an earthquake, or demolition of the structural system. Conversely, controlled rocking walls are a self-centering seismic force-resisting system that has been developed as a structural solution to minimize residual drifts and damage after an earthquake (Priestley et al. 1999). In this system, the wall starts to uplift (rock) once the lateral forces exceed its decompression capacity, which prevents yielding and plastic deformations. The self-weight and the unbonded post-tensioned strands which anchor the wall to the foundation are responsible for resisting the wall overturning, as shown in Figure 1.1. These rocking wall systems have often been isolated from tributary gravity loads of the floor diaphragms. This isolation can be achieved by using a wall-diaphragm connection that only transfers lateral loads and allows vertical and rotational displacements, such as the V-connector, shown in Figure 1.2 (Watkins, 2017).

The development of such systems has focused mostly on post-tensioned controlled rocking masonry and concrete walls (Laursen and Ingham 2001, 2004a, & 2004b; Yassin et al. 2020) that showed low damage and low residual drifts. However, according to Yassin et al. (2022a and 2022b), the implementation of unbonded post-tensioning is mostly limited to precast concrete shear walls since it is still challenging to fully implement it with masonry walls due to some concerns related to the high compression demands on the masonry wall toes. Also, the self-centering capability can be compromised due to post-tensioning losses, post-tension yielding, and

masonry degradation (Hassanli et al. 2016). These abovementioned concerns motivated the development of a new system by Yassin et al. (2022a and 2022b), namely Energy Dissipation-Controlled Rocking Masonry Walls (ED-CRMWs). The self-centering capability of this wall system relies only on vertical gravity loads, thus avoiding the implementation of post-tensioned tendons. ED-CRMWs system uses also energy dissipation devices, such as axial bars (Lee Kim et al. 2019) and replaceable flexural arms (Li et al. 2019), in order to both increase the ultimate strength and control the lateral displacements of the wall.

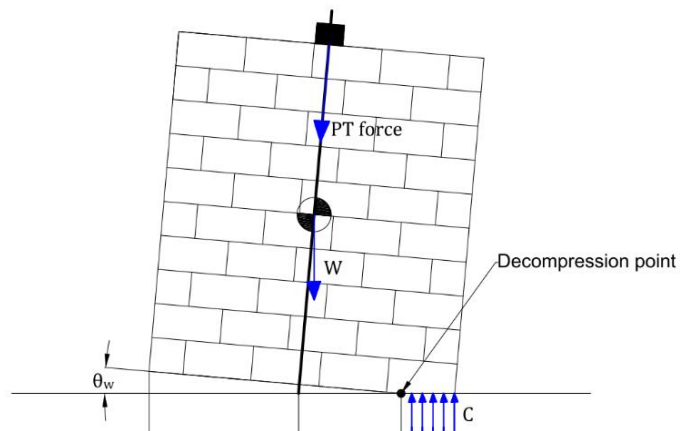


Figure 1.1. Forces acting on an unbonded post-tensioned masonry wall (Schultz & Kalliontzis, 2017)

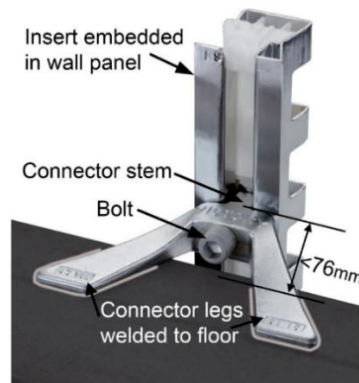


Figure 1.2. Slotted wall-to-floor V connector (Watkins, 2017)

Despite such advantages of control rocking systems, limited research has been conducted on the interaction between the controlled rocking wall and the diaphragm. For example, Henry (2011) and Liu (2016) investigated this interaction by considering a rocking concrete wall with: i) a cast-in-place concrete slab, and ii) an isolated precast concrete slab. The interaction between the rocking concrete wall and the cast-in-place concrete slab resulted in damage to the slab due to the vertical incompatibility of their displacements caused by the different boundary conditions between the wall and the surrounding elements. Conversely, the isolated precast concrete slab avoided displacement incompatibilities by implementing a connection that allowed such movements without damaging the slab. Even though the isolated slab prevents damage and delivers a resilient system, the implementation of the latter connection can be challenging due to the lack of guidance in the North American codes and design standards, as well as unfamiliarity in the masonry construction practice. Also, the isolated connection can not transfer vertical gravity loads to walls, which are needed for systems such as ED-CRMWs.

1.2 Hollow-core Slab

A hollow-core slab is a precast concrete member with extended voids throughout the element in order to reduce the weight and cost of the slab. This precast element is usually prestressed with uncoated-steel 7-wire low relaxation strands. Hollow-core slabs are mostly used as floor and roof systems for masonry structures (e.g., office, residential and parking buildings). A hollow-core slab provides the efficiency of a prestressed element with a high load capacity and a wide span range. This slab type has also high fire/thermal resistance and sound isolation.

1.3 Diaphragm-Wall Interaction

Previous research on concrete and rocking masonry walls, whose main objective was to have a low-damage resilient building, have facilitated the development of several elements, such as individual post-tensioned concrete walls (Henry et al. 2012), hybrid concrete walls (Marriott et al. 2008), precast concrete walls with end columns (PreWEC) (Sritharan et al. 2008), and post-tensioned controlled rocking masonry walls (Shultz et al. 2017, Yassin et al. 2020). These elements have mostly been studied, analyzed, and tested as isolated structural walls without considering the seismic response of the wall-to-floor interaction.

In a rocking wall system, the interaction between the diaphragm and the wall with a non-isolated connection must be analyzed when the self-centering response of the system is being examined under seismic events. Specifically, evaluating the wall-floor interaction and the corresponding contribution of this interaction to the overall performance of the rocking system is key. During a seismic event, lateral forces are transferred from diaphragms to shear walls, and if these walls are loadbearing walls, gravity loads are also transferred. Therefore, wall-to-floor connections must be designed to guarantee that lateral and gravitational load paths are preserved.

The main mechanism of a rocking system is a horizontal crack at the wall-foundation interface when the wall uplifts. This uplift leads to a vertical displacement incompatibility between the slab and the wall. For non-isolated diaphragms, this incompatibility can have an impact on the seismic behaviour of the whole building. This can then lead to damage to the diaphragm and can also cause a partial loss of the self-centering ability of the system due to residual displacements (Liu 2016), which may not be acceptable in the context of resilient buildings. This inevitable interaction with the surrounding structure creates a challenge in the diaphragm-wall connection design. Therefore, to achieve a low-damage building design, vertical

displacement incompatibilities should be carefully considered during the seismic design stage of controlled rocking systems when the wall-diaphragm connection is non-isolated.

The few research projects that have focused on this interaction (Priestley et al. 1999, Schoettler et al. 2009, Henry et al. 2012 and Watkins, 2017) have used special connectors to isolate the wall from the diaphragm in the vertical direction, thus avoiding vertical displacement incompatibilities while maintaining the lateral load transfer capability. The difference between isolated and non-isolated diaphragm-wall connections can be seen in Figure 1.3. As seen in this figure, with a non-isolated connection, the diaphragm uplifts and rotates with the wall. Also, the diaphragms are constrained to the gravity frames at the edges, resulting in out-of-plane bending of the diaphragm. Conversely, the isolated diaphragm (e.g., using a V-connector) does not uplift and rotate with the wall. As a result, isolated diaphragms do not have out-of-plane bending.

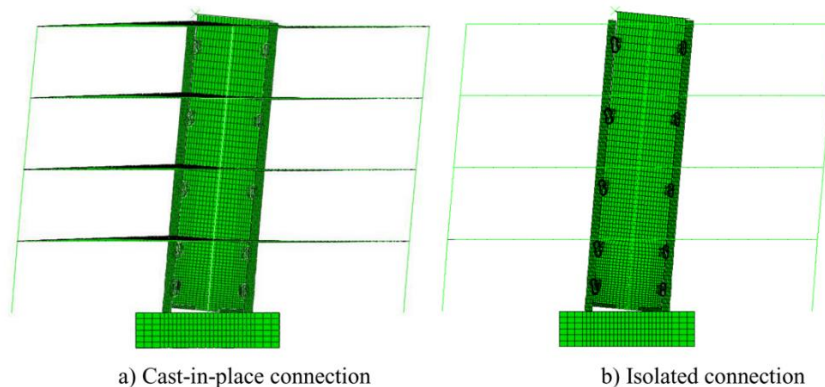


Figure 1.3. Elevation view showing the prototype's FEM displacement shape (magnified 3 times) (Henry et al. 2012).

1.4 Masonry Diaphragm-wall Connections

The connection types determine the wall-floor interaction behaviour in terms of how the lateral forces are transmitted from the slab to the wall and how the system responds to the incompatibility displacements. The connection must be designed to avoid premature failure. In masonry walls, the most commonly used connections for load-bearing walls with precast slabs or with cast-in-place slabs are discussed in this subsection

1.4.1 Precast Hollow-core Slab to Wall

Precast hollow-core slabs are the most common floor system used in new masonry structures in Canada (Smith et al. 2020). A fixed connection with a masonry wall is typically constructed with a precast plank seating on the masonry wall that includes an in-situ concrete topping binding the diaphragm to the wall. For interior walls, where the slab is placed on both sides of the wall, continuous longitudinal rebars with a grouting joint tie both slabs (Figure 1.4). For an exterior wall, where the slab is placed on one side of the wall, a rebar with a 90-degree angle connects the precast floor to the wall (Figure 1.5) to transfer lateral loads from the diaphragm to the wall. For both wall types, vertical continuity is achieved with continuity of the grout, the vertical reinforcement, and the dowel, as shown in Figures 1.4 and 1.5. The topping between the wall and the slab resists vertical displacements and rotations. This could result in vertical incompatibilities and/or torsional effects on the hollow-core slab and subsequently affects the overall behaviour of the rocking system (refer to section 1.8 for more information about the torsional behaviour of the hollow cores).

Another type of connection can be a simply supported connection, where the hollow-core slab is supported by an inverted T-beam and the collector as well as the boundary reinforcement

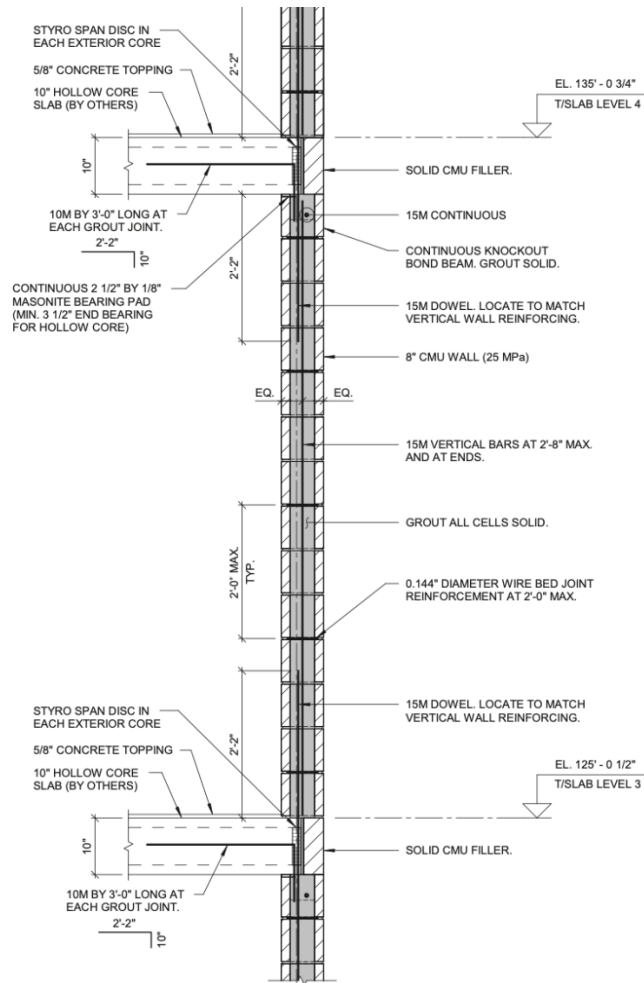


Figure 1.5. Transversal view of an exterior masonry wall with a hollow-core slab and its detailing (Smith et al. 2020).

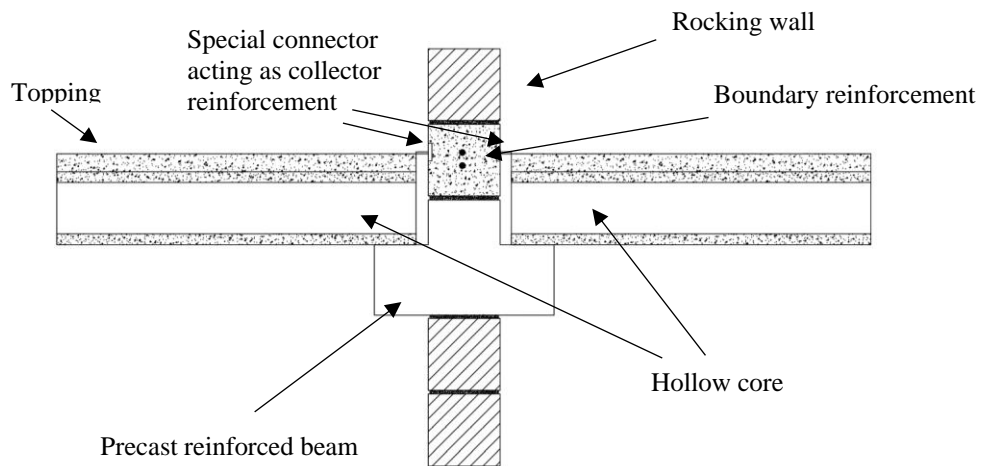


Figure 1.6 Simply Supported connection

1.4.2 Cast-in-place Slab to Wall Connection

A cast-in-place slab to wall connection is assembled with the slab having negative reinforcement bars, as shown in Figure 1.7. Also, the masonry wall has dowels that extend from the lower to the upper part of the masonry wall so that the wall and the diaphragm are bonded. These dowels are designed to allow the lateral load transfer from the diaphragm to the shear wall. Although cast-in-place to wall connections in masonry structures are not common in Canada (Banting, personal communication 2020), such connections are still mentioned here for applications elsewhere. Previous research projects that have investigated the interaction between a cast-in-place slab and rocking walls are discussed in section 1.6.

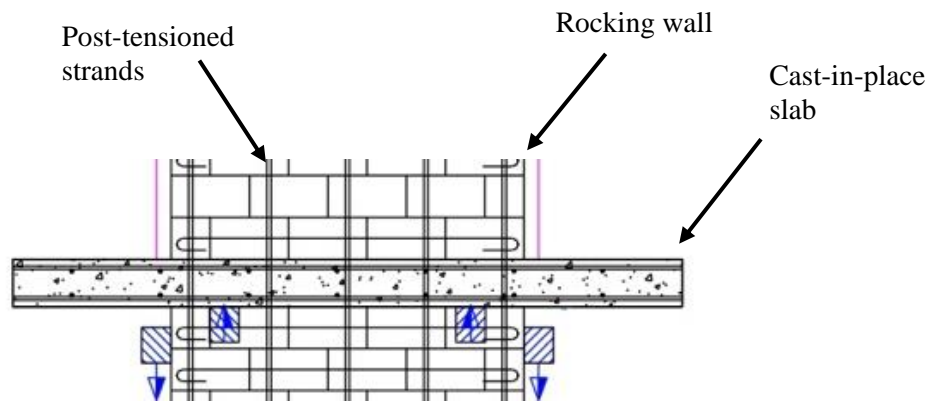


Figure 1.7. Front view of a bearing masonry wall with a cast-in-place slab (Ashour and El-Dakhakhni 2016)

1.5 Previous Studies of Rocking Wall Systems With a Focus on the Diaphragm-wall

Interaction

This subsection presents a summary of one research paper and two theses that focused on the rocking wall-floor interaction. Although some of these investigations have considered a concrete rocking wall, the results and findings are also relevant to masonry construction practice.

1.5.1 Shake-table Tests of Confined-rocking Masonry Walls With Supplementary Hysteretic Damping (Toranzo et al. 2009)

This research presents the results of a shake-table test on a 40% scale rocking masonry wall model prototype. The structural system consisted of unreinforced masonry walls with supplementary damping devices that were confined by small/light columns (Toranzo et al. 2009) and cast-in-place slabs. The supplementary damping device used was a foundation-fixed cantilever arm that was connected to the lower corners of the confining columns, as shown in Figure 1.8. In this research, a performance-based design methodology was followed. The methodology aimed at preventing structural damage, considering the rocking wall mechanism, controlling the magnitude of lateral drifts, and preventing residual displacements. The system was designed to remain elastic except for the energy-dissipation devices, the base of the exterior columns (grooves), and specific locations in each of the connecting slabs (grooves). The direct displacement-based design methodology proposed by Priestley (2000) was used and adapted for this research.

High rotational capacity-reduced moment zones were detailed at the slabs and the column bases (detailed for the column to behave as a pin), as shown in Figures 1.9, 1.10, and 1.11. These zones on the slab were formed by grooves in the hinge zones. Shallow (10x20 mm) and deep grooves (20x10 mm) were built adjacent to the wall and columns. At a drift ratio of 2.5%, the

damage was observed mostly in zones where shallow grooves were built or in zones that had no grooves (Figure 1.12).

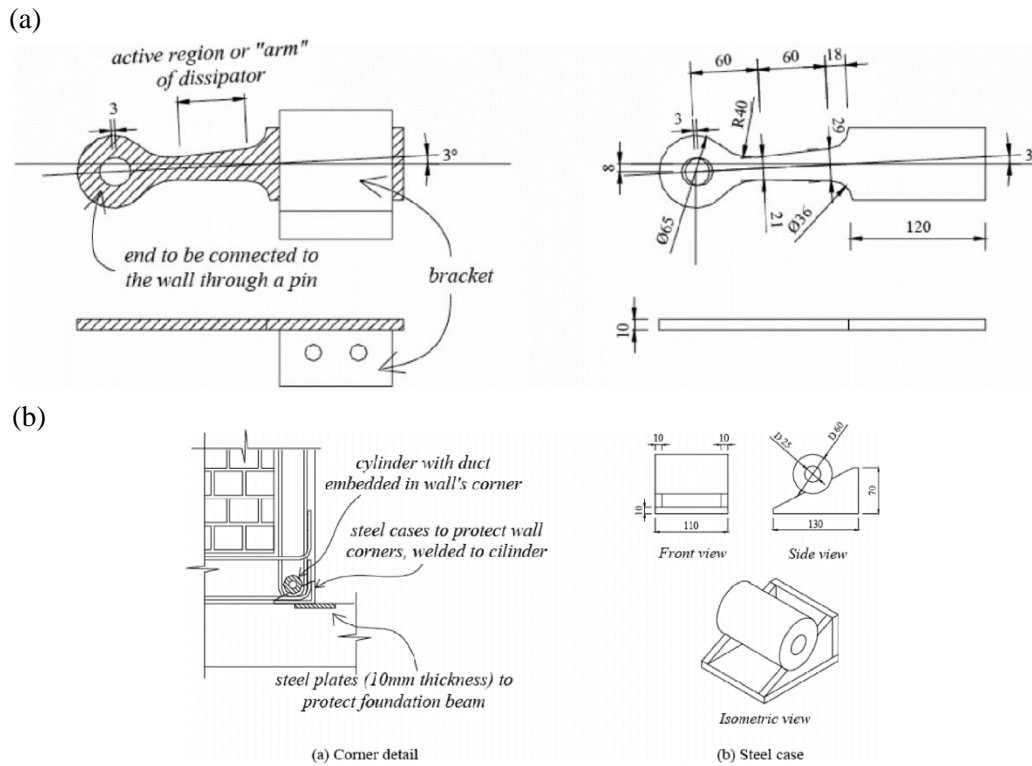


Figure 1.8. (a) The geometry of hysteretic energy dissipation devices and (b) detailing of the confining columns (Toranzo et al. 2009).

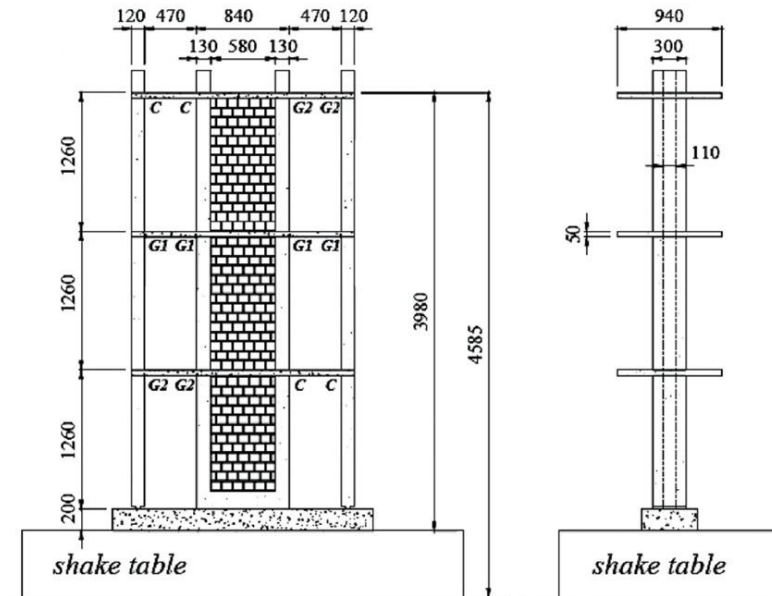


Figure 1.9. General dimensions and the position that the shallow (G1) and deep (G2) grooves were placed. (C stands for no grooves). (Toranzo et al. 2009)

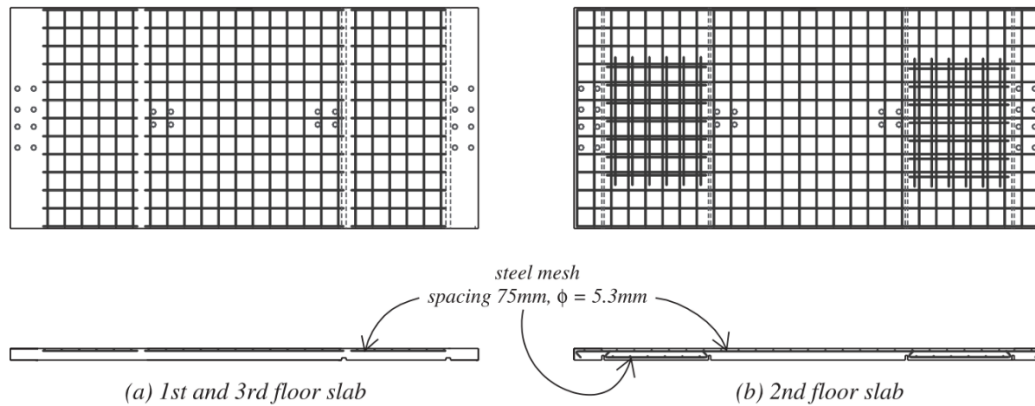


Figure 1.10. Reinforcement mesh of the slab with shallow grooves (1st and 3rd floor) and the deeper groover (2nd-floor slab) (Toranzo et al. 2009).

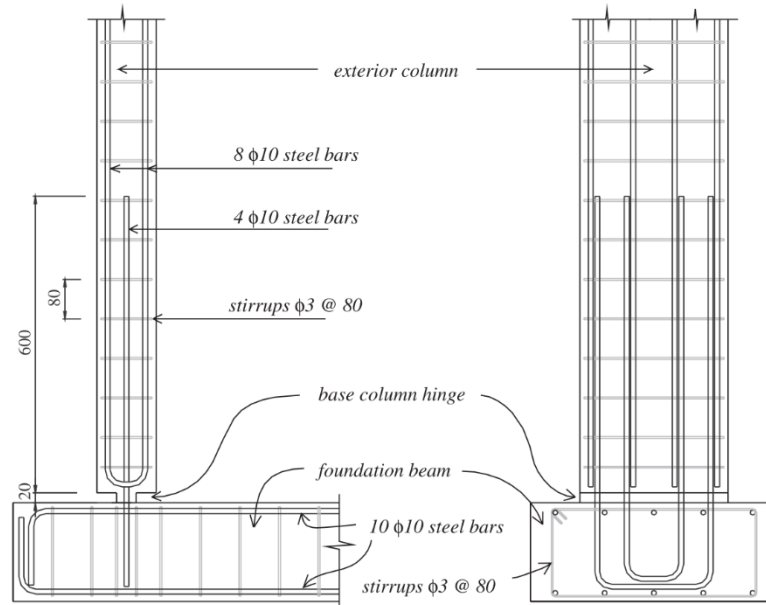


Figure 1.11. Reinforcing detailing at the base of exterior columns (Toranzo et al. 2009).

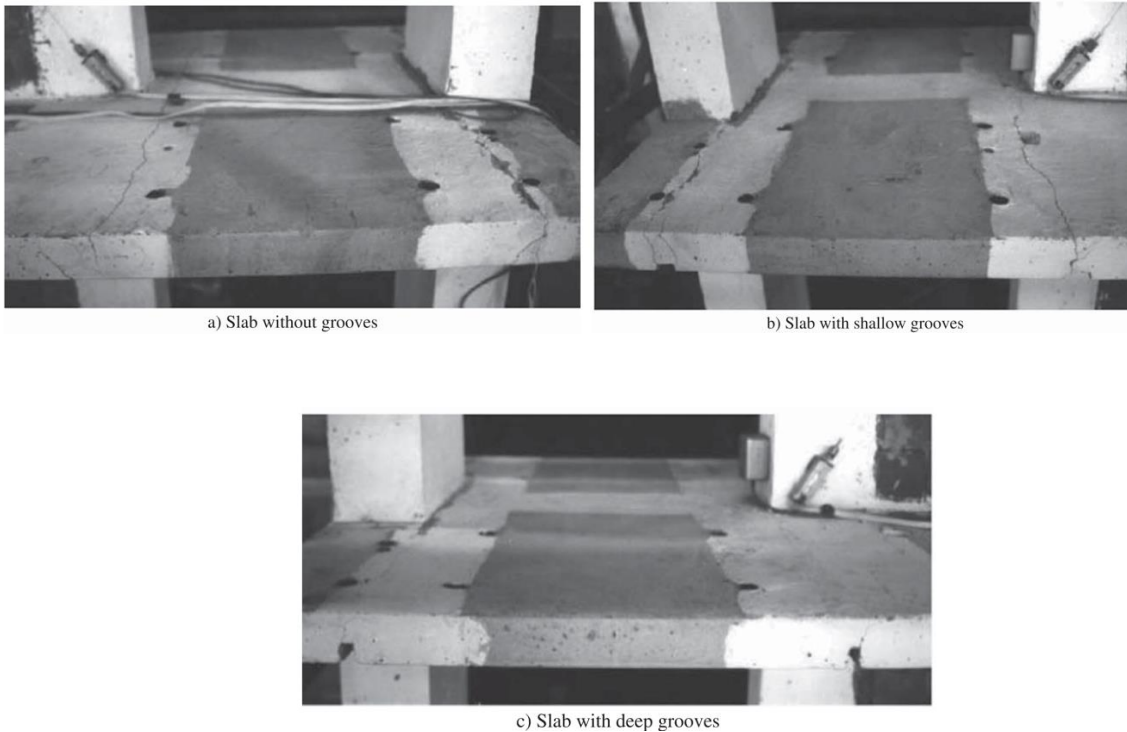


Figure 1.12. Comparison of the damage between slabs without grooves, with shallow grooves and with deeper grooves. (Toranzo et al. 2009)

1.5.2 Self-centering Precast Concrete Walls for Buildings in Regions with Low to High Seismicity (Henry 2011)

One of the objectives of this research was to overcome the uncertainty in the behaviour of a whole building including the interaction between the self-centering wall and surrounding elements. This research used Precast Wall with End Columns (PreWEC) wall system which achieved its self-centering mechanism with post-tensioned strands and used an energy dissipation device (O-connector), as shown in Figure 1.13. In the analysis of the self-centering system, different wall-diaphragm connections were presented.

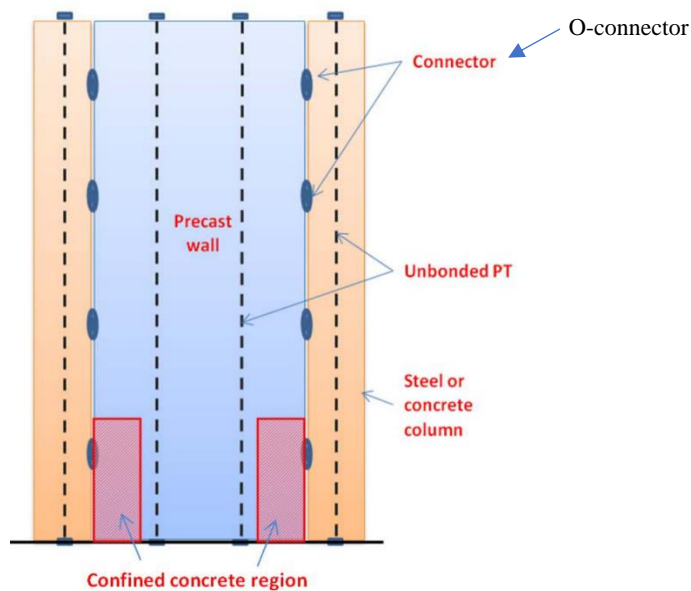


Figure 1.13. PreWEC wall System (Henry, 2011)

The typical types of connections that were identified in this research included the rigid cast-in-place wall-to-floor connection, semi-rigid precast floor units bearing on the wall connection, and an isolated connection with precast units placed in parallel to the wall which was achieved by using a slotted connection (Figure 1.14). Although these three different connections were identified, this research focused only on rigid and isolated connections.

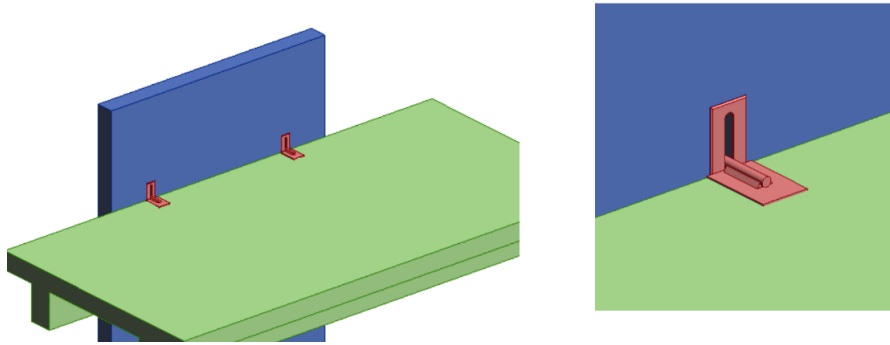


Figure 1.14. Slotted connection used on parallel precast slabs (isolated connection) (Henry, 2011)

Finite element analysis was used to investigate the effects of the presented connections. The model in ABAQUS software found that when a rigid connection was used, the deformations of the floors were significant (about 30% of the floor cracks at 3% drift). Due to these deformations, the concrete floor showed cracks and the rebar steel yielded, resulting in significant damage to the floor (Figure 1.15). Also, the lateral strength increased approximately by 44% and 50% at drifts ratios of 2% and 3%, respectively. The increase in the lateral strength can affect the seismic design of the building since it was not originally designed for these higher strength values.

The isolated connection prevented the damage to the floor and the lateral strength was more predictable (Figure 1.16). The behaviour of the rocking wall was primarily similar to an individual Precast Wall with End Columns (PreWEC) specimen, with concentrated deformations at the wall base with a single crack. No significant damage was also found on the floor, where strains did not exceed the concrete cracking strain.

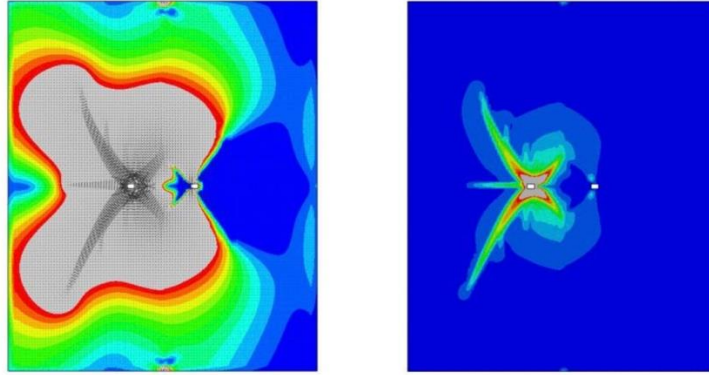


Figure 1.15. Principal strains contours on cast-in-place diaphragm-wall connection at 2% lateral drift (Left: Concrete; Right: Reinforcing steel) (Henry 2011).

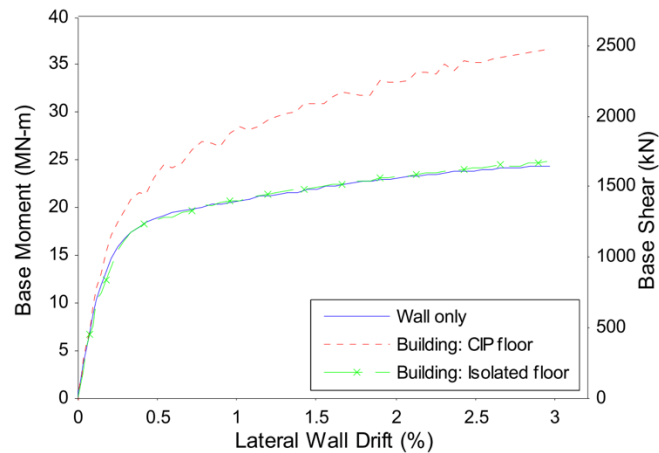


Figure 1.16. Comparison of responses between the FEM with an isolated floor, cast-in-place floor and considering the wall without any floors (Henry 2011).

1.5.3 Interaction between Rocking Wall System and Surrounding Structure (Liu 2016)

In this research, a one-third-scale prototype building was built. The building consisted of PreWEC rocking walls in one direction and special moment frames in the orthogonal direction. In this study, two specimens were considered. The first specimen (PFS1) was a PreWEC with side columns made of short steel tubes, two O-connectors (dissipation device) connected to each of four side columns, and a cast-in-place unbonded post-tensioned slab as a floor system and rigid

floor-edge beam connections, as shown in Figure 1.17. The second specimen (PFS2) was a PreWEC with end columns made of RC columns, four O-connectors connected to each of two end columns, a precast slab formed by solid RC units as a floor system and pinned-pinned floor edge beam connections, as shown in Figure 1.18. Specimen PFS1 had a significant interaction due to the cast-in-place unbonded post-tensioned slab connection that transferred gravity and lateral loads to the wall. In contrast to PFS1, specimen PFS2 had a negligible wall-diaphragm interaction due to the vertical movement of the isolated connectors. PFS2 used hollow-core slabs which were supported by precast girders and edge beams. Figure 1.19 shows the hysteresis loops of PFS1 and the PreWEC system with an isolated diaphragm. With quasi-static loading, the dissipation capacity can be represented by the area inside the hysteresis loops. The energy dissipation of PFS1 was more than three times higher than a PreWEC with an isolation system. Also, PFS1 had a peak of 0.87% residual drift which compromised the self-centering ability of the system, while PFS2 had a peak of 0.088% residual drift (Figure 1.20) which is considered negligible. The higher dissipation capacity and the larger residual drift in comparison to the PreWEC system with the isolated diaphragm can be attributed to the surrounding structure and the corresponding damage (Figure 1.21). The local damage to the cast-in-place slab was concentrated on the floor slab adjacent to the wall (Figure 1.21). Minor cracks also formed at the floor-edge beam interface. After the damage was fully developed, the slab behaved as an independent body without damage. The advantages of a rigid-floor connection are the contribution of the gravity loads to the strength of the PreWEC system and the self-centering capacity. The disadvantages are the damage around the rocking walls (Figure 1.21) and the repair that is needed after seismic events.

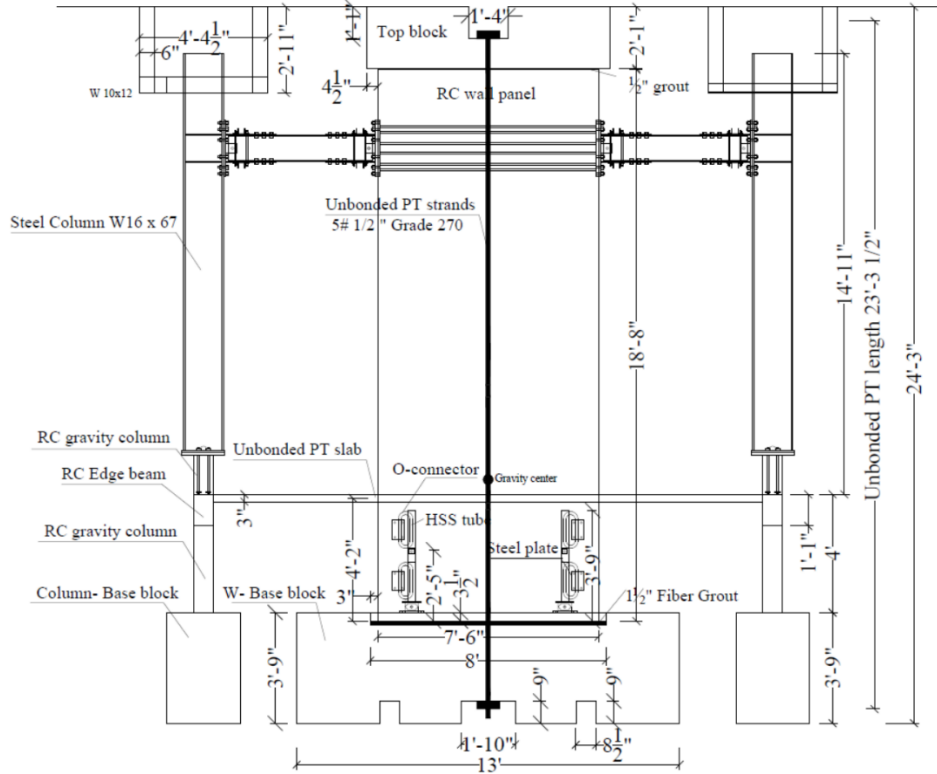


Figure 1.17. Elevation view of specimen PFS1 (Liu 2016)

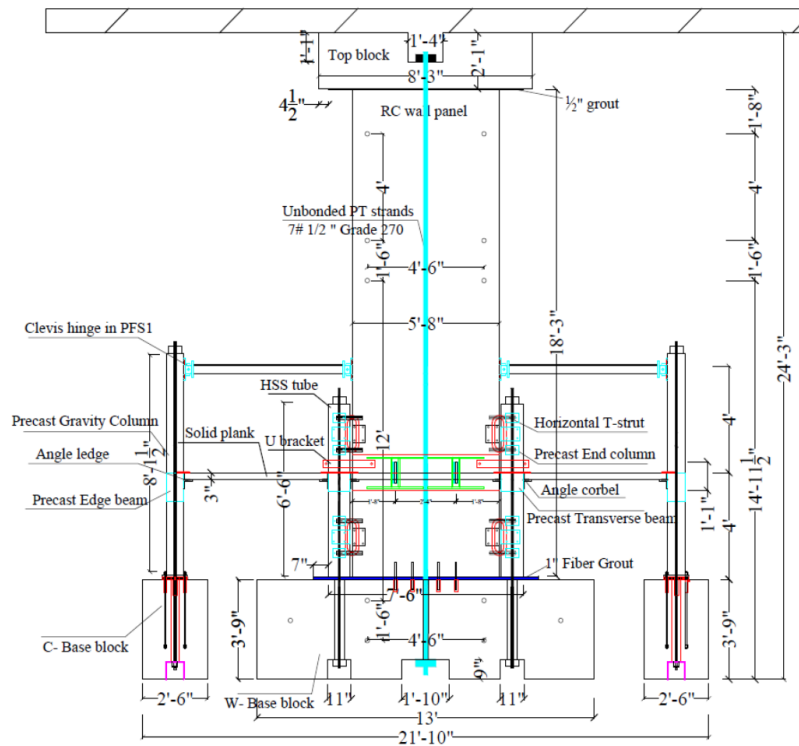


Figure 1.18. Elevation view of specimen PFS2 (Liu 2016).

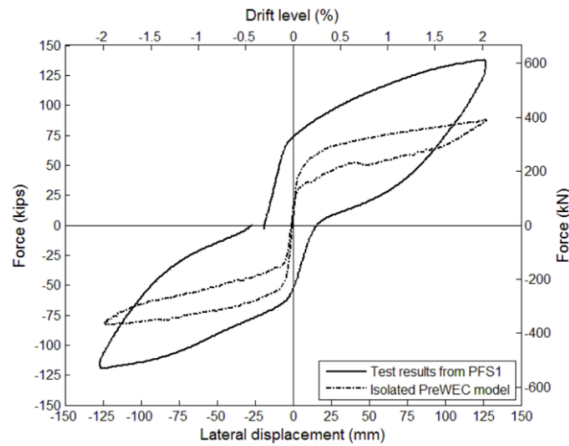


Figure 1.19. Comparison of the hysteresis loop between the specimen PFS1 and the numerical model of the isolated PreWEC system at 2% drift (Liu 2016)

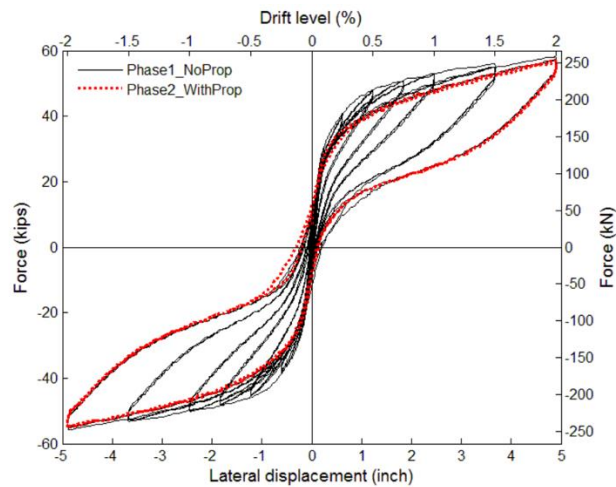


Figure 1.20. Specimen PFS2 force-displacement response (isolated wall-floor connection) (Liu 2016).

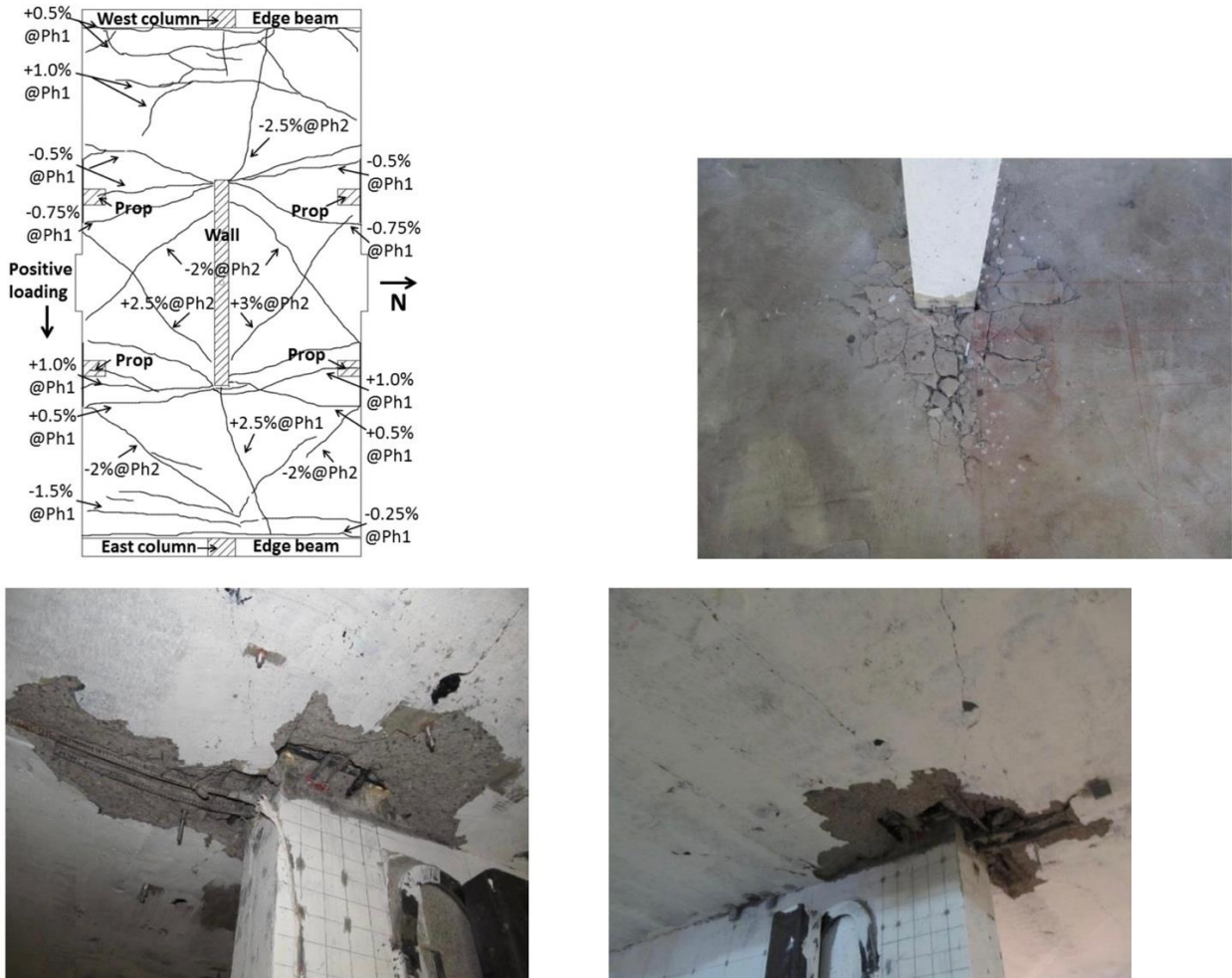


Figure 1.21. Crack map and localized damage at the wall-floor connection after the test (Specimen PFS1) (Liu 2016)

Due to the negligible residual drift of specimen PFS2, the whole specimen was almost without damage due to the uplift of the wall (Figure 1.22). However, cracks were observed due to rebar discontinuity (Figure 1.23). The advantages of rocking wall structures with an isolating connection include almost damage-free structures after seismic events and the whole system performance can be more predictable. The disadvantages include the need for additional gravity load paths in structures that may limit the architectural floor-plan layouts. Also, due to the lack of

contribution from gravity loads to the strength of the isolated PreWEC system, the initial post-tensioning force may be required to be larger.

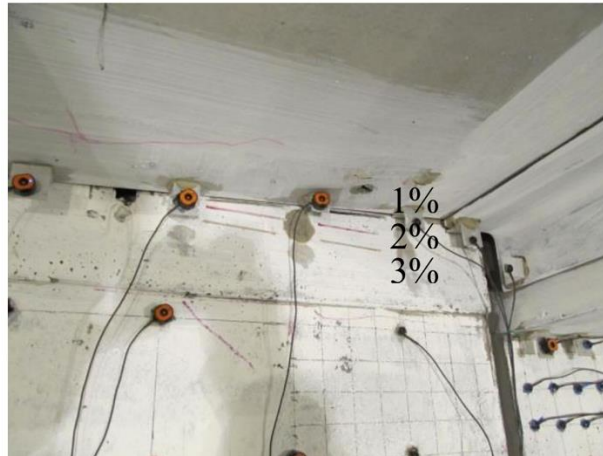


Figure 1.22. Drift level markers beneath the hollow-core units show no damage on specimen PFS2 (Liu 2016).



Figure 1.23. Specimen PFS2 cracks due to rebar discontinuity (Liu 2016).

1.6 Finite Element Modelling for Prestressed Concrete Elements

This section presents a summary of research papers that focused on finite element modelling techniques for prestressed concrete elements. Some of these techniques were used in modelling the prestressed hollow-core slabs in this thesis. Further and more detailed information is described in Chapter 3.

Arab et al. (2011) presented a methodological approach for finite element analysis of pre-tensioned concrete members. This study used two approaches to model pre-tensioned strands and their interactions with concrete. The first approach is the extrusion technique which uses 3-D strands and a friction-based contact interaction. The approach uses a concrete-strand interaction to capture the normal/tangential behaviour that prevents any penetration and captures the specified friction between the surfaces. This interface interaction is based on the strain-compatibility technique; however, it fails to capture any slippage between the strands and the concrete (Yapar et al. 2015). The second approach uses the embedment technique that does not require any modelling of contact surfaces, and thus reduces the number of iterations and the computational costs of the simulations. The embedded element is confined inside the host element and its degrees of freedom are suppressed as they follow those of the host element (Arab et al. 2011). Although the embedment technique is less expensive than the extrusion technique, it requires modelling the pre-tensioned strands as 1-D truss elements, which is not capable of capturing one of the main transfer mechanisms between the strands and the surrounded concrete, namely the Hoyer effect. This effect captures the strand's tendency to return to its original shape/diameter after releasing the strands (Yapar et al. 2015). Lack of accuracy occurs due to the above-mentioned strain-compatibility assumption and the usage of the embedment technique.

Yapar et al. (2015) presented a prestressed concrete beam nonlinear finite element model. This study aimed at addressing several assumptions that previous studies have made. A prestressed beam with stirrups was modelled with the Concrete Damaged Plasticity (CDP) model in the commercial software ABAQUS. Instead of using 1-D truss elements for modelling the pre-tensioned strands, the study used 3-D elements in order to capture the Hoyer effect in the strands-concrete interaction. Also, the study avoided the assumption of strain compatibility at the steel and concrete interfaces due to the lack of slippage and bond failure. Instead, the study used a bond-slip behaviour using interfacial distributed spring elements with zero dimensions. This was achieved by using a contact interaction and adding the normal behaviour (prevented penetration between surfaces), tangential behaviour (captured the friction in the interaction), cohesive behaviour (considered the slippage between the strands and the concrete) and damage behaviour (captured the degradation of the cohesive stiffness). Using such interface interactions and 3-D elements for modelling the strands showed accurate results when such techniques were validated with experimental tests (full details in Yapar et al. 2015).

Broo et al. (2015) presented a finite element analysis of a full-scale test of shear and a full-scale test of torsion in prestressed hollow-core units. The finite element model in this study was developed using the non-linear finite element program DIANA 8.1. The modelling technique focused on developing the hollow-core unit with solid elements only in the critical areas. The rest of the unit was built with beam elements. The strands were modelled with 2-node bar elements including interface elements with a predefined bond-slip interaction in order to simulate the bond between the strands and the concrete. The solid elements were connected to the beams assuming a stiff rotation and that the plane cross-section remained plane. This investigation showed that combining coarse solid elements for critical unit sections and beam elements for the rest of the

slab was a reasonable modelling technique. This allowed for less time-consuming analyses without jeopardizing the accuracy.

1.7 Modes of Failures of Hollow-core Slabs

Inspections after earthquakes and extensive research in New Zealand have illuminated the potential failure modes that hollow-core slabs can face. Also, retrofits are recommended to be performed to increase life safety in case one of the critical failure modes occurs.

1.7.1 Loss of Support

Loss of support or loss of seating is directly associated with critical connection deficiencies. Such deficiencies are the insufficient seating length and/or seating ledges (supporting beam) with an unreinforced cover seat. This loss of support occurs due to the potential rotation of the seating beam which supports the hollow-core slabs, as shown in Figure 1.24. Figure 1.25 shows also the types of failure, including the combination of trapped portions of the hollow-core slab and the fracture of the seating ledge.

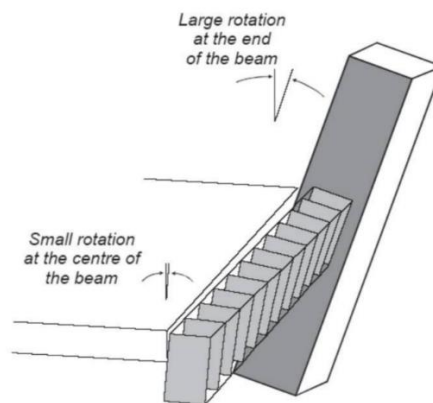


Figure 1.24. Torsion of a seating beam (Jensen, 2006).

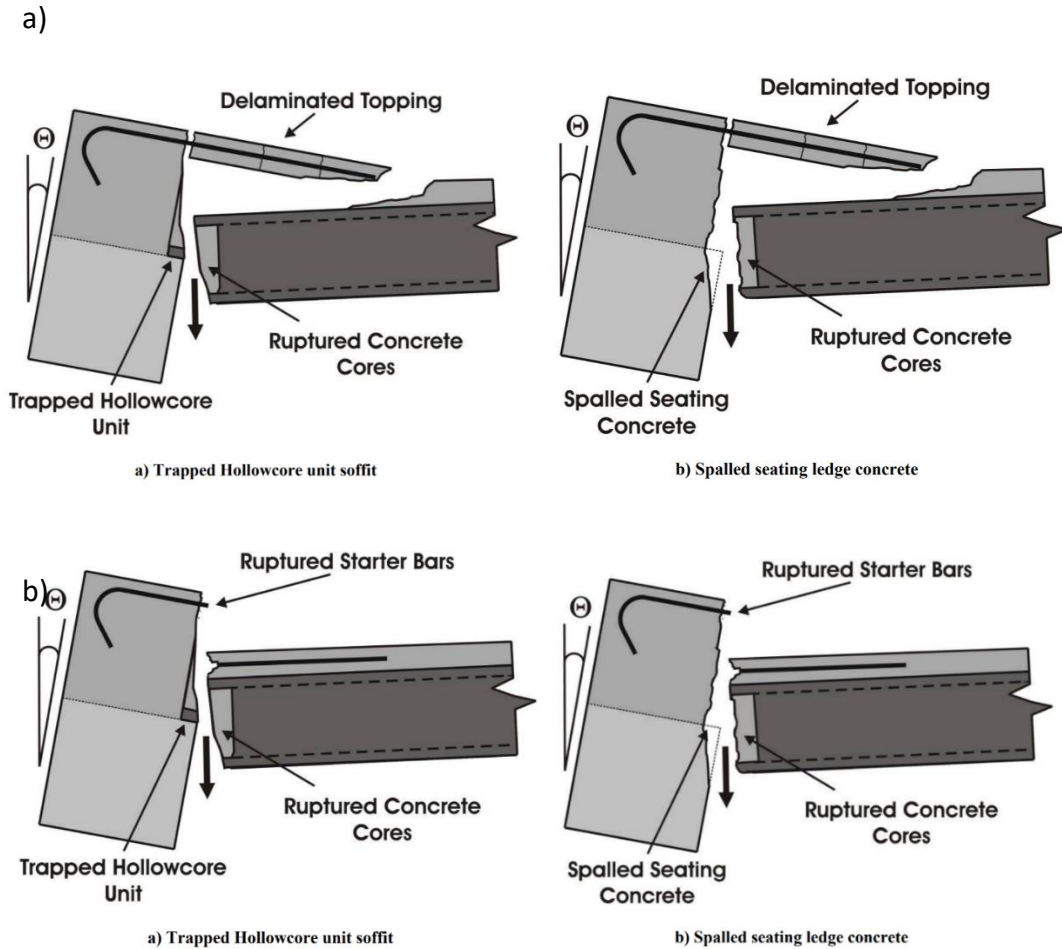


Figure 1.25. Failure mechanisms with (a) and without (b) topping delamination (Jensen, 2006)

1.7.2 Flexure-shear Failure in Positive Moment

The hollow-core slabs are usually assumed as simply-supported elements; however, Matthews (2004) has shown that the fixity between the seating beam and the hollow-core is enough to induce flexure and shear forces which can exceed the hollow-core slab capacity (Jensen, 2006). This failure mechanism starts with flexural cracking on the bottom face (seating face) which then develops into a shear failure with diagonal cracking, as seen in Figure 1.26. This failure mechanism suggests that the strength of the surrounding elements is the dominant variable that induces connection fixity and supplementary core reinforcement induces further fixity in such connections (Jensen, 2006).

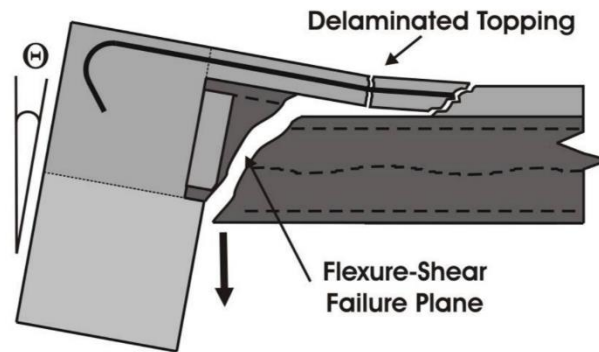


Figure 1.26. Flexure-Shear failure mechanism (Jensen, 2006)

This failure mechanism occurs at the ends of the hollow-core slab, which is the zone where the prestress is not fully developed (development length), and therefore, the designed flexural strength is not achieved in this region. As a result, the flexural capacity of the hollow-core slab is governed mostly by the strength of the concrete, which results in much less strength than the designed flexural strength where prestressing strands are considered (Jensen, 2006). Figure 1.27 shows the flexural-shear failure mechanism investigated by Bull and Matthew (2003).



Figure 1.27. Flexure-Shear Failure (Bull and Matthew, 2003)

1.7.3 Flexure and Flexure-shear Failure in Negative Moment

A hollow-core unit does not usually have reinforcement or prestressed strands on the top flanges. The resistance against a negative moment is provided by the concrete strength and the starter bars in the topping (if a structural topping is placed). Flexural cracks are formed when the tensile capacity of the concrete is surpassed, and the cracks propagate into the hollow-core slab leading to failure, and the weakest point is the section where starter bars in the topping end (Khanal, 2019).

Figure 1.28 shows the flexural failure mechanism.

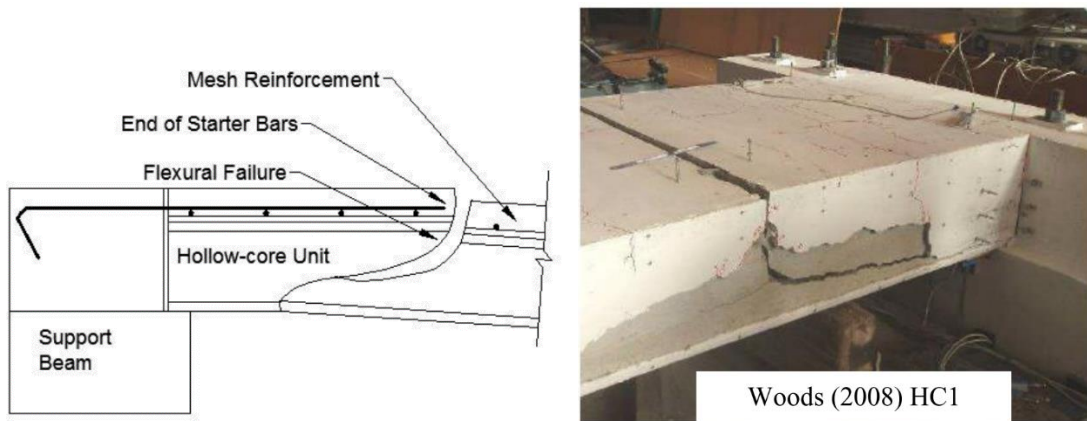


Figure 1.28. (a) Flexure failure mechanism and (b) Flexure failure mechanism (Khanal, 2019).

A flexure-shear failure can occur when steel reinforcement is placed inside the cores and cast with in-situ concrete. This technique is usually used when there is a deficient seating length for the hollow-core slab or when there is no seating available (Jensen, 2006). Figure 1.29 shows the failure mechanism for a seating deficient connection and a no-seating connection (also called negative seating).

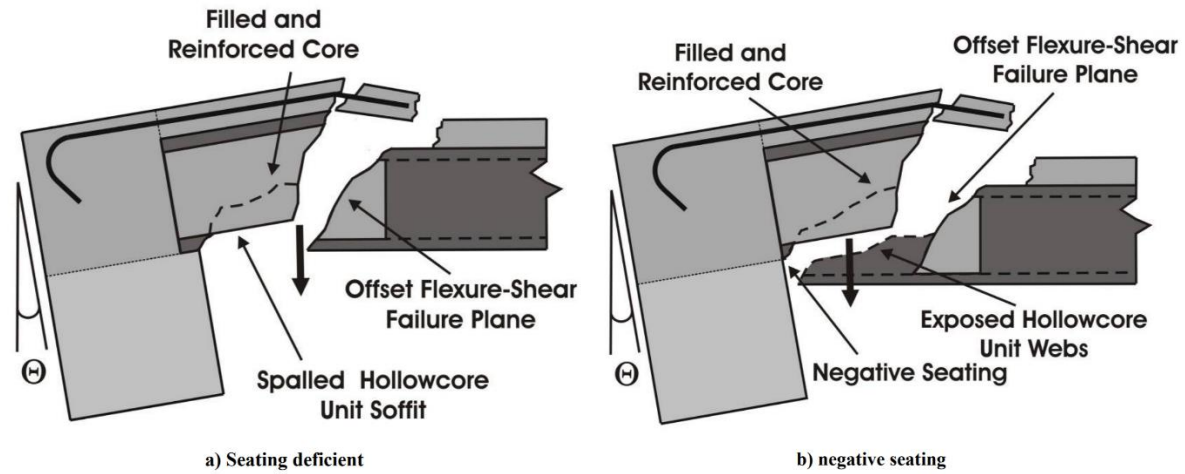


Figure 1.29. Flexure-Shear failure mechanism (Jensen, 2006).

1.7.4 Torsional Failure

Since the hollow-core units do not have transverse reinforcement, torsional cracks occur when the principal tensile stress reaches the hollow-core concrete cracking strength. Once the cracks are developed, the torsional resistance decreases quickly (Collins and Mitchell, 1987). Also, when a crack is developed, the stresses redistribute to the uncracked flanges, leading to all flanges being cracked and the slab behaving like several I-section beams (Khanal, 2019). Figure 1.30 shows the distribution and the redistribution of stresses in a hollow-core unit with torsional effects, while Figure 1.31 shows a hollow-core unit converted to I-beams due to cracks in the flanges.

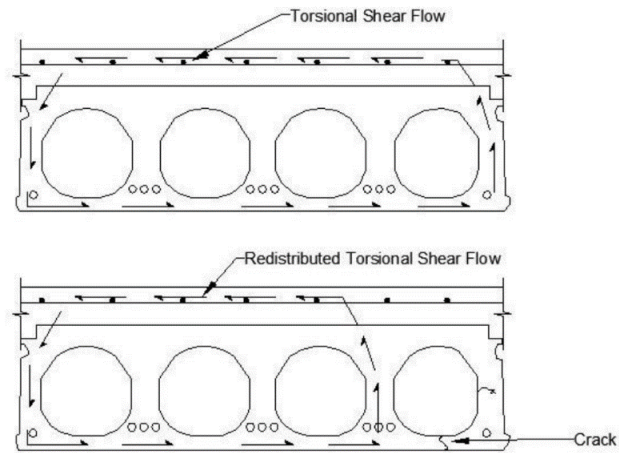


Figure 1.30. Distribution and redistribution of stresses in a hollow-core unit with torsional effects (Jensen, 2006).

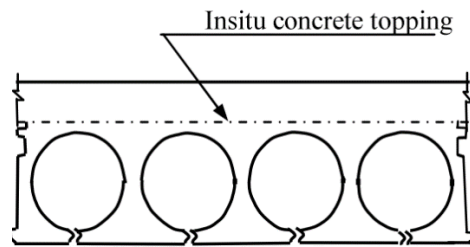


Figure 1.31. Hollow-core unit converted into I beams (Fenwick et al. 2010).

1.8 Objectives

This study is a continuation of a research stream on the development of controlled rocking masonry systems at McMaster University. As mentioned before, the development of ED-CRMWs (Yassin et al. 2022a and 2022b) used flexural arms as dissipation devices which were originally tested by Li (2019) and modelled later by East et al. (2022). Currently, an upgrade of the ED-CRMWs is also being developed and tested. This development includes installing a steel beam at the bottom of a rocking wall to avoid masonry crushing when rocking. Since ED-CRMWs do not make use of post-tensioned strands and rely instead on vertical gravity loads, there is a need to investigate the ED-CRMW-diaphragm interaction at the system-level.

Based on the displacement incompatibilities that exist when considering the interaction between a controlled rocking masonry wall and the diaphragm, the current thesis aims at a better understanding of such an interaction considering the most commonly used slab in current Canadian reinforced masonry construction practice, which is the hollow-core slab. In this respect, the main objectives of the thesis are to 1) identify and classify the potential issues in a rocking system that supports hollow core slabs; and 2) use finite element modelling to identify the expected damage and quantify the displacement capacity for a common case of hollow core slab deformation induced by incompatible wall uplifts. First, the potential wall-diaphragm interaction issues in masonry buildings with rocking walls are described and illustrated in Chapter 2. Next, Chapter 3 provides an overview of the modelling, which is performed using the finite element commercial software ABAQUS with the concrete damage plasticity (CDP) model to represent a non-linear behaviour in the concrete. The thesis then compares the performance of four different hollow-core geometries, three spans, and two different prestresses (only the bottom flange and at the top and bottom flange). Such details are fully described in Chapter 4, along with the results of

this parametric study to facilitate quantifying the displacement that can be accommodated by the considered connections and geometries. Finally, Chapter 5 provides a summary of the findings and suggests some future research directions.

Chapter 2: Potential wall-diaphragm issues in rocking masonry wall buildings

This section provides a summary of the potential issues that the wall-diaphragm interaction in a masonry building with hollow-core slabs (HC) might encounter when rocking walls are being considered in the design. Although the analysis in subsequent chapters focuses on only one of the issues presented in this section, all these issues (Figure 2.1) should be considered during the design stage of any masonry building with rocking walls. All of the situations described here focus on demands related to loading the walls that carry the vertical loads from the one-way hollow core slabs, but the real three-dimensional deformations must also be considered. To avoid unnecessary displacement incompatibility, the walls that do not receive loads from the one-way slab action are assumed to be connected to the hollow core slabs in a way that transfers the lateral seismic forces but does not transfer vertical forces. In addition, out-of-plane deformations of the walls are not considered within the scope of this work.

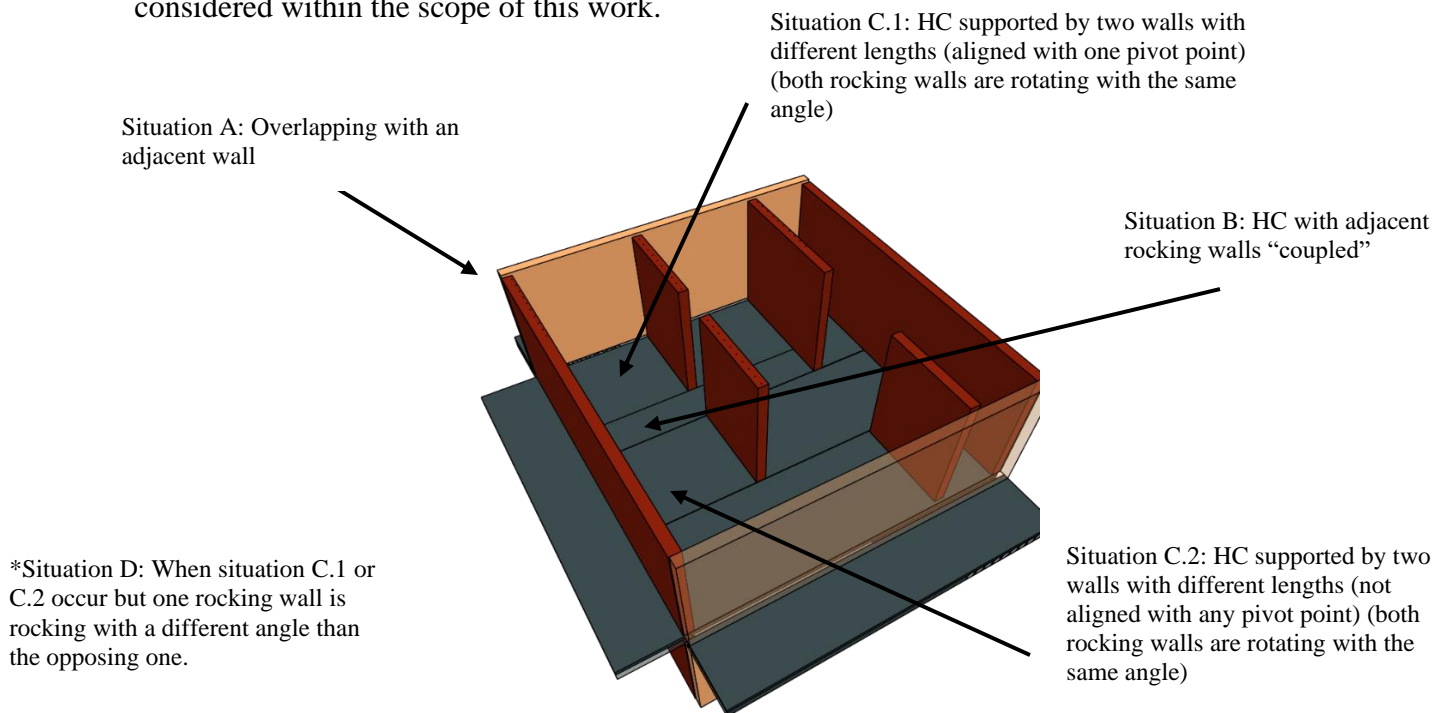


Figure 2.1. Floor plan with potential situations in a masonry building with rocking walls.

2.1 Situation A: A rocking wall with adjacent walls

Figure 2.2. (a) shows an isometric view of a rocking wall between two adjacent walls. The main issue that occurs when the wall rocks is the contact due to its drift, as can be seen in Figure 2.2. (b). This contact occurs along the wall height and also has a potential contact between the hollow cores. This situation must be addressed to prevent unreparable damage that is expected to affect the self-centering capability of the system. The out-of-plane and in-plane drifts of the adjacent walls need also to be taken into consideration. Also, if an adjacent wall rocks, the wall will likely have an out-of-plane base rotation.

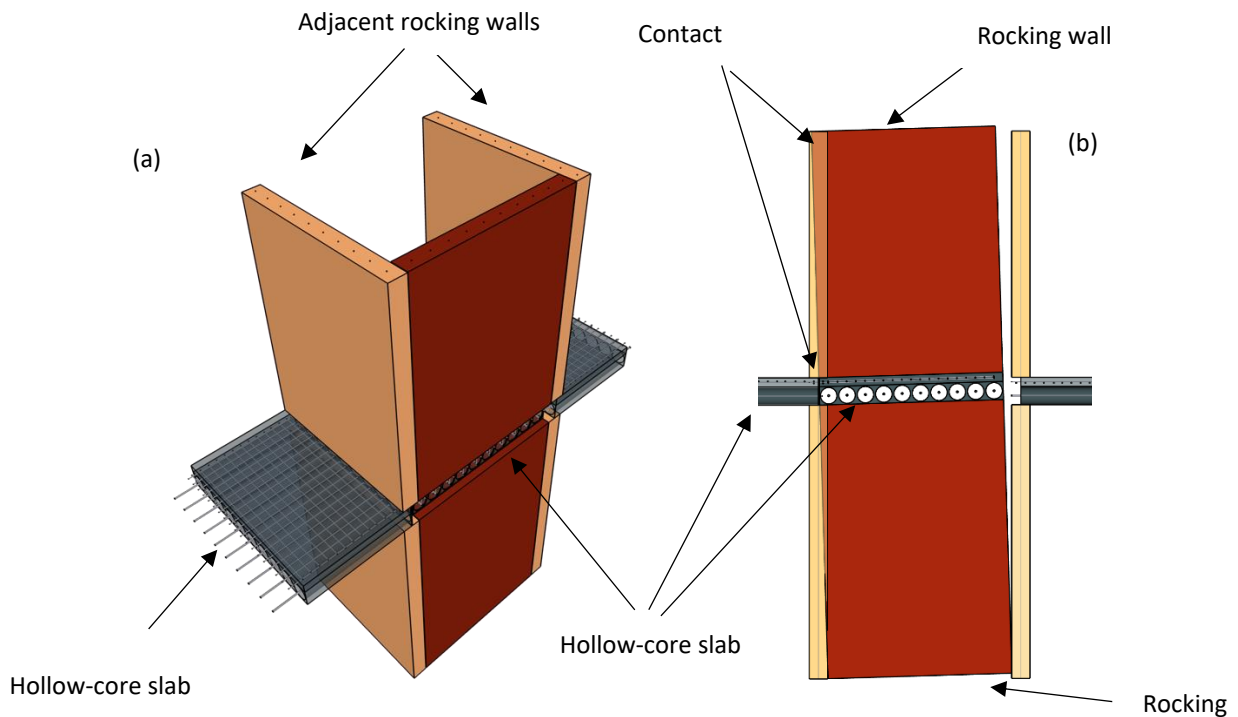


Figure 2.2. (a) Isometric view for a rocking wall with adjacent walls and hollow-core slabs. (b) Elevation view with the pounding/contact due to the rocking of the wall.

2.2 Situation B: Hollow-core units with adjacent pairs of rocking walls

Figure 2.3. (a) shows an isometric view for a hollow-core slab being between two adjacent walls. The slab is being supported by two independent walls whose pivot point (to rotate) could differ from both of the adjacent walls. This could induce different incompatibility of displacements on each end of the slab. These incompatible displacements between the walls can cause damage to the hollow-core slab. This incompatibility can be seen in Figures 2.3. (b) and 2.3 (c).

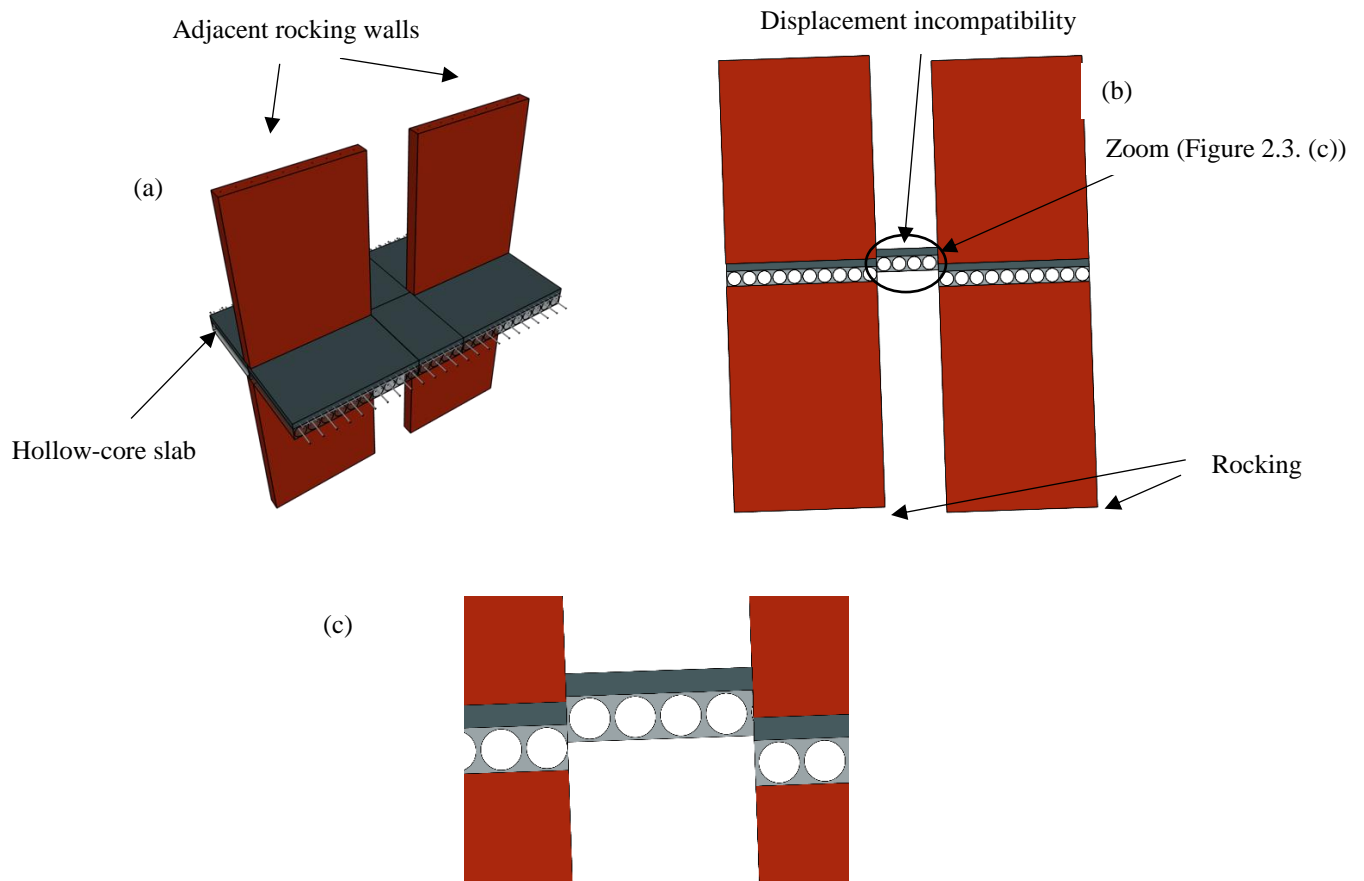


Figure 2.3. (a) Isometric view of hollow-core units with adjacent walls of rocking walls “coupled”. (b) Elevation view shows the rocking of the walls and the incompatibility of displacements between the hollow-cores. (c) Zoom of the displacement incompatibility.

2.3 Situation C.1 and C.2: Hollow-core units supported by rocking walls with different lengths and rocking at the same angle

In a building, it is common that the layout and the sizes of the walls are not fully symmetrical. When the walls that support hollow-core slabs do not have the same length, a displacement incompatibility issue occurs (Figures 2.4 & 2.5). Since the most commonly used connection (Figure 1.5. & 1.6.) can be considered a rigid connection, this leads to a potential failure of the slab at the endings due to the concentration of stresses at the wall-slab edge contact.

When incompatibility of displacements is an issue, there are two different potential situations where the slab suffers from such displacements. These situations depend on how the walls are aligned with each other in a parallel direction. In situation C.1, which is illustrated in Figure 2.4, both walls start/end at the same position and the walls do not have any incompatibility of displacements when they are both rocking from the same pivot point and with the same rotational angle (Figure 2.4. (b)); however, displacement incompatibilities occur when rotating in the opposite direction since the walls do not share the same pivot point due to their different lengths (Figure 2.4. (c)). Situation C.2 occurs when both walls do not share the same pivot point when rocking in either direction (Figure 2.5.). In this case, displacement incompatibilities occur when the walls rock in both directions and with the same rotational angle. The investigation presented in this thesis focuses only on the incompatibility of displacements that situation C induces to the slab. Situation C is a major concern for rocking systems because it occurs when a rigid diaphragm causes all walls to displace the same amount in one direction, assuming rigid body motion of the walls leads to equal rotations in all walls.

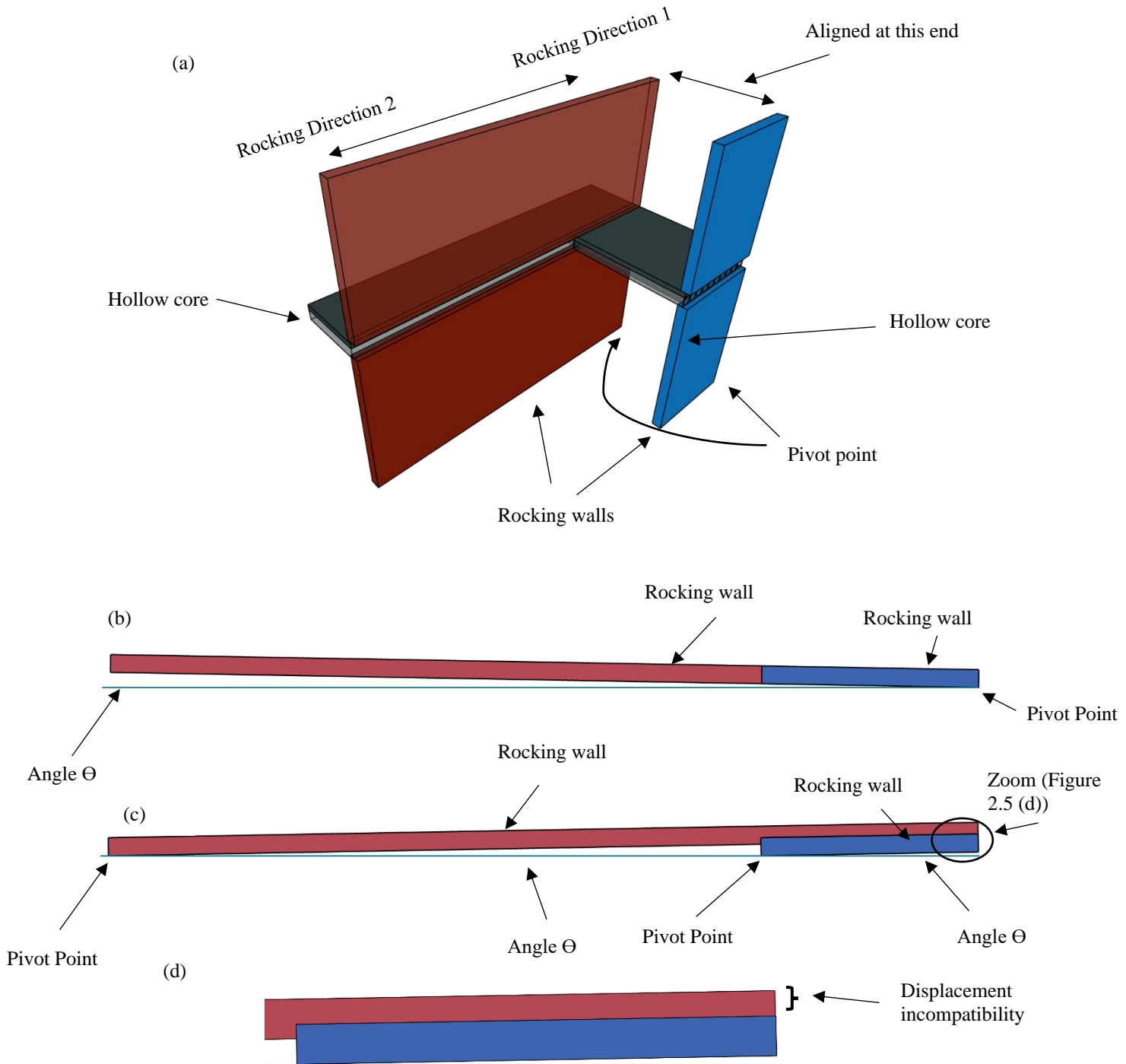
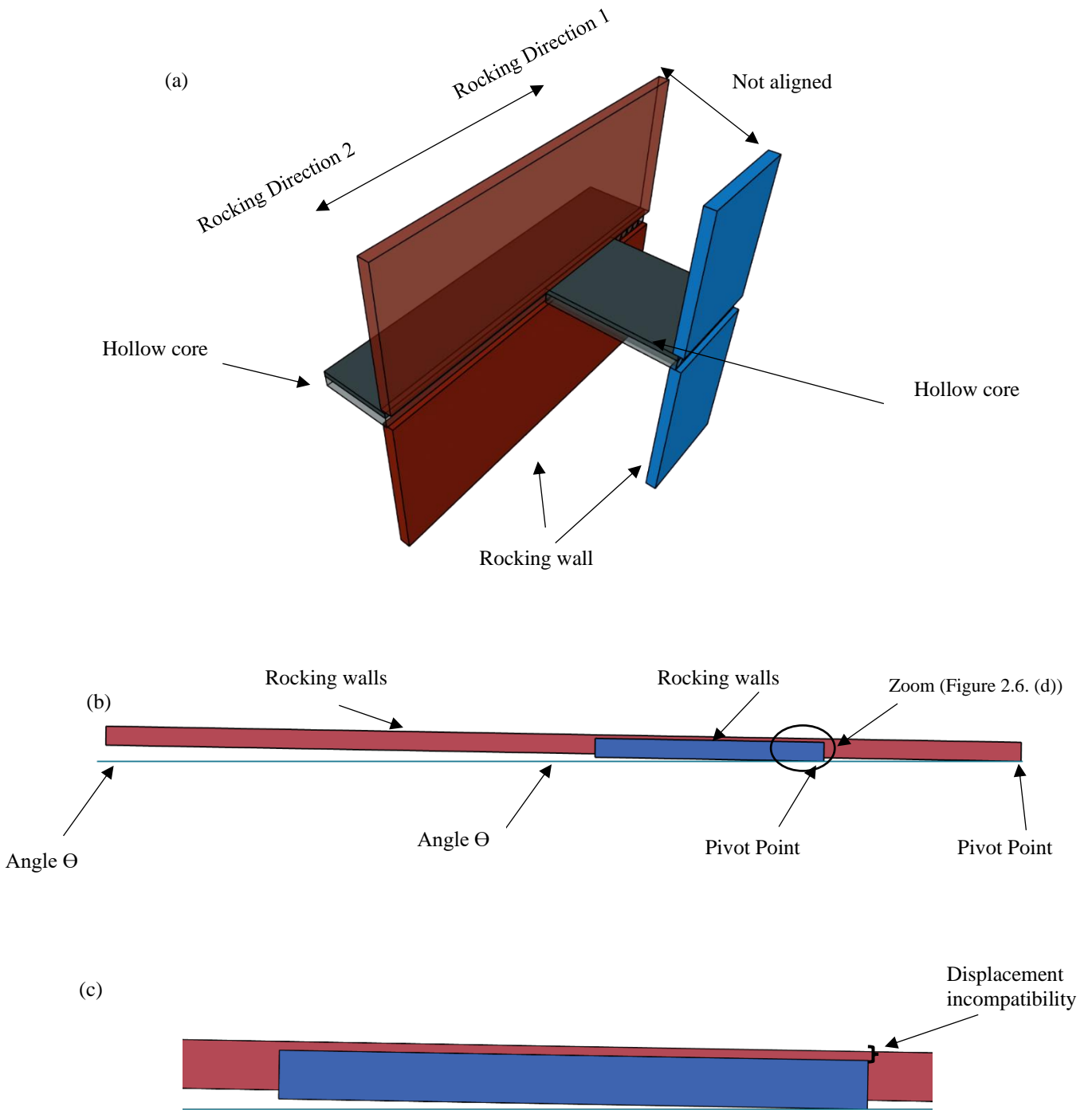


Fig 2.4. Situation C.1: (a) Isometric view of the two walls with different lengths. (b) Top edge elevation views of the two walls with different lengths rocking in direction 1 (on the same pivot point). (c) Top edge elevation views of the two walls with different lengths rocking in direction 2 (on a different pivot point). (d) Zoom of the displacement incompatibility in (c).



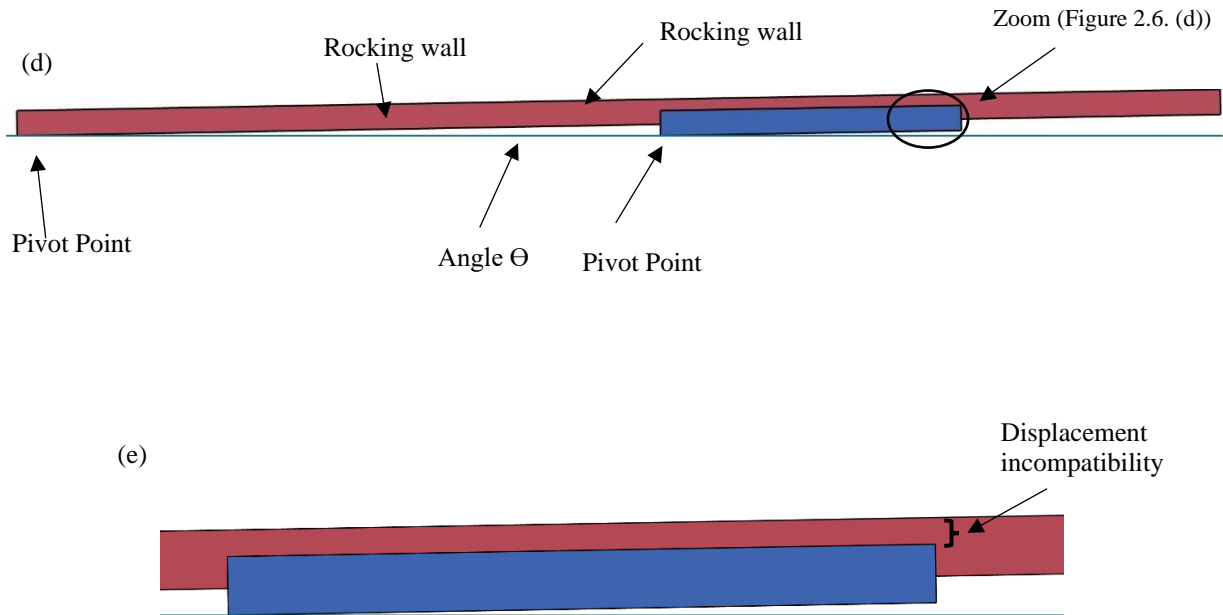


Fig 2.5. Situation C.2: (a) Isometric view of the two walls with different lengths (not aligned). (b) Top edge elevation views of the two walls with different lengths rocking in direction 1. (c) Zoom of the displacement incompatibility in (b). (d) Top edge elevation views of the two walls with different lengths rocking in direction 2. (e) Zoom of the displacement incompatibility in (d).

2.4 Situation D.1 and D.2: Hollow-core units supported by rocking walls rotating at different angles

Walls that support a hollow-core slab and rock at different angles are expected to induce potential vertical displacement/angular incompatibilities and torsional effects. This occurs primarily because of torsional deformations of a building in plan, where a rigid diaphragm assumption implies unequal displacements at different walls in the same direction. In this case, there are two different situations with two different effects on the slab. Situation D.1 occurs when the two rocking walls which rotate at different angles have the same length and share the same pivot points (Figure 2.6.). This will induce only angular-displacement incompatibilities into the slab.

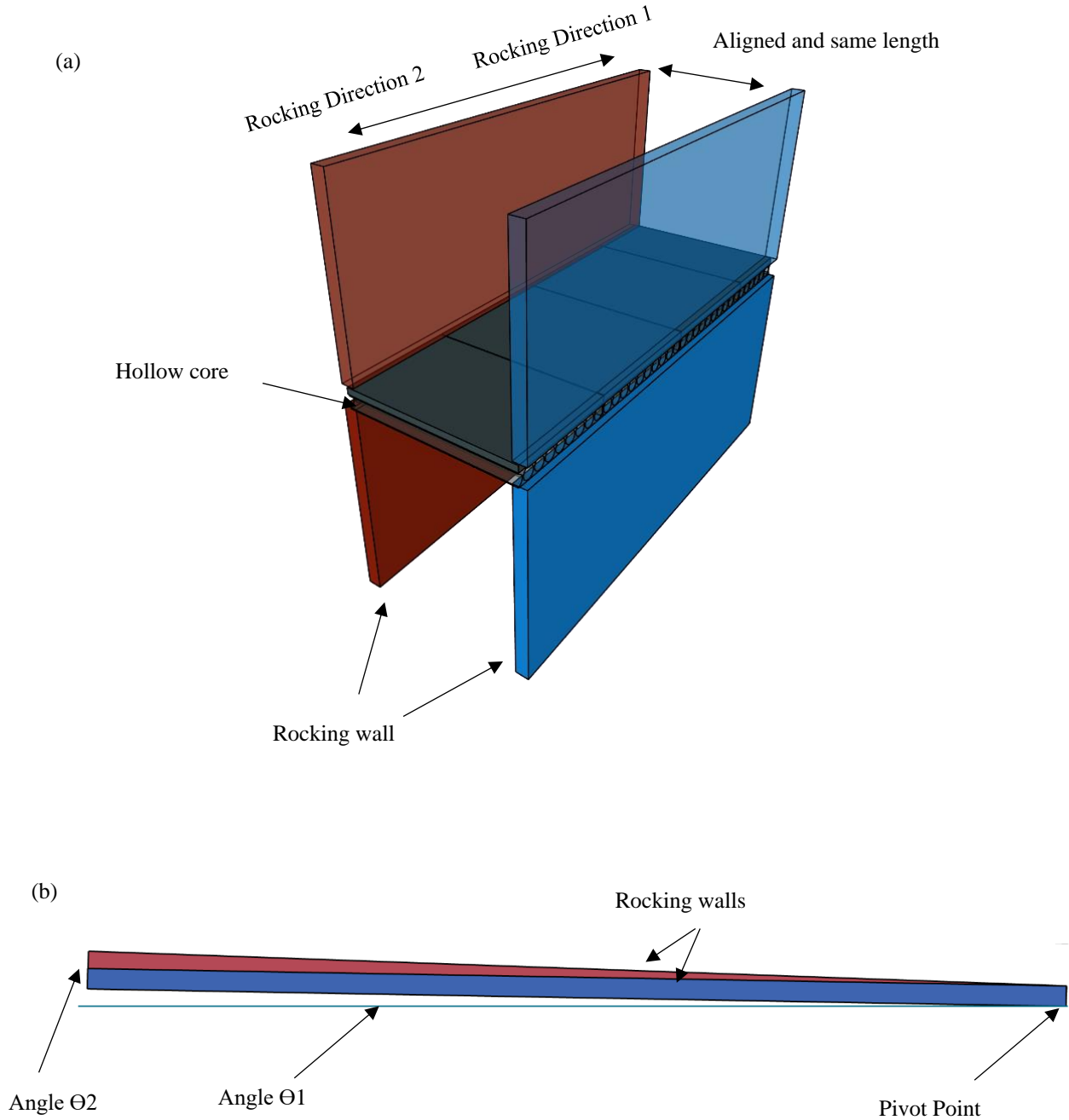
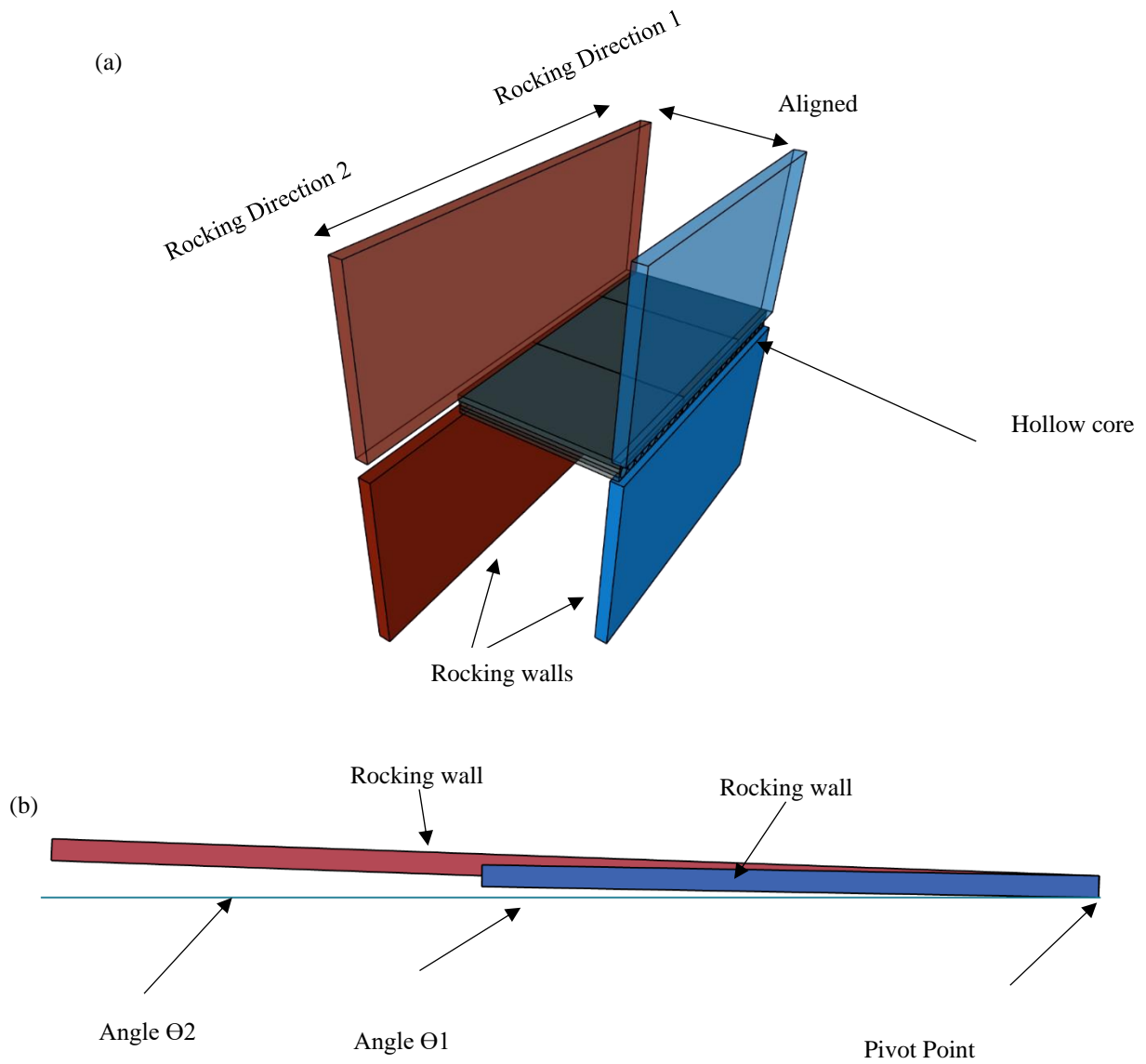


Figure 2.6. (a) Isometric view of the two rocking walls of the same length and aligned with each other. (b) Top edge elevation view of the two walls with the same length and rotating at different angles. $\theta_1 < \theta_2$

Situation D.2 is realized when the two walls do not have the same length while sharing just one (or no) pivot point. This induces angular-displacement incompatibilities when both walls rotate from the same pivot point, but it induces a combination of vertical and angular-displacement incompatibilities when the walls rotate from different pivot points (Figure 2.7 (c) and (d)).



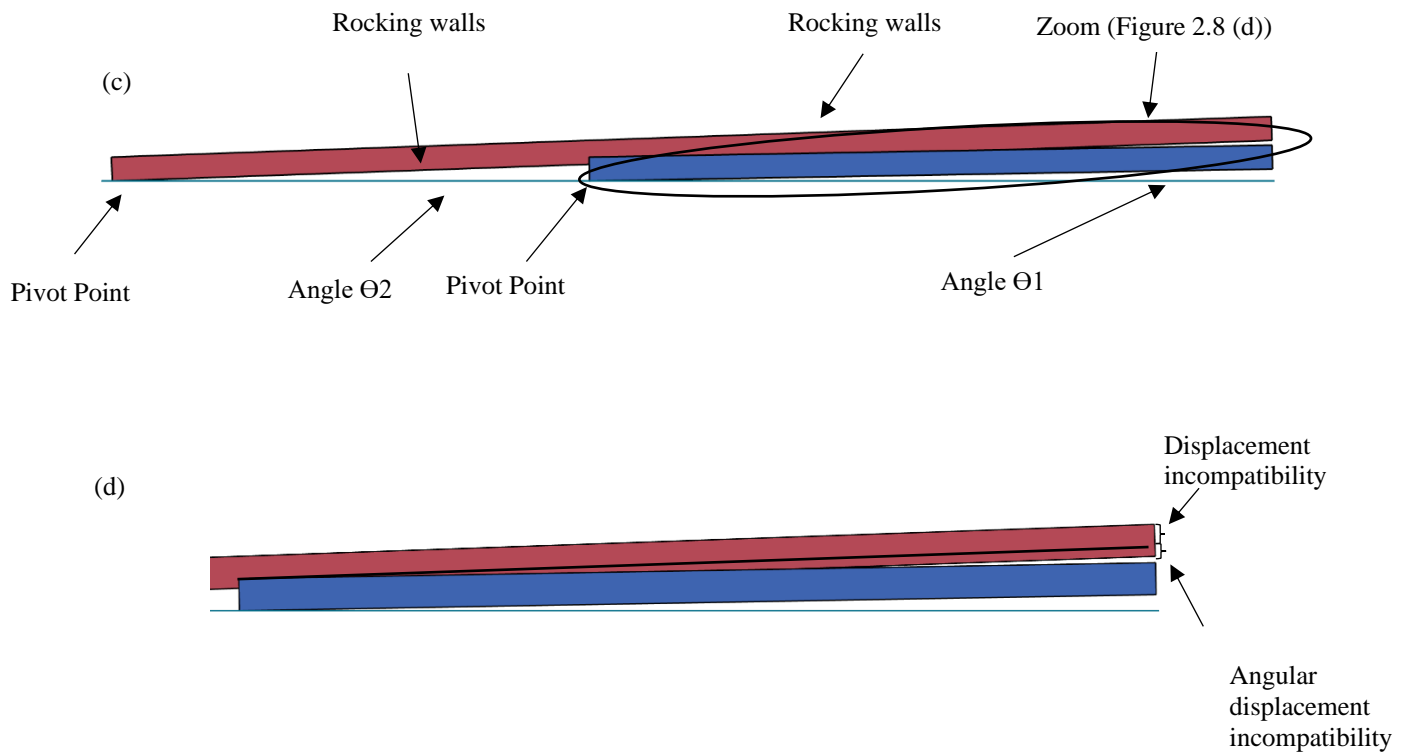
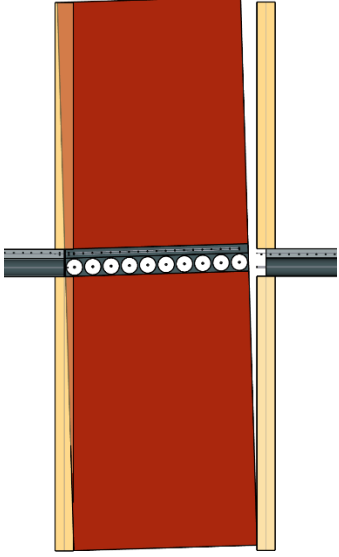
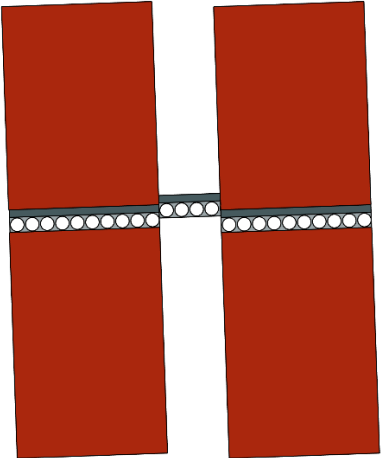
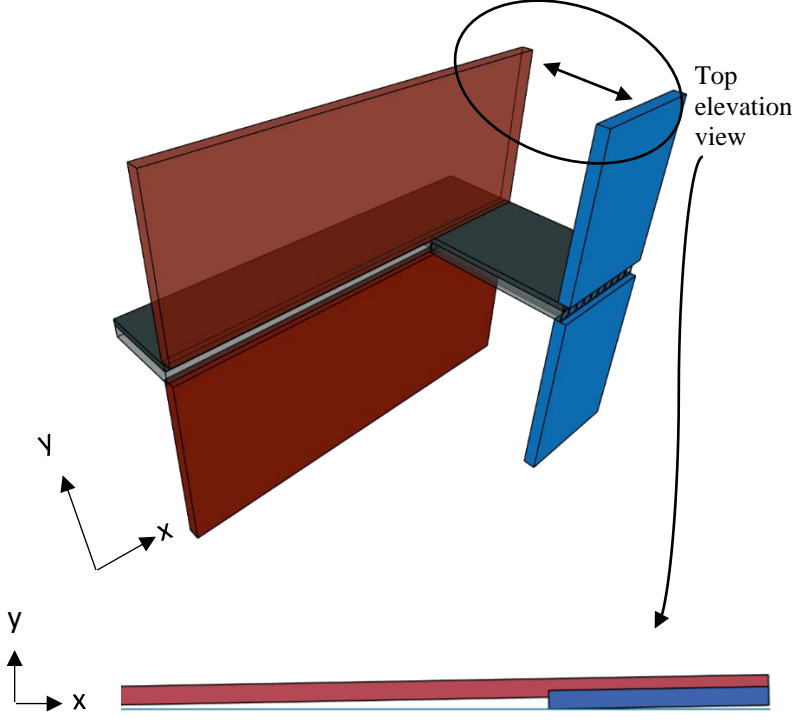
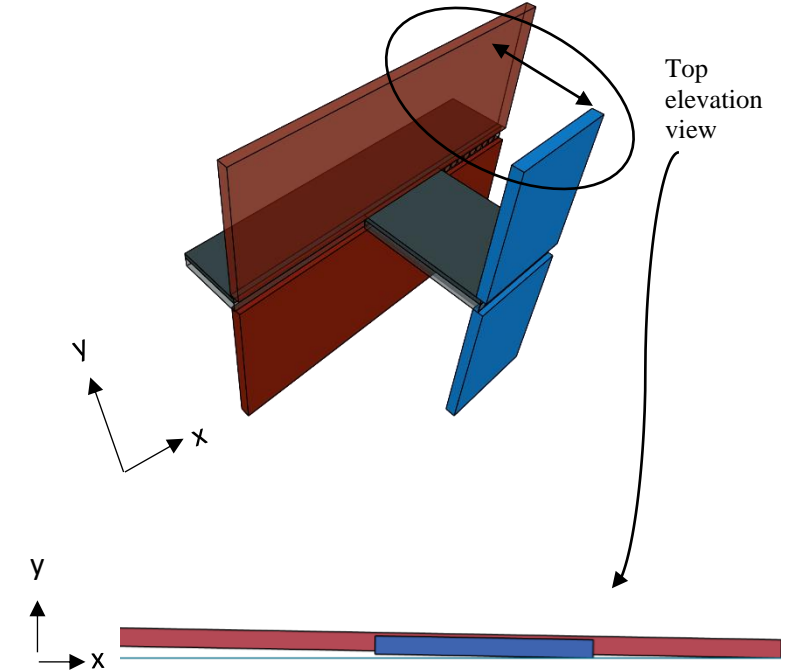


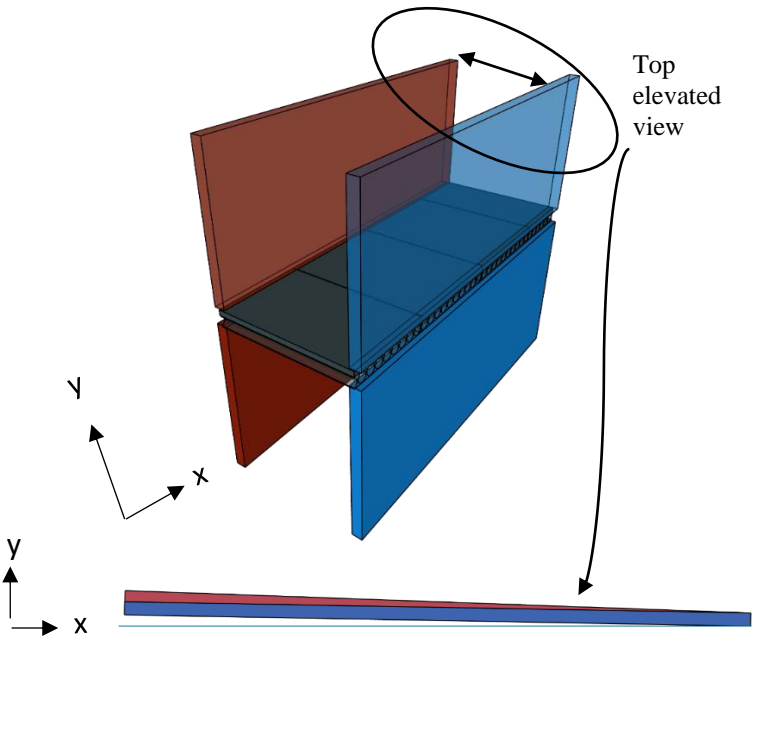
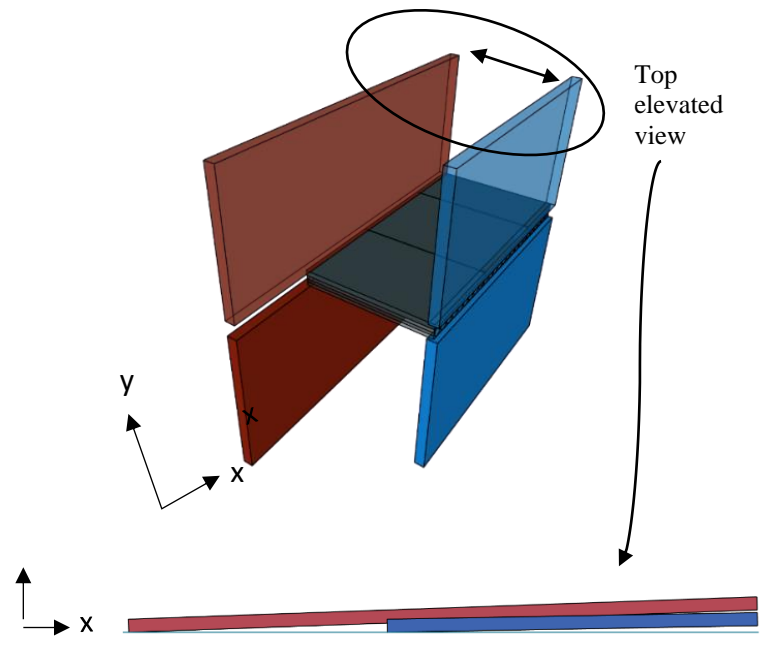
Figure 2.7. (a) Isometric view of the two rocking walls with different lengths and aligned with each other. (b) Top edge elevation view of the two walls with different lengths and rotating in direction 1 when the longer wall rotates at a bigger angle. (c) Top edge elevation view of the two walls with different lengths and rotating in direction 2 when the longer wall rotates at a bigger angle. (d) Zoom of the combination of vertical displacement and angular displacement incompatibilities in (c). $\Theta_1 < \Theta_2$

2.5 Summary

Table 2.1 Summary of situations discussed above.

Situation	Illustration	Potential Issue
A		Contact with adjacent walls due to drift
B		Displacement incompatibility due to different rotational pivot points between walls and intermediate hollow-core slabs

<p>C.1</p>	 <p>Top elevation view</p>	<p>Displacement incompatibility (when rotating in one direction) due to different rotational pivot points between supporting walls. Both walls rotate at the same angle</p>
<p>C.2</p>	 <p>Top elevation view</p>	<p>Displacement incompatibility (when rotating in both directions) due to different rotational pivot points between supporting walls. Both walls rotate at the same angle</p>

<p>D.1</p>	 <p>Top elevated view</p>	<p>Angular displacement incompatibility due to different rotational angles and the same pivot points between the two supporting walls</p>
<p>D.2</p>	 <p>Top elevated view</p>	<p>A combination of vertical and angular displacement incompatibility due to different rotational pivot points between the two supporting walls. The shorter wall rotates at a different angle than the larger wall*</p>

*Depends on the geometry of the walls and the direction of rocking.

Chapter 3: Model Development and Validation

A numerical model was developed in the current thesis to capture the incompatibility of displacements in a hollow-core slab, as presented in chapter 2 (Situation C). This numerical model was developed using ABAQUS 6.18 commercial software (Dassault Systemes 2018). In this chapter, the overall description of the model is in Section 3.1, while Section 3.2 describes the FEM formulation including a full description of the model and the interactions, constraints, element types, material properties, and boundary conditions. Finally, Section 3.3 presents the validation process for the model using previous experimental test results.

3.1 Model overall description

The connection is considered to be a fixed/rigid connection, where the hollow-core slab is supported by a masonry wall and the continuation of the masonry wall lies on top of the hollow-core. All diaphragms need to have boundary reinforcement, which is essential to ensure that the diaphragm can transfer lateral loads to the seismic force-resisting systems such as controlled rocking masonry walls. In addition, collector reinforcement is required in diaphragms to transfer such forces to the masonry walls. These connectors provide structural integrity to ensure a complete load path (Buettner et al. 2015). As seen in Figure 3.1, this connection is assumed to have collector reinforcement which is placed in the keyways between slabs, while the boundary reinforcement is placed between the two opposite hollow-cores within the in-situ topping concrete.

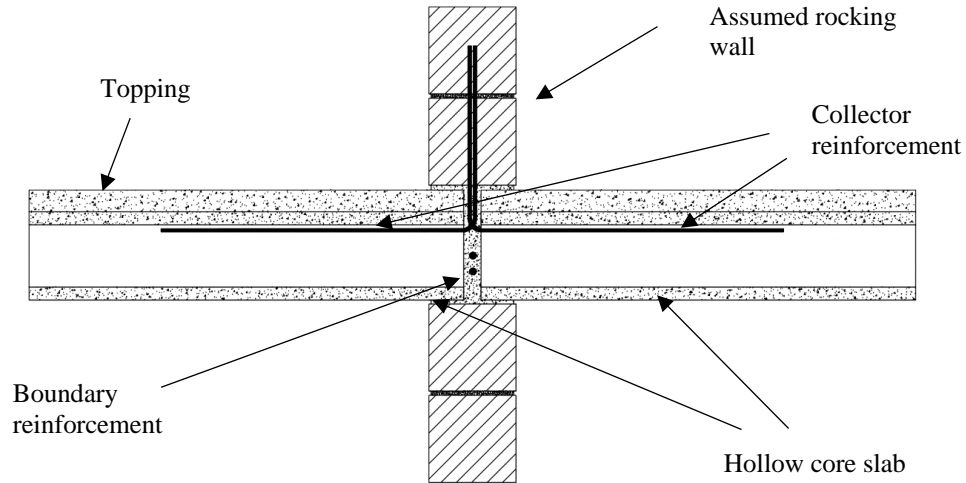


Figure 3.1. Fixed masonry wall – hollow-core connection.

*The diagram is for overall guidance only, specific reinforcement (topping, precast beam, wall) and prestress strands have been omitted for clarity purposes.

The connection was simplified for FEM modelling, as shown in Figures 3.2 and 3.3. This simplification was made since the study focuses on the overall behaviour of the hollow-core slab with vertical displacement incompatibilities.

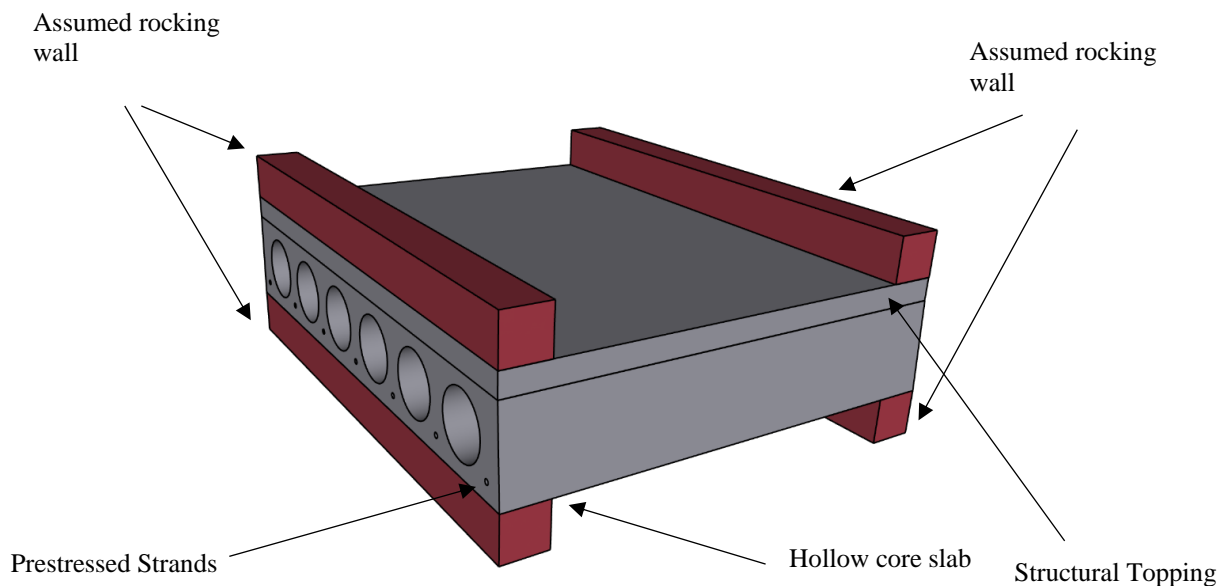


Figure 3.2. Simplified fixed/rigid connection for the FEM formulation.

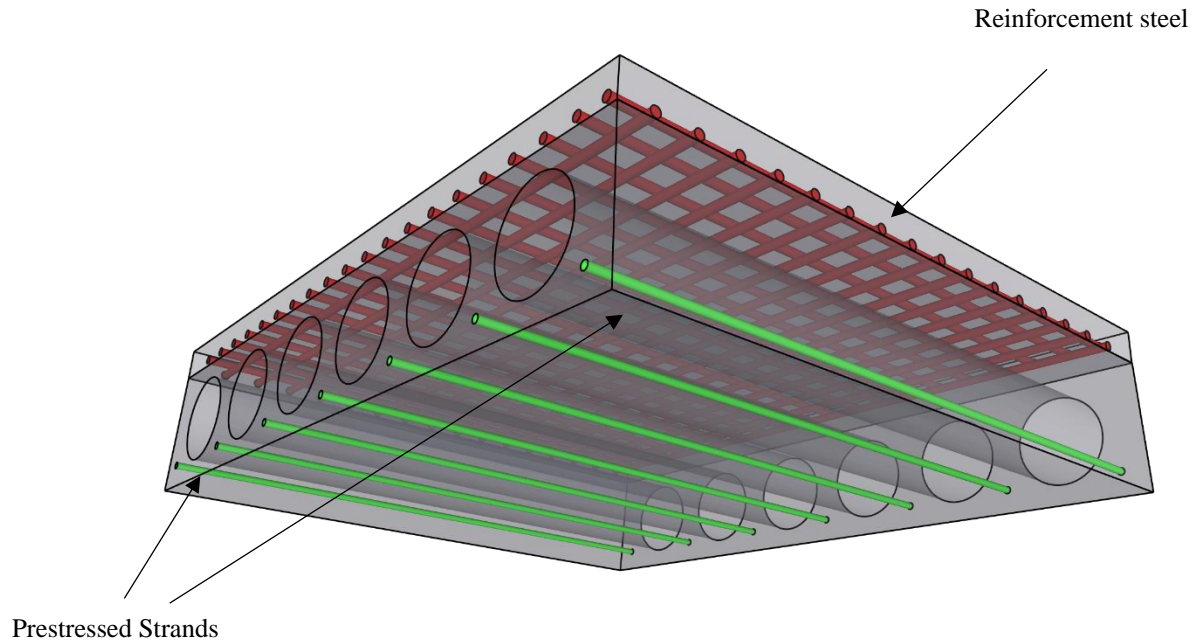
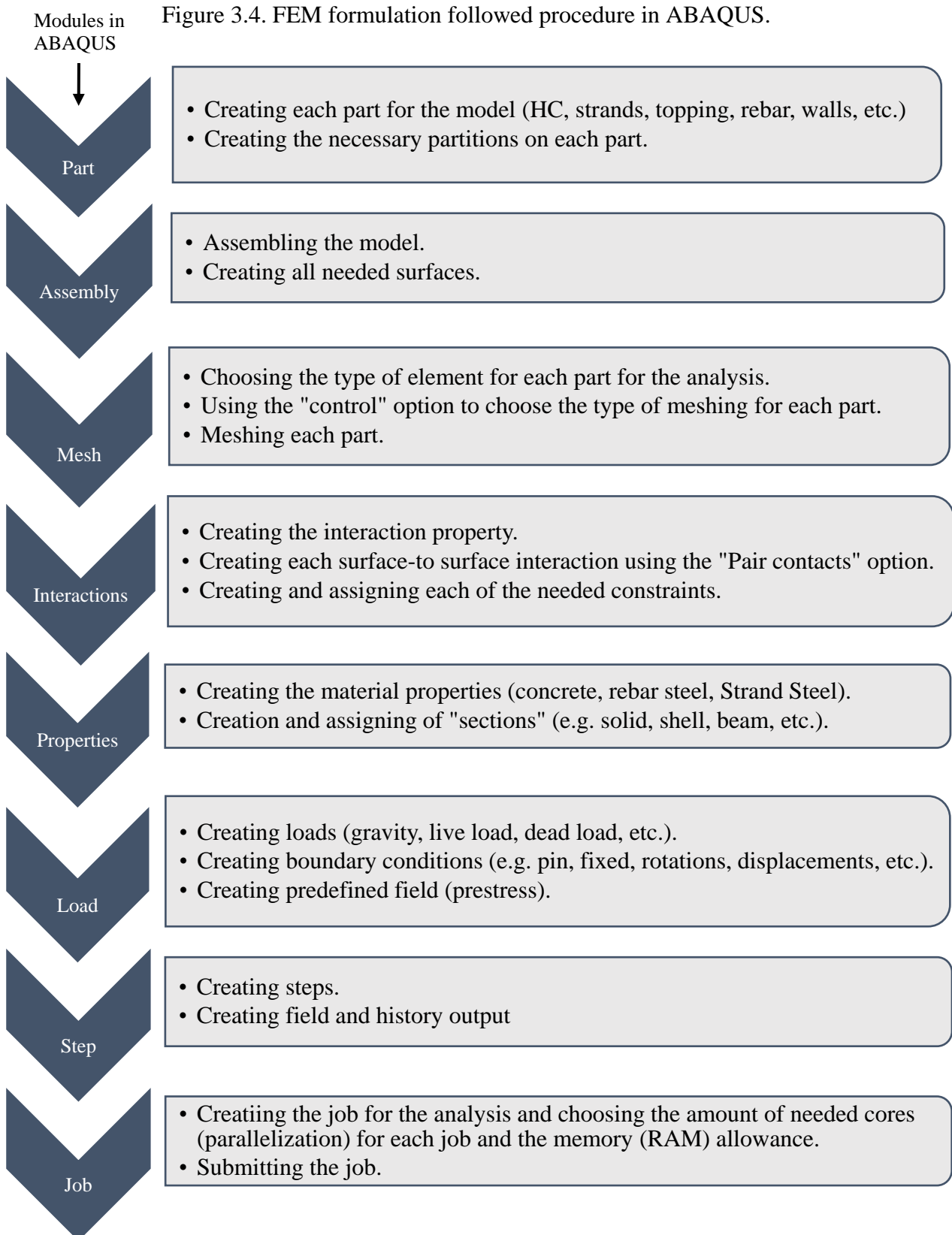


Figure 3.3. Rebar and prestressing steel in the hollow-core slab system.

3.2 FEM Development

The hollow-core slab was modelled using the 3D brick elements available in ABAQUS. The followed procedure was not in the same order as the “modules” in ABAQUS, but in a selected and more efficient order, as shown in Figure 3.4. The slab was partitioned to allow for boundary conditions, interactions, and meshing to be applied in the model in the correct locations, as shown in Figure 3.5. The hollow-core slab was meshed so that the element size was reduced towards its ends. Also, the element size was reduced towards the pre-tensioned strand ducts, as seen in Figure 3.6. This discretization allowed a more detailed mesh in the critical regions of the slab where the most yielding was expected, and it also allowed for proper interactions between the hollow-core slab and the pre-tensioned strands.



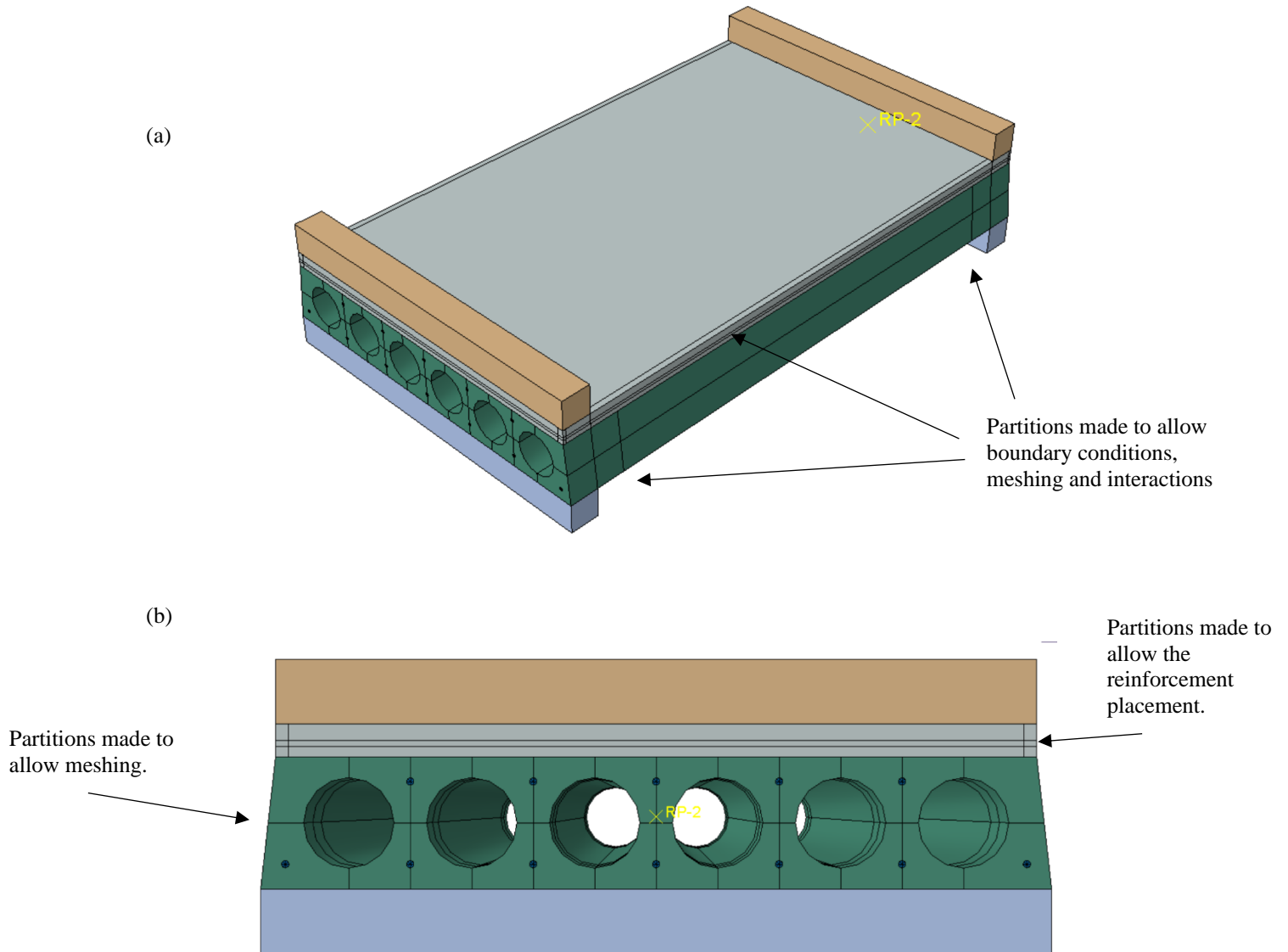


Figure 3.5. Illustrations of a 203 mm hollow-core (with fixed connection) model assembly. (a) Isometric view. (b) Cross-section view.

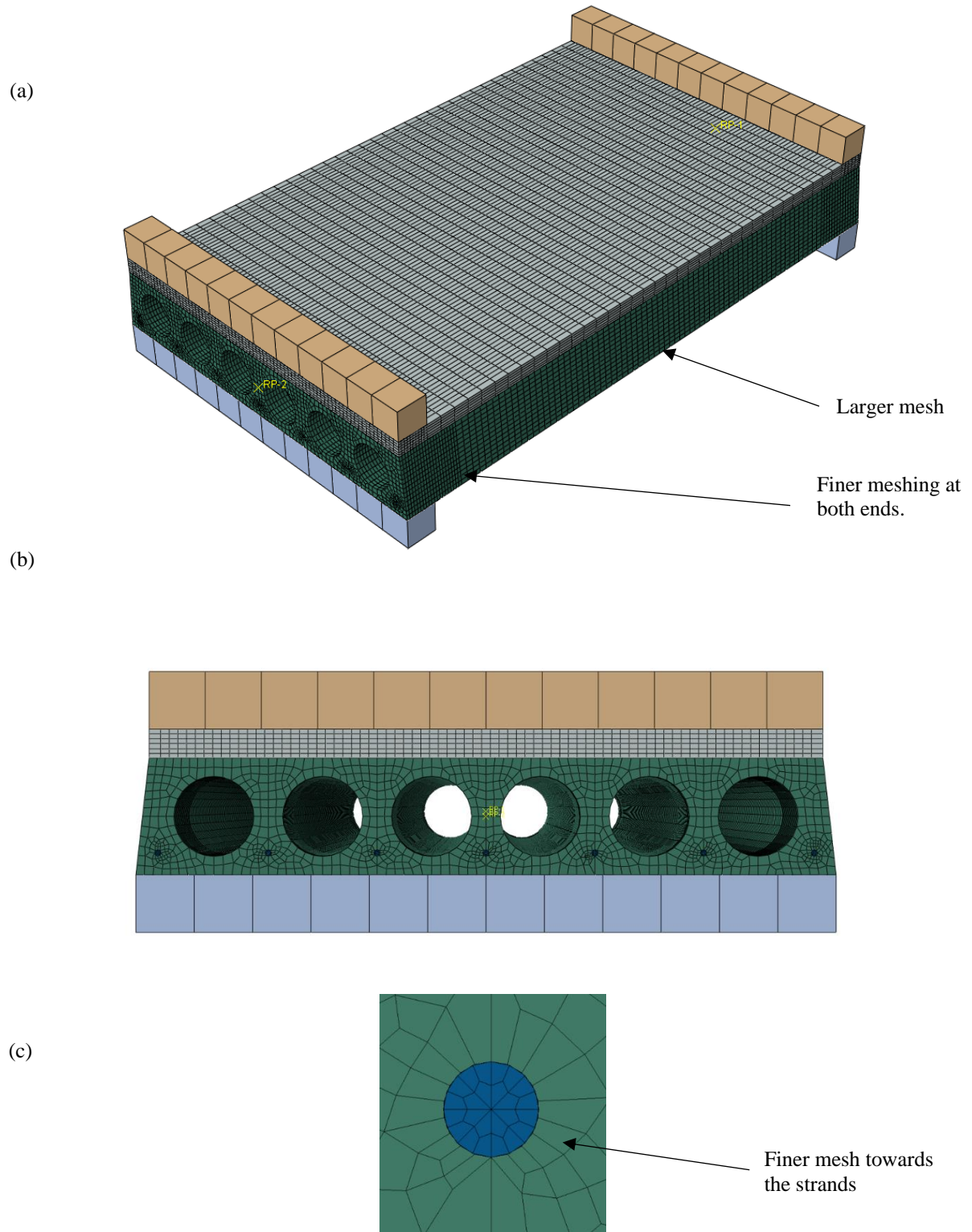


Figure 3.6. Illustration of the meshed 203 mm hollow-core model with fixed connection. (a) Isometric view. (b) Cross-section view. (c) Zoom of a meshed strand cross-section.

The element size close to the hollow-core slab ends was 10 mm and it increased between 50 - 150 mm towards the middle of the hollow-core slab (along the length). The element size along the width and height was 15-20 mm. Finally, the element size on the edge of the strand ducts was reduced to 4 mm. These mesh sizes were chosen based on trial and error to balance accuracy and computational cost.

Brick elements (3D) were used to model the strands to properly capture the “Hoyer effect” in the strand (described later) which approaches a realistic behaviour. The strand was partitioned in order to allow for proper meshing. The element size on the cross-section was 4 mm, thus matching the size that was used along the length of the hollow-core slab to have a proper interaction between both materials. In order to simulate the proper interaction between the strand and the concrete, a surface-to-surface interaction was used and assigned to every strand.

The concrete topping was modelled with the same 3D brick elements as for the hollow-core slab. The topping was partitioned in order to place the rebars and to have a similar mesh pattern as the hollow-core slab. The topping mesh size was reduced towards the ends with an element size of 10 mm and increased to 100-150 mm towards the middle of the span. The topping was tied to the hollow-core slab to prevent any slippage between both concrete elements. The reinforcement bars were modelled as truss elements (2D) and were placed and embedded into the topping.

The rocking walls were simplified to rectangular beams and subjected to the movements that such walls would have, thereby inducing the displacement incompatibilities between such walls and the hollow-core slab. Such beams were tied to the top of the topping and the bottom of the hollow-core slab and the appropriate boundary conditions were applied, as discussed in Section 3.2.3.

During the first step of the analysis, the prestress was applied to the strands and the gravity load, and the interactions between the strands and the surrounded concrete were activated. In order to prevent the prestress from affecting the topping, an interaction was created to momentarily “disappear” the topping and the walls. This interaction is called “model change” and it suppressed the topping before re-appearing it in the second step of the analysis after the prestress was applied. During the second step of the analysis, the displacement incompatibility was considered by applying displacements at a reference point that was tied to the walls at the moving end, while the other end was fixed, as described in detail in Section 3.2.3.

Even though explicit analysis could have been used, the computational cost of the model would have increased substantially because this analysis type performs a large number of small-time increments using a central-difference time integration rule, which typically improves the convergence issues, but a high computational cost is expected. Also, the inertia forces would have needed to be taken into consideration and the initial stress condition for the strands would not have been possible for the explicit analysis. Instead, the implicit solver in ABAQUS was used herein. The implicit solver uses Newton’s method solution techniques to solve the nonlinear equilibrium equations which are generated in the analysis, which is particularly useful for nonlinear static analysis where the inertia forces can be ignored. According to the literature, using the implicit analysis solver is successful when performing nonlinear quasi-static analyses (Liu, 2016 and Henry, 2011).

3.2.1 Interactions and constraints

The assemblage module in ABAQUS facilitates building a model by placing the elements needed in the correct place. However, to have a proper model that delivers accurate results, the interaction module has different types of options (e.g., general contact, surface-to-surface contact, self-contact, model change, etc.). Also, every interaction must be assigned to a specific step of the simulation in order to initiate the interaction at the desired time. Furthermore, ABAQUS has several constraints, including tie, coupling and embedded which are used in this study to make the model behave as needed.

Concrete-Strand Interaction properties

In this model, special surface-to-surface contact interaction (Figure 3.7) was used for the interaction between the prestressed strands and the surrounding concrete. The concrete-strand interaction is a contact behaviour, where the tangential behaviour, normal behaviour and cohesive behaviour should be considered. Each of them has a specific role and the corresponding parameters were chosen herein based on the literature. In the tangential behaviour, the coefficient of friction was assumed as 0.4 (Yapar et al. 2015). Since the strands do not penetrate the surrounding concrete, “Hard contact” was assigned for the normal behaviour. The cohesive behaviour was also used to model the interface behaviour and can be used for modelling a permanently bonded interface which was the case for the interaction between the prestressed strands and the concrete. The cohesive behaviour allows for specifying the interface stiffness representative of the physical behaviour or the default parameter in ABAQUS could also be chosen. When choosing cohesive behaviour, uncoupled or coupled traction-separation behaviour can be chosen. In this model, the uncoupled traction-separation behaviour was used which is also

the default option for ABAQUS. This means that the pure normal separation does not affect the cohesive forces in the shear direction and pure shear slip with no normal separation does not affect the cohesive forces in the normal direction. For this specific traction-separation behaviour, the stiffness components of the interface could be specified if needed.

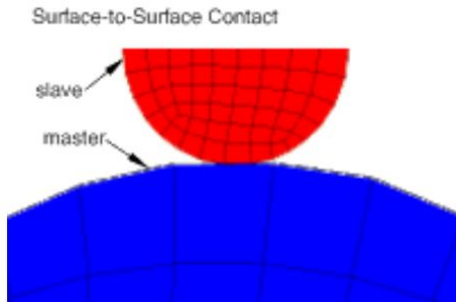


Figure 3.7. Surface to surface contact, (ABAQUS (6.14)).

Turon et al. (2005) suggested the following equation to calculate the interfacial stiffness of a bond using the cohesive behaviour approach,

$$K = \frac{\alpha E}{t} \quad (3.1)$$

Where t is the thickness of the adjacent element, E is the Modulus of Elasticity and α is much larger than 1. The interface stiffness may cause convergence issues if it has a very large value. To avoid that, it is suggested to take $\alpha = 50$ (Turon et al. 2005).

The default option in ABAQUS, which automatically calculates the interface stiffness between the surfaces, was tested against the value obtained from equation (3.1) and the values differ by less than 0.5%, as shown in Figure 3.8. By specifying the interface stiffness (K), the computational expense was lowered by 30%. Therefore, it was decided to move forward with calculating the value of K using Eqn. (3.1).

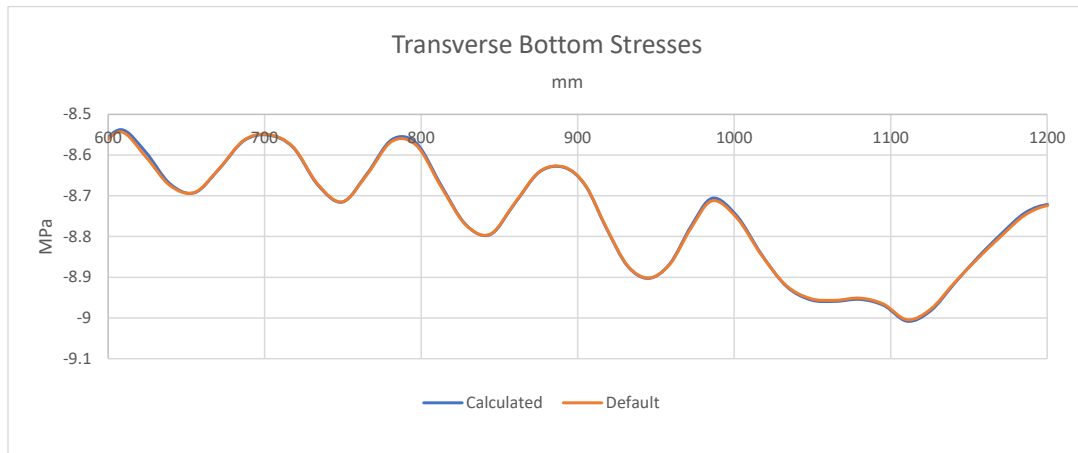


Figure 3.8. Comparison of stresses between default and calculated interface stiffness of a hollow-core (HC 203), with core diameters of 139 mm and 7 – 12.7 mm diameter strands with a prestress of 700 MPa

Table 3.1 Summary of the concrete-strand interaction properties

Tangential behaviour	Coefficient of friction = 0.4
Normal Behaviour	Hard contact
Cohesive Behaviour	Uncoupled, $K = \frac{50 \cdot E}{t}$

Constraints

First, the “Rigid body” constraint was used on the rocking walls to ensure a uniform deformation on the slab when applying the vertical displacements. Also, to simulate the attachment between the wall and the hollow-core, the “tie” constraint was used to create a permanent bond between these two surfaces and prevent their relative displacements. Finally, the “embedded” constraint was used on the reinforcement steel to confine it inside the host element (topping).

Table 3.2 Constraints summary

Part of the model	Type of constraint
Rocking walls	Rigid Body
Embedded rebar in concrete (host)	Embedded
HC-Wall contact, HC-topping contact	Tie (surface to surface approach)

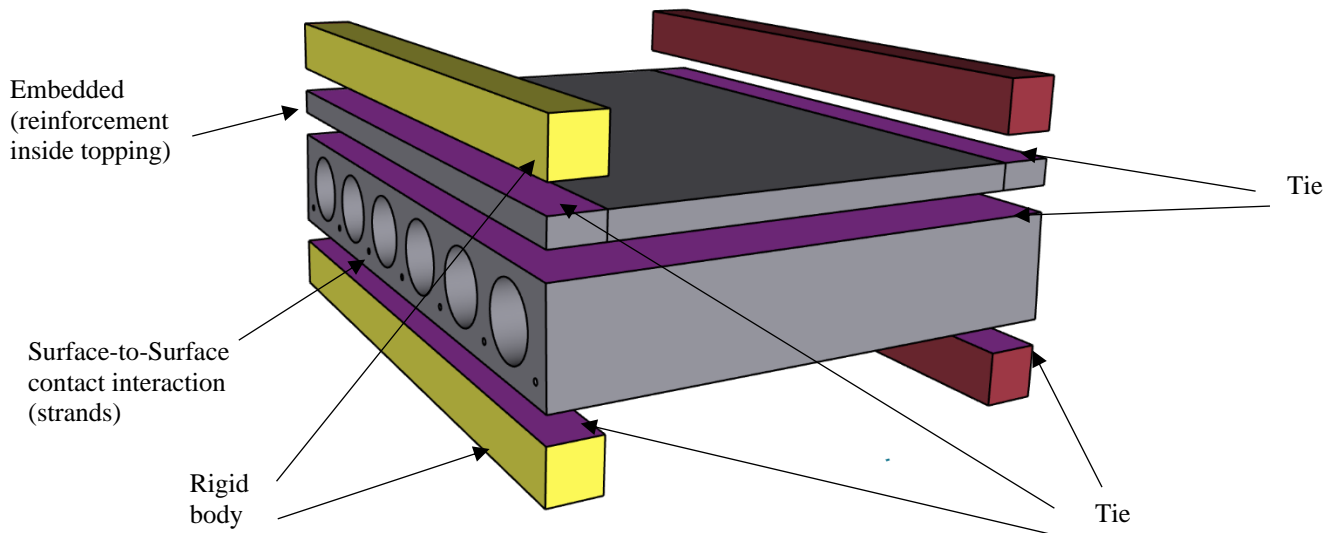


Figure 3.9. Assigned constraints to the model.

3.2.2 Element Type

Concrete (HC, topping and walls)

The concrete was modelled with brick elements (3D) in ABAQUS. This element was selected herein because of its ability to capture the complex nonlinear behaviour due to plasticity, contact and plastic deformations such as cracking and crushing, (ABAQUS (6.14)). The reduced integration was used because fully integrated elements behave poorly for plastic behaviour as they underpredict deflections due to “shear locking”. This is because fully integrated solid elements are too stiff in bending, (ABAQUS (6.14)). The hollow-core slab, topping and walls were modelled using concrete material models.

Strands

The pre-tensioned strands in the hollow-core slab were simulated using 3D elements. It was found in the literature that some researchers have modelled strands using truss elements (3D-2-node) which can only transmit axial forces. However, such truss elements cannot represent one of the main stress transfer mechanisms which is called the wedge effect or Hoyer effect (Yapar et al. 2015). When the strand is tensioned, its diameter decreases (Poisson effect). When the strand is released, it attempts to return to its original size. In the area where the strand is not encased by concrete, the strand returns its original diameter. On the other hand, beyond the transfer length, where the prestressing has been developed, the diameter remains at its stressed diameter. In the zone where the prestressing forces are not fully developed, the stress is reduced and as the strands restore their initial diameters, radial forces develop along with the concrete-strand interaction, as shown in Figure 3.10. (Briere et al. 2013). Cracks at the bottom ends of the slab are usually linked to the two typical stresses in the transmission region, namely splitting and bursting. Splitting cracks generate traction stresses in the concrete while bursting cracks are generated by the strand slippage into the slab (Parkhats 2018).

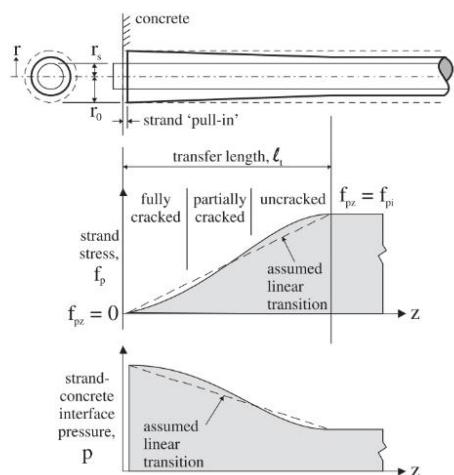


Figure 3.10 Representation of the Hoyer effect (Briere et al. 2013)

Reinforcement bars

The reinforcement bars in the topping concrete were represented by truss elements (3D-2-node). These reinforcement bars were embedded (constraint) in the topping. With this constraint, the bars did not need any independent interaction to simulate the reinforcement inside any concrete.

3.2.3 Prestress and Boundary Conditions

The loads and boundary conditions were assigned in the “load module” in ABAQUS. Three different approaches were used in this model to simulate the boundary conditions, loading and prestress forces. Also, every single boundary condition must be carefully assigned to a specific step of the simulation.

Prestress loading

The prestress forces were assigned using the option “Predefined fields” in the “load module”. The prestress losses depend on different factors (e.g., anchorage slip, friction loss, relaxation of tendons at transfer, elastic shortening, creep, shrinkage, relaxation of tendons after the transfer, and the ambient relative humidity), (CSA Group (1), (2019)). The commentary on the Canadian Highway Bridge Design Code provides approximate values of lump sum losses that are useful for preliminary design, as shown in Table 3.3. These losses are based on the highest allowable transfer stresses considering Grade 1860 low-relaxation strands, (CSA Group (4), (2019)). According to the following table, 260 MPa is the estimate of total prestress losses, which corresponds to approximately 20% of the applied prestress. As a reference for Table 3.3, REL₁: relaxation of tendons at transfer, ES: elastic shortening, CR: creep, SH: shrinkage, and REL₂: relaxation of tendons after transfer.

Table 3.3 Estimate of lump sum losses (MPa) (CSA Group (4), 2019)

		Pretensioning	Post-tensioning
	REL_1	10	—
	ES	110	20
At transfer	$\Delta f_{s1} = REL_1 + ES$	120	20
	CR	80	55
	SH	40	35
	REL_2	20	30
After transfer	$\Delta f_{s2} = CR + SH + REL_2$	140	120
Total Δf_s	$\Delta f_{s1} + \Delta f_{s2}$	260	140

The prestress is applied to the strand as normal stress is perpendicular to the cross-section of the strand. The applied prestress corresponds to 70% of the tensile strength of the strand, which is the used prestress percentile in hollow-cores in the CPCI design manual 5th edition. This is also less than the stress limit of 74% of the tensile strength permitted by the Design of Concrete Structures, CSA group (1), (2019).

Boundary conditions

Boundary conditions were used to simulate the prestress and the incompatibility of displacements on the walls. For the prestress step, boundary conditions of $U1=U2=0$; $UR3=0$ were applied to the hollow-core ends to consider the prestress effect on the slab (Figure 3.11). The boundary conditions for the prestress step are summarized in Table 3.4.

Table 3.4 Summary of the boundary conditions for the prestress step.

Parts or surfaces	Boundary condition
Walls & Topping	N/A
HC (Ends surfaces)	($U1=U2=0$; $UR3=0$)

* $U1=X$, $U2=Y$, $U3=Z$ (axis)

Due to the nature of the prestress forces acting only in the z-direction, this boundary condition allowed the slab to fully deform on the z-axis. For the second step (displacement incompatibilities), the above boundary conditions were changed to “Inactive” because the prestress forces were fully developed and otherwise it would create an incorrect assumption by preventing movements to the U1, U2 and UR3. Since the model has a fixed-fixed connection, one end is fixed in all directions, while the other end restrains all directions with the exception of the vertical direction (U2) to allow the needed displacements, as seen in Figure 3.12. The “loading” was applied as displacements to the reference point RP-2, as shown in Figure 3.13. The reference point was linked to the “rigid body” constraint that was applied to the beams at the end of the slabs. A summary of the boundary conditions used for this model at the displacement incompatibility step is presented in Table 3.5.

Table 3.5 Summary of the boundary conditions for the displacement incompatibility step

Part or surfaces	Boundary condition
Fixed wall	Fixed ((U1=U2=U3=UR1=UR2=UR3=0)
Displacement wall	U2=Vertical displacement
Displacement wall-restrictions	U1=U3=UR1=UR2=UR3=0
HC (Ends)	Inactive

*U1=X, U2=Y, U3=Z (axis)

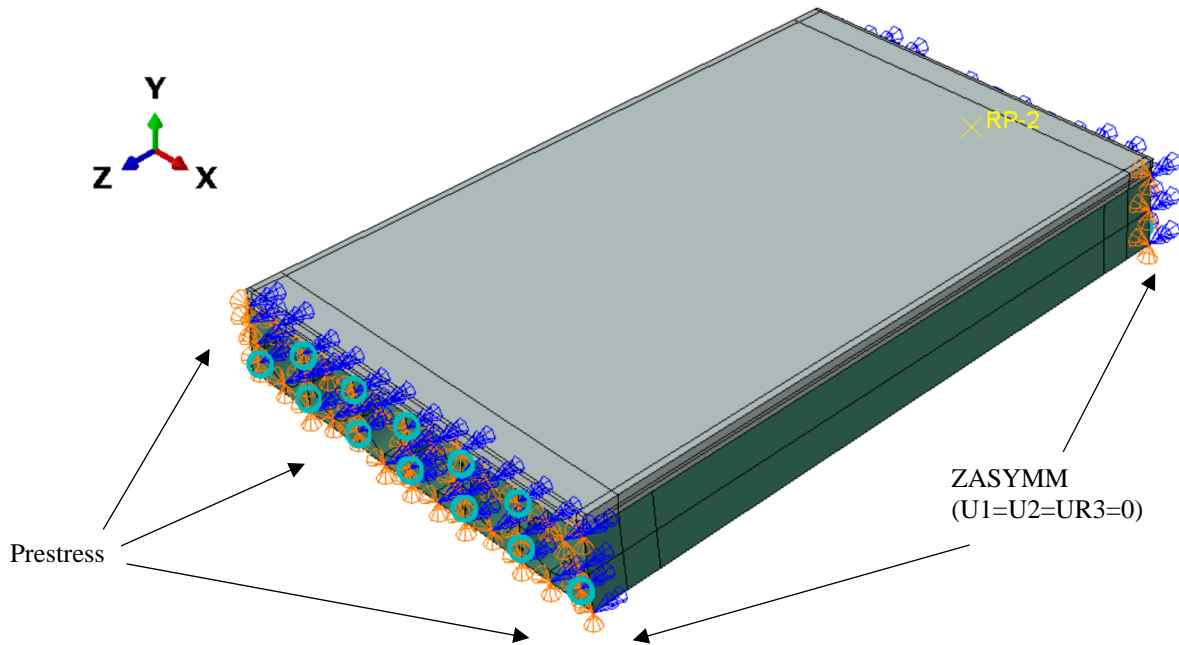


Figure 3.11. Boundary conditions at the prestress step

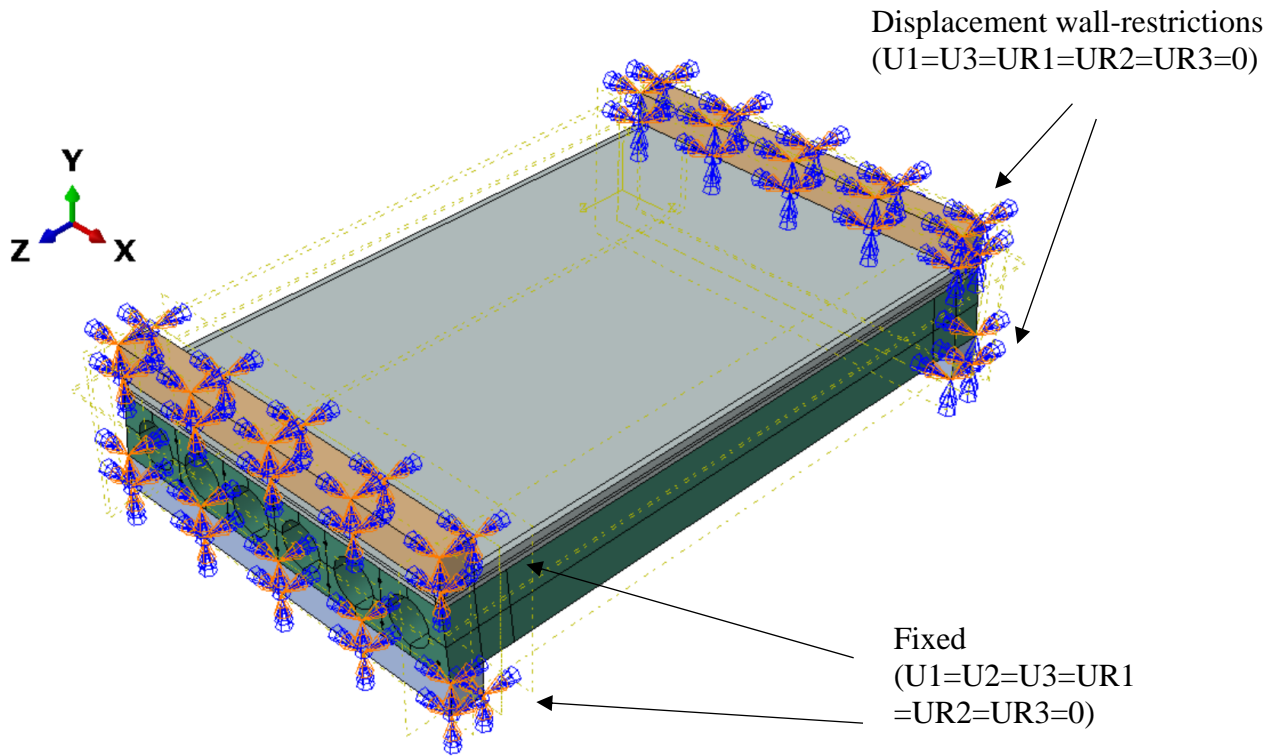


Figure 3.12. Boundary conditions at the displacement step

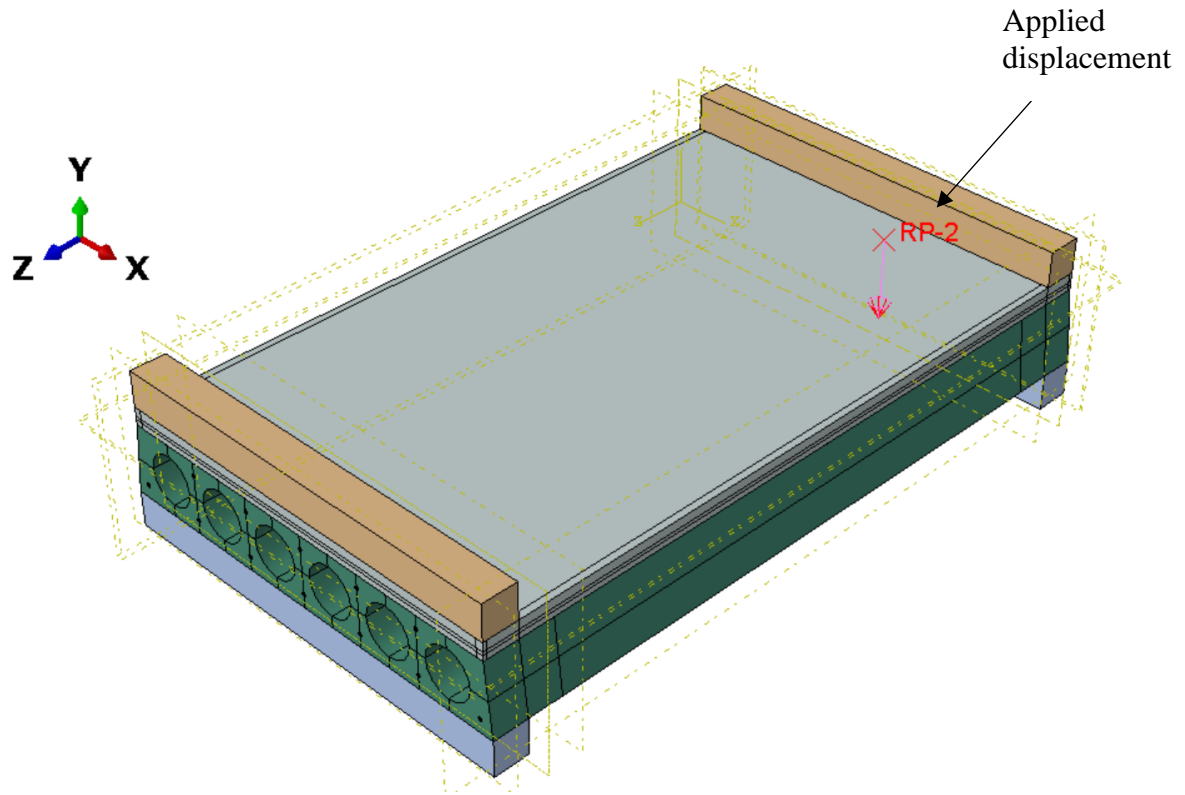


Figure 3.13. Applied displacement at a reference point

3.2.4 Material properties

Hollow-core slabs in Canada are usually made with a compressive strength of 40 MPa and with a concrete density of 2400 kg/m^3 (Coreslab Structures 2004). The specification of strands was taken from the Standard Specification for Steel Strand, Uncoated 7-wire for Prestressed Concrete from the ASTM A 416/A416M (ASTM, 2006) as per indicated in CPCI design manual 5th edition.

Constitutive Models

Constitutive models describe the material behaviour by providing stress-strain relations and the corresponding failure criteria. In this study, the Chang and Mander (1994) constitutive model was used.

Concrete (Concrete Damaged Plasticity Model)

The concrete damaged plasticity model was used in the current research work. This model uses concepts of isotropic damaged elasticity in combination with isotropic tensile and compressive plasticity to represent the inelastic behaviour of concrete. The input parameters are the uniaxial stress and plastic strain in compression and tension, damage parameters, weight factors and parameters to define the yield functions of concrete (ABAQUS (6.14)). The above-mentioned parameters are described in the following.

The concrete damaged plasticity model assumes non-associated potential plastic flow. The flow potential G used for this plasticity model by ABAQUS is the Drucker-Prager hyperbolic function:

$$G = \sqrt{(\epsilon * \sigma_{t0} * \tan\psi)^2 + q^{-2}} - p * \tan\psi \quad (3.2)$$

where,

ψ = Dilation angle

σ_{t0} = Uniaxial tensile stress at failure

ϵ = Eccentricity which defines the rate at which the function approaches the asymptote

p = Equivalent pressure stress

q = Mises equivalent stress

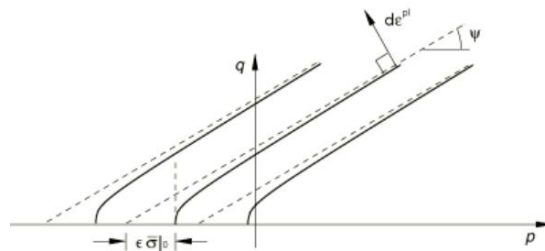


Figure 3.14 Family of hyperbolic flow potentials in the p-q plane (ABAQUS (6.14))

The concrete damaged plasticity model utilizes the yield function of Lubliner et al. (1989), with the modifications proposed by Lee and Fenves (1998) to account for different evolution of strength under tension and compression. The dilation angle, ψ describes the performance of concrete under compound stress (ABAQUS (6.14)). Even though the value of the dilation angle could be taken between 30° to 40° (Meng 2016), it is important to calibrate such a value with experimental tests. The evolution of the yield surface is controlled by the hardening variables, $\tilde{\epsilon}_c^{pl}$ and $\tilde{\epsilon}_t^{pl}$. A full expression of the yield function and its details can be found in Lee and Fenves (1998). Two of the parameters needed in the abovementioned yield function are 1) the ratio of initial equibiaxial compressive yield stress to initial uniaxial compressive yield stress (σ_{b0}/σ_{c0}) with a default value of 1.16, and 2) K_c which is the ratio of the second stress invariant on the tensile meridian, T.M., to that on the compressive meridian, C.M., at initial yield for any given value of the pressure invariant p such that the maximum principal stress is negative; condition = $0.5 < K_c \leq 1$ (Default Value = $2/3$)

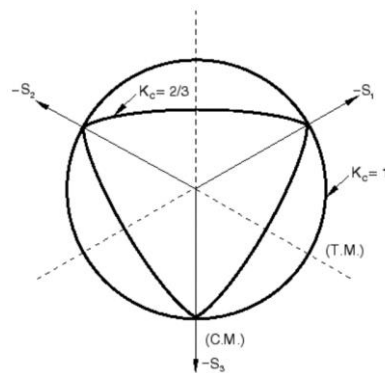


Figure 3.15 Yield surfaces in the deviatoric plane, corresponding to different values of K_c (ABAQUS (6.14)).

Materials with softening behaviour might lead to severe convergence difficulties when running an implicit analysis in ABAQUS. The viscoplastic regulation can be used to help the program converge. This technique can be applied to the concrete damaged plasticity model which allows the stresses to be outside of the yield surface (Demir et al. 2018).

Uniaxial compressive stress vs strain curve

For the stress-strain relationship, the Chang and Mander (1994) constitutive model was used. Figure 3.16 shows the response of concrete in uniaxial compression. This relationship follows a linear elastic behaviour until the value of the initial yield (σ_{c0}) of concrete is reached. After the initial yielding, a hardening stage follows, ending with the softening branch after the ultimate stress (σ_{cu} or f'_c) is reached.

In ABAQUS, the hardening data are given in terms of the inelastic strain (ε_c^{in}). This inelastic strain is defined as the total strain minus the elastic strain (ε_c^{el}) corresponding to the undamaged material. ABAQUS automatically converts these inelastic strain values to plastic strain values using the following relationship,

$$\varepsilon_c^{pl} = \varepsilon_c^{in} - \frac{d_c \sigma_c}{1-d_c E_c} \quad (3.3)$$

where,

E_c = Elastic modulus of concrete, and

d_c = Compression damage = $1 - \frac{\sigma_c}{\sigma_{cu}}$

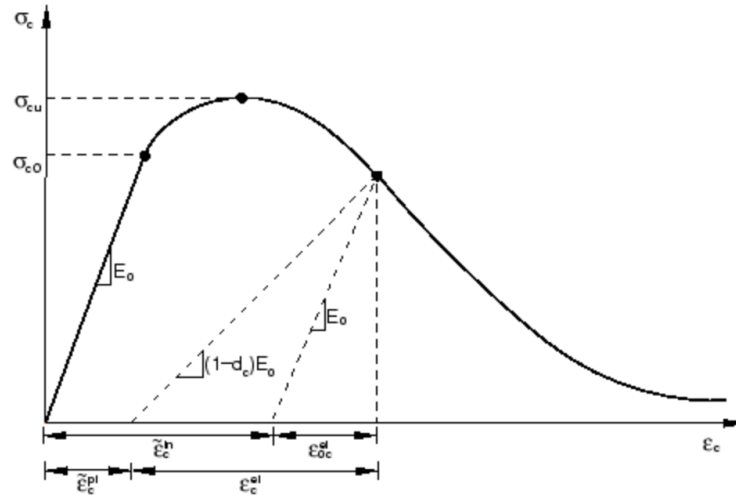


Figure 3.16 Concrete stress-strain relationship in compression, (ABAQUS (6.14)).

To obtain the compressive stress-strain relationship, the following constitutive model was used (SI Units) (Chang and Mander 1994):

$$\sigma_c = f'_c \frac{nx}{1 + \left(n - \frac{r}{r-1}\right)x + \frac{x^r}{r-1}} \quad (3.4)$$

where,

$$x = \frac{\varepsilon_c}{\varepsilon'_c} \quad (3.5), \quad n = \frac{E_c \varepsilon_c}{\sigma_{t0}} \quad (3.6) \quad \text{and} \quad r = \frac{f'_c}{5.2} - 1.9 \quad (3.7)$$

where,

f'_c = Concrete compressive strength (MPa)

ε'_c = Strain at the peak compressive stress

E_c = Modulus of Elasticity (MPa)

ε_c = Nominal compressive strain

The Modulus of Elasticity was calculated according to the Canadian Highway Bridge Design Code (CSA S6:19):

$$E_c = (3300 * \sqrt{f'_c} + 6900) * \left(\frac{\gamma_c}{2300}\right)^{1.5} \quad (3.8)$$

where the density of the concrete, γ_c , was assumed as 2500 kg/m³.

Uniaxial tensile stress vs. strain curve

This relationship follows a linear elastic behaviour until the plain concrete tension strength (σ_{t0}). The failure corresponds to the cracks in the plain concrete. After the failure stress is reached, the cracks are represented by a softening branch.

In ABAQUS, the tension stiffening data are given in terms of the cracking strain (inelastic strain). This cracking strain (ε_t^{cr}) is defined as the total strain minus the elastic strain (ε_t^{el}) corresponding to the undamaged material.

To obtain the tensile stress-strain relationship, the following constitutive model was used (SI Units) (Chang and Mander 1994).

$$\sigma_t = \sigma_{t0} \frac{nx}{1 + \left(n - \frac{r}{r-1}\right)x + \frac{x^r}{r-1}} \quad (3.9)$$

where,

$$x = \frac{\varepsilon_c}{\varepsilon_{cr}} \quad (3.10), \quad n = \frac{E_c \varepsilon_c}{\sigma_{t0}} \quad (3.11) \quad \text{and} \quad r = \frac{f'_c}{5.2} - 1.9 \quad (3.12)$$

in which,

σ_{t0} = Concrete tensile strength (MPa)

ε_{cr} = Strain at the peak tension stress

f'_c = Concrete compressive Stress (MPa)

E_c = Modulus of Elasticity (MPa)

ε_t = Nominal tensile strain

As mentioned before, the cracking strain (inelastic strain) is calculated with the following:

$$\varepsilon_t^{cr} = \varepsilon_t - \varepsilon_t^{el}, \quad (3.13)$$

$$\varepsilon_t^{el} = \frac{\sigma_t}{E_c} \quad (3.14)$$

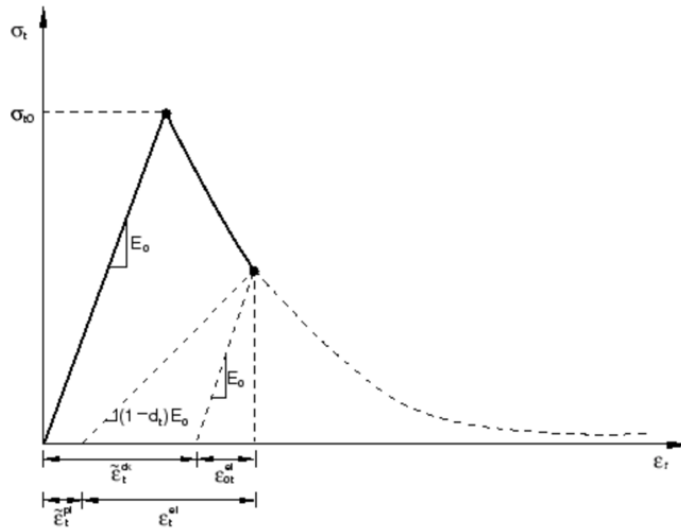


Figure 3.17 Concrete stress-strain relationship in tension, (ABAQUS (6.14)).

Strands and Reinforcement Steel

In order to capture the nonlinear behaviour of the steel, the plasticity behaviour needs to be specified when steel is modelled. When defining the plasticity data, true stress and true strain must be used so that ABAQUS interprets the data correctly, (ABAQUS (6.14)).

The relationship between true stress and nominal stress (engineering stress) as well as strains is

$$\sigma_{true} = \sigma_{nom} (1 + \varepsilon_{nom}) \quad (3.15), \quad \varepsilon_{true} = \ln (1 + \varepsilon_{nom}) \quad (3.16)$$

The plasticity model in ABAQUS defines the post-yield behaviour of metals. The plastic data define the true yield stress of the material as a function of true plastic strain. Usually, the stress-strain relationship obtained in any material test does not provide the plastic strains in the material but the total strains instead. The plastic strains can be calculated by subtracting the elastic strain from the total strain, as presented in Eq. (3.5) and shown in Figure 3.18.

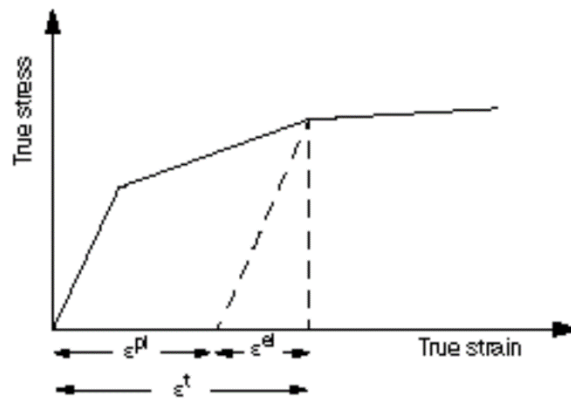


Figure 3.18. True stress-true strain relationship, (ABAQUS (6.14)).

$$\varepsilon^{pl} = \varepsilon^t - \varepsilon^{el} = \varepsilon^t - \sigma/E \quad (3.17)$$

where,

ε^{pl} = True plastic strain,

ε^t = True total strain,

ε^{el} = True elastic strain,

σ = True stress (MPa),

E = Young's modulus (MPa).

Strands Constitutive model

The constitutive model for strands was taken from the ASTM A 416/A416M (2006). The stress-strain relationship was found using the following equations.

$$\varepsilon_{ps} \leq 0.0085: f_{ps} = 28800\varepsilon_{ps} \text{ (ksi)} \quad (3.18)$$

$$\varepsilon_{ps} > 0.0085: f_{ps} = 270 - \frac{0.04}{\varepsilon_{ps} - 0.007} \text{ (ksi)} \quad (3.19)$$

*1 ksi = 6.89 MPa

Reinforcement steel Constitutive Model

The Chang and Mander (1994) constitutive model for the reinforcement steel was used to calculate the engineering stress-strain relationship. This relationship follows a linear elastic behaviour until it reaches the yield stress (σ_y) followed by the hardening branch until it reaches the ultimate stress (σ_u), as shown in Figure 3.19.

The engineering stress-strain relationship can be calculated using the following expression

$$\sigma = \frac{E(\varepsilon - \varepsilon_{shift})}{\left(1 + \left(\frac{E(\varepsilon - \varepsilon_{shift})}{\sigma_y}\right)^{10}\right)^{0.1}} + (\sigma_u - \sigma_y) \left(1 - \left|\frac{\varepsilon_u - (\varepsilon - \varepsilon_{shift})}{\varepsilon_u - \varepsilon_{sh}}\right|^p\right) \quad (3.20)$$

where

$$p = E_{sh} \frac{\varepsilon_u - \varepsilon_{sh}}{\sigma_u - \sigma_y}$$

σ = Engineering stress

σ_y = Yield Engineering stress (MPa)

σ_u = Ultimate Engineering stress (MPa)

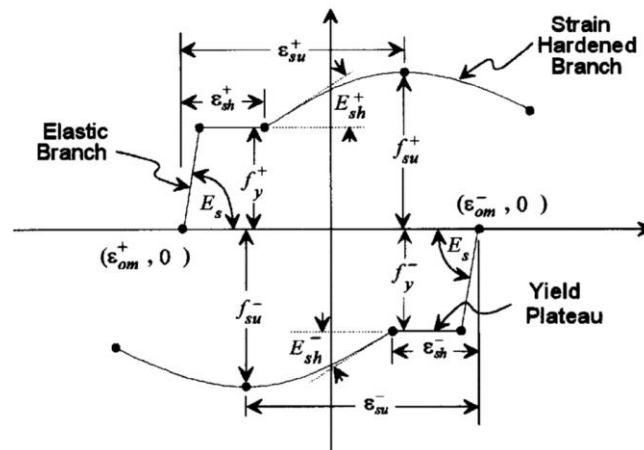
ε = Engineering strain

ε_{sh} = Yield Engineering Strain

ε_u = Ultimate engineering strain

ε_{shift} = relocated origin abscissa (Value of zero if starting at the origin)

E_{sh} = Strain hardening tangent modulus (MPa)



(a) Steel Model

Figure 3.19. Strain-Stress curve (Chang et al. 1996)

3.3 FEM Validation

This section describes the experimental test that was used to validate the developed model. It also describes the validation model and its material properties. Finally, a validation of the used concrete behaviour is presented with the calibration of the viscosity parameter.

3.3.1 Experimental test overview (Pachalla & Prakash, 2018)

The model was validated using the experimental test results by Pachalla and Prakash, (2018). The test set-up includes a full-scale hollow-core slab which was tested to evaluate the flexural and shear strengths. The slab was 150 mm deep, 1200 mm wide, and 3500 mm long (Figures 3.20 and 3.21). The slabs were prestressed with six strands of 9.53 mm diameter with an area of 54.8 mm² and a prestressing jack force of 70 kN each. Two a/d values (3.5 and 7.5) were chosen to represent the shear and flexure-dominated behaviours, where “a” represented the distance between the applied load and the middle line of the supporting beam, where “d” represented the hollow-core depth (the model was validated using only a/d=3.5 to capture potential flexure-shear interactions). A 250 kN actuator was used to apply the load. This load was transferred to a single longitudinal rigid steel spreader beam. The load was then transferred from the spreader beam to two transverse rigid steel beams located in the specific locations depending on the a/d value, as seen in Figure 3.21. Finally, the load was transferred from the two rigid steel beams to the hollow-core slab. The midspan deflection was measured using linear variable differential transformers. Also, strain gauges were mounted on the prestressed strands at the midspan to measure their strains during the test. This study also developed a finite element model of the test.

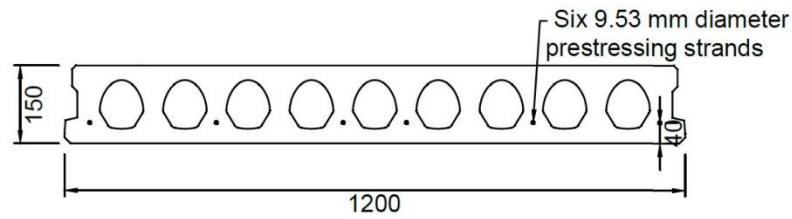


Figure 3.20. Hollow-core slab cross-section (Pachalla and Prakash, 2018).

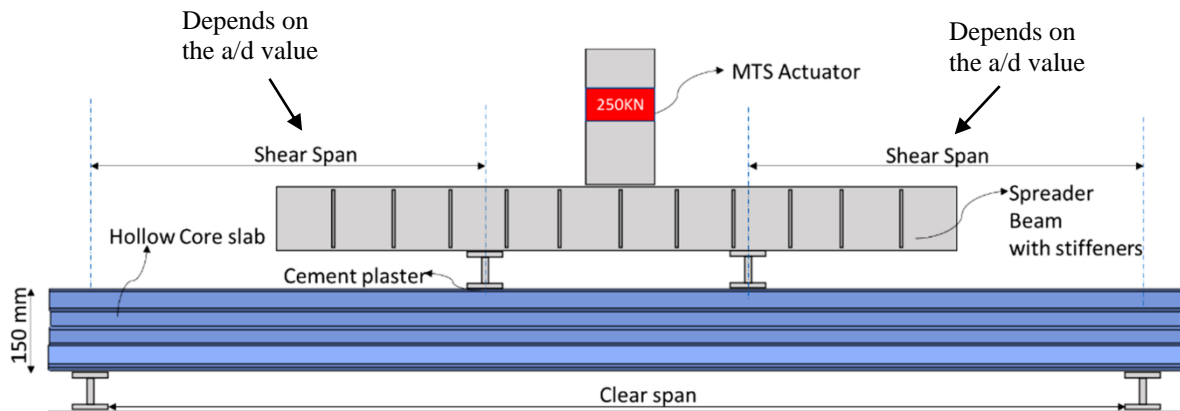


Figure 3.21. Test setup (Pachalla and Prakash, 2018)

Material properties of the experimental test (Pachalla & Prakash, 2018).

Concrete cylinders were tested and the average strength was found to be 34 MPa. The elastic modulus was estimated as 27,800 MPa and the Poisson's ratio as 0.2 as per ACI318-11. Finally, the uniaxial tensile strength of the concrete was taken as 7% of the compressive strength. The used constitutive model for concrete under compression in this paper is the Hognestad constitutive model [full details of the Hognestad constitutive model can be found in Hognestad (1951)].

Experimental test results (Pachalla & Prakash, 2018).

The specimen with $a/d = 3.5$ had a linear behaviour at the beginning of loading, an initial crack at a load of 129 kN and a second crack at the other end of the specimen at 161 kN. The slab had symmetrical cracking until a major shear crack appeared on one side. The slab had an ultimate capacity of 181 kN. The full force-displacement relationship can be seen in the following subsections.

3.3.2 Validated model

Due to the lack of dimensional details from the study by Pachalla and Prakash (2018), the following hollow-core slab was chosen in an iterative procedure with the objective to match the moment of inertia (I). This slab is 150 mm deep, 1200 mm wide, and 3500 mm long. The core voids have a diameter of 96 mm, and the prestressed strands have a 9.53 mm nominal diameter with an effective diameter of 8.3530 mm and an area of 54.8 mm^2 (Figure 3.22). Due to the small differences between the experimental slab and the validated slab, small differences can be observed in the cross-sectional geometrical comparison in Table 3.6.

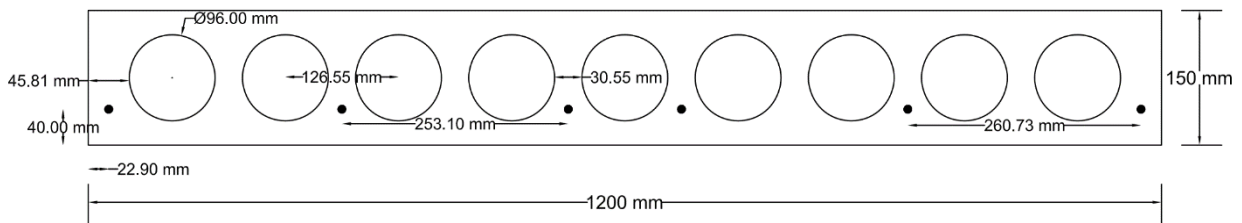


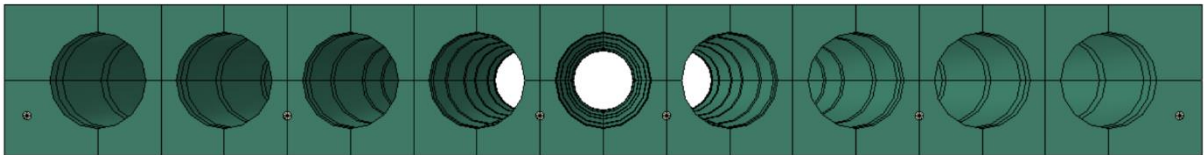
Figure 3.22. Hollow-core slab cross-section (Validation Model)

Table 3.6. Cross-sectional details comparison

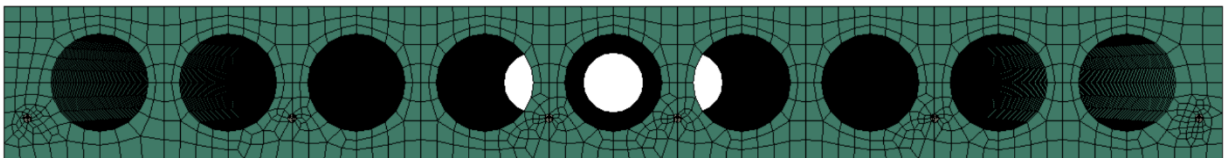
Description	Pachalla & Prakash, 2018	Validation Model
Area (mm ²)	120,370	114,527
Moment of inertia (mm ⁴)	299 x 10 ⁶	299.9 x 10 ⁶
Prestressing reinforcement ratio % (A_p/A_c)	0.273	0.287

The boundary conditions and the loading were applied following the same set-up described in the experimental test overview (Section 3.3.1). The slab had a pin-roll support and the loading was applied to a location where the a/d ratio was 3.5 (525 mm from the support at both sides). The hollow-core slab and the prestressed strands were built with brick elements (3D), as shown in Figures 3.23 and 3.24. The load was applied to an area to simulate the two transverse steel rigid beams, as shown in Figure 3.24. Also, an interaction was created for each strand to simulate the proper interaction between the prestressed strand and the concrete.

a)



b)



c)

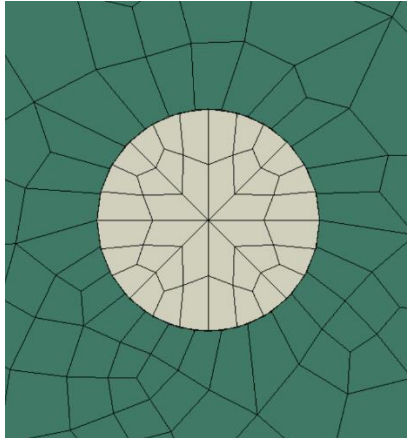


Figure 3.23. a) Partition of the hollow-core slab. b) Meshing of the hollow-core slab. c) Zoom of the strand's meshing.

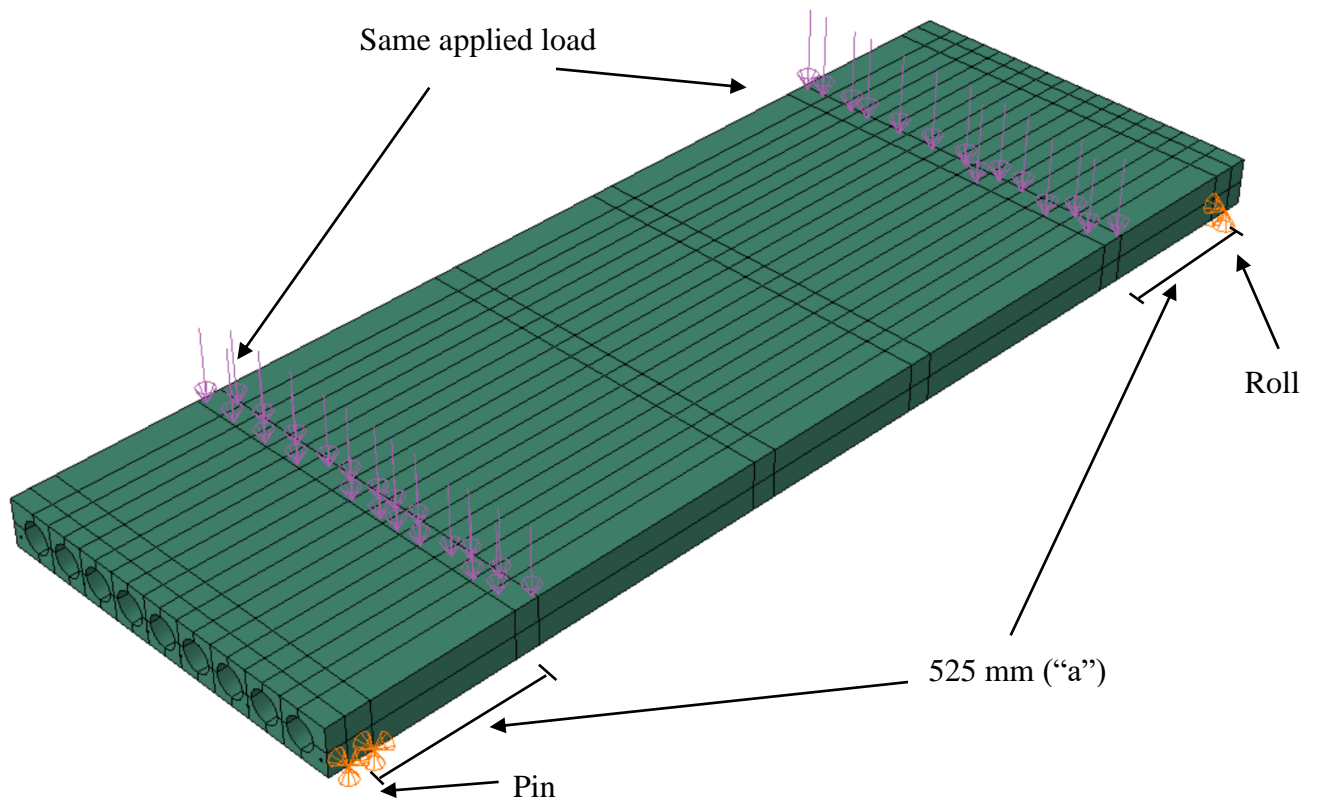


Figure 3.24. Boundary conditions and loading in the validated model.

*Note: The loading and the boundary conditions (pin) are symmetrical on each end of the slab. The lack of symmetry in Figure 3.24 is due to the lack of resolution in the ABAQUS interface.

Material properties (validated model)

The material properties were chosen according to the experimental study, as mentioned in Section 3.3.1. The constitutive models that were applied to this validation are the same models described in Section 3.2.4. Using the Chang and Mander (1994) constitutive model for the compressive and tensile concrete behaviour and the ASTM A 416/A416M (2006) for the strand behaviour, the stress-strain relationships are shown in Figures 3.25 to 3.27. A summary of the material properties and the ABAQUS input for concrete can be found in Tables 3.7 and 3.8, while a summary of the material properties and the ABAQUS input for the strand can be found in Table 3.9.

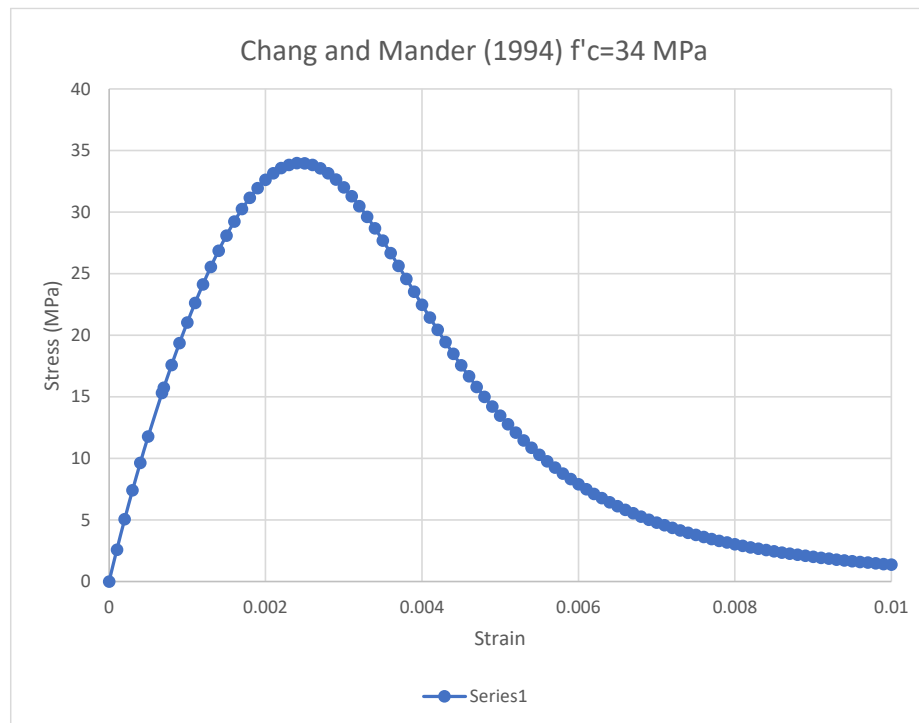


Figure 3.25. Compressive stress-strain relationship $f'_c=34$ MPa (Chang and Mander 1994)

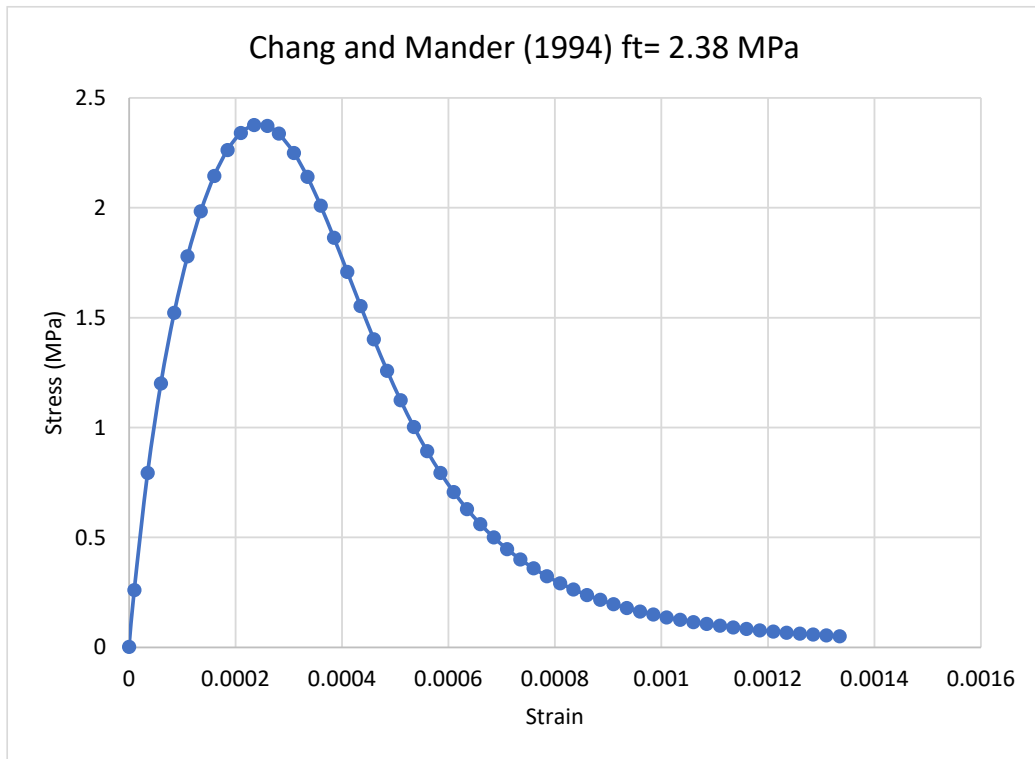


Figure 3.26. Tensile stress-strain relationship $f_t=2.38$ MPa (Chang and Mander 1994)

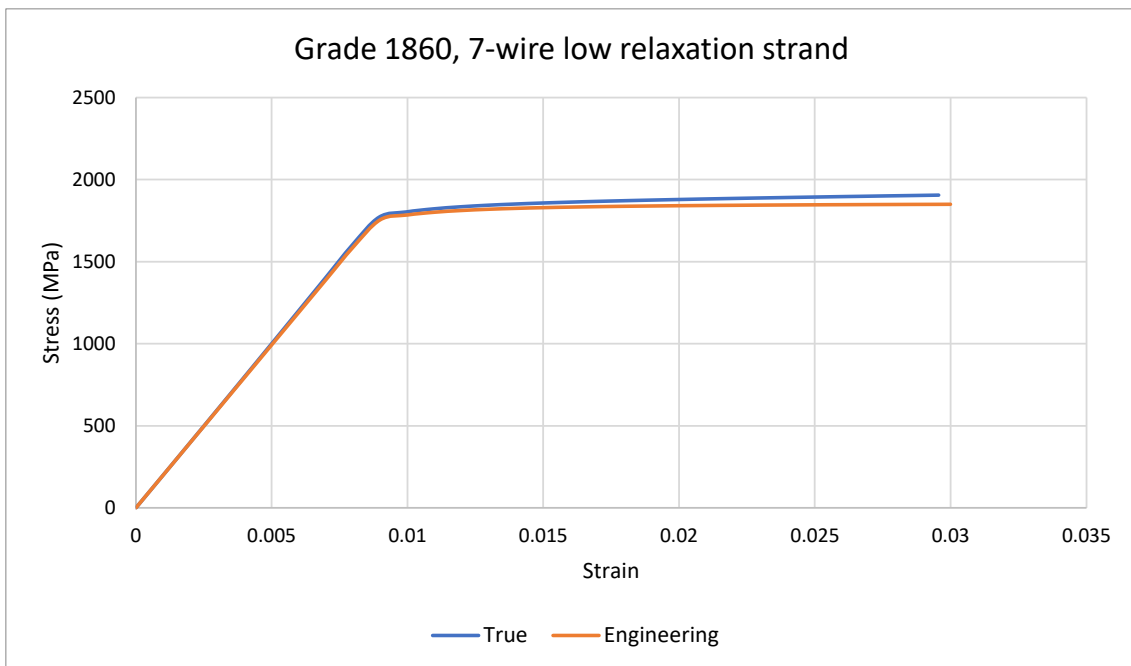


Figure 3.27. Strand stress-strain relationship for a Grade 1860, 7-wire low relaxation strand.

Table 3.7 Material Properties and ABAQUS input for the Hollow-core slab (Concrete)

Material Parameters		Plasticity Parameters	
		Dilation angle**	30
f'c*	34	Eccentricity**	0.1
E (MPa)*	27800	Fb0/fc0**	1.16
Poisson ratio*	0.2	K**	0.67
		Viscosity parameter	0.0002
Concrete compressive behaviour		Concrete Tensile behaviour	
Yield Stress (MPa)	Inelastic Strain	Yield Stress (MPa)	Cracking Strain
11.78	0.000000	2.38	0
15.75	0.000133	2.37	0.0001747
19.36	0.000203	2.34	0.0001972
22.63	0.000286	2.25	0.0002291
25.55	0.000381	2.14	0.000258
28.11	0.000489	2.01	0.0002877
30.26	0.000611	1.86	0.000318
31.96	0.000750	1.71	0.0003485
33.18	0.000907	1.55	0.0003791
33.85	0.001082	1.40	0.0004096
33.98	0.001278	1.26	0.0004397
33.57	0.001493	1.12	0.0004695
32.65	0.001725	1.00	0.0004989
31.31	0.001974	0.89	0.0005279
29.62	0.002234	0.79	0.0005564
27.70	0.002504	0.71	0.0005846
24.59	0.002915	0.63	0.0006124
22.49	0.003191	0.56	0.0006398
20.44	0.003465	0.50	0.000667
18.50	0.003735	0.45	0.0006939
16.68	0.004000	0.40	0.0007206
15.01	0.004260	0.36	0.0007471
13.48	0.004515	0.32	0.0007734
12.11	0.004764	0.29	0.0007995
10.31	0.005129	0.26	0.0008255
9.26	0.005367	0.24	0.0008514
8.34	0.005600	0.22	0.0008772
7.51	0.005830	0.20	0.0009029
6.78	0.006056	0.18	0.0009286
6.13	0.006280	0.16	0.0009541
5.55	0.006500	0.15	0.0009796
5.03	0.006719	0.14	0.0010051

*From: Pachalla and Prakash, 2018

**From: Yapar et al, 2015

Table 3.8 Stress-strain relationship data for concrete $f'_c=34$ MPa and $f_t=2.38$ MPa.

Concrete compressive behaviour		Concrete Tensile behaviour	
Stress (MPa)	Strain	Stress (MPa)	Strain
2.60	0.0001	0.26	0.00001
7.42	0.0003	0.79	0.000035
11.78	0.0005	1.20	0.00006
15.75	0.0007	1.52	0.000085
19.36	0.0009	1.78	0.00011
22.63	0.0011	1.98	0.000135
25.55	0.0013	2.15	0.00016
28.11	0.0015	2.26	0.000185
30.26	0.0017	2.34	0.00021
31.96	0.0019	2.38	0.000235
33.17	0.0021	2.37	0.00026
33.85	0.0023	2.34	0.0002813
33.98	0.0025	2.25	0.00031
33.57	0.0027	2.14	0.000335
32.65	0.0029	2.01	0.00036
31.31	0.0031	1.86	0.000385
29.62	0.0033	1.71	0.00041
27.70	0.0035	1.55	0.000435
25.64	0.0037	1.40	0.00046
23.54	0.0039	1.26	0.000485
21.46	0.0041	1.13	0.00051
19.45	0.0043	1.00	0.000535
17.57	0.0045	0.89	0.00056
15.82	0.0047	0.79	0.000585
14.23	0.0049	0.71	0.00061
12.78	0.0051	0.63	0.000635
11.47	0.0053	0.56	0.00066
10.31	0.0055	0.50	0.000685
9.26	0.0057	0.45	0.00071
8.34	0.0059	0.40	0.000735
7.51	0.0061	0.36	0.00076
6.78	0.0063	0.32	0.000785
6.13	0.0065	0.29	0.00081
5.55	0.0067	0.26	0.000835
5.03	0.0069	0.24	0.00086
4.57	0.0071	0.22	0.000885
4.17	0.0073	0.20	0.00091
3.80	0.0075	0.18	0.000935
3.47	0.0077	0.16	0.00096
3.18	0.0079	0.15	0.000985
2.91	0.0081	0.14	0.00101
2.68	0.0083	0.13	0.001035
2.46	0.0085	0.12	0.00106
2.27	0.0087	0.11	0.001085
2.10	0.0089	0.10	0.00111

Table 3.9 Material properties and ABAQUS input for the prestressing strands.

Material Parameters			
Grade **	1860	Type of Strand *	Low-relaxation
E (MPa) *	197000	Diameter of the strand *	12.7 (mm)
Poisson ratio*	0.3	Steel Area *	98.7 (mm ²)
Strand behaviour		Strand plastic behaviour (Input ABAQUS)	
True Stress (Mpa)	True Strain	True Yield Stress (MPa)	True Plastic Strain
198.77	0.001	198.77	0
397.93	0.002	397.93	0
597.49	0.003	597.49	0
797.45	0.004	797.45	0
997.81	0.005	997.81	0
1198.56	0.006	1198.56	0
1399.71	0.007	1399.71	0
1601.26	0.008	1601.26	0
1771.31	0.009	1771.31	0
1802.83	0.010	1802.83	0.000799
1821.45	0.011	1821.45	0.001694
1834.08	0.012	1834.08	0.002618
1843.46	0.013	1843.46	0.003559
1850.85	0.014	1850.85	0.004508
1856.96	0.015	1856.96	0.005462
1862.18	0.016	1862.18	0.006421
1866.77	0.017	1866.77	0.007381
1870.89	0.018	1870.89	0.008343
1874.65	0.019	1874.65	0.009306
1878.13	0.020	1878.13	0.010269
1881.39	0.021	1881.39	0.011232
1884.47	0.022	1884.47	0.012196
1887.41	0.023	1887.41	0.013159
1890.22	0.024	1890.22	0.014122
1892.93	0.025	1892.93	0.015084
1895.55	0.026	1895.55	0.016046
1898.10	0.027	1898.10	0.017007
1900.58	0.028	1900.58	0.017968
1903.01	0.029	1903.01	0.018927
1905.40	0.030	1905.40	0.019887
1907.74	0.031	1907.74	0.020845
1910.04	0.031	1910.04	0.021803
1912.31	0.032	1912.31	0.022760
1914.55	0.033	1914.55	0.023716
1916.76	0.034	1916.76	0.024672

*From: ASTM,
2006.

**From:
Pachalla and
Prakash, 2018

Concrete material validation

The concrete material in the model used the concrete damaged plasticity model, which is described in section 3.2.4. The stress-strain relationship was determined using the Chang and Mander (1994) constitutive model and they can be seen in the previous section. The concrete response was validated with ABAQUS explicit (even though implicit analysis was used for the analyses in this thesis) due to its capability of capturing the post-failure response of the model, thus obtaining a more accurate softening branch. A cylindrical specimen was modelled and compared with the stress-strain relationship. The cylinder has a 150 mm diameter and a height of 300 mm. The bottom face was fixed, while the upper face had a displacement of 6 mm and was restrained in all other directions. Gravity load was also applied, as shown in Figure 3.28.

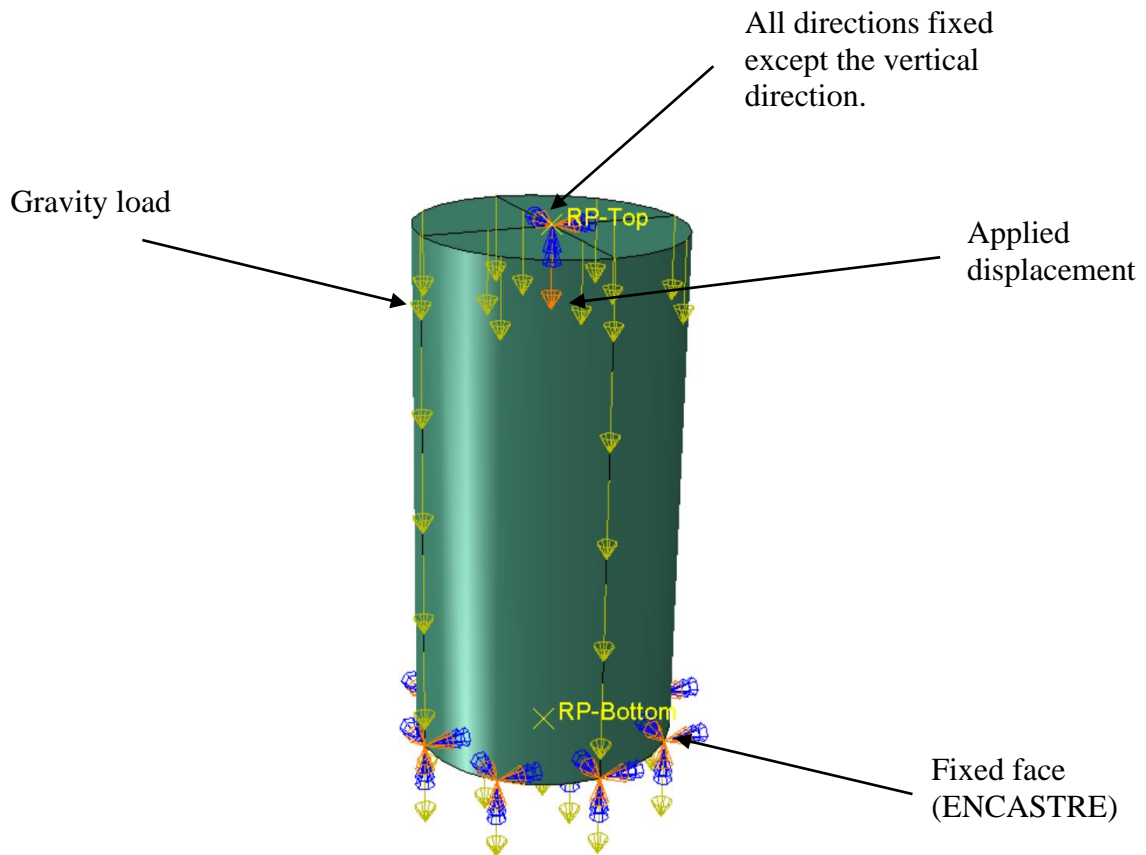


Figure 3.28. Cylinder with boundary and loading conditions

The model behaviour is similar to the Chang and Mander (1994) constitutive model, as shown in Figure 3.29. The ABAQUS computation had a difference in the peak compressive strength of 1.46 %, while a maximum difference of 33.7% at a strain of 0.004 on the descending branch was found. While this constitutive model only requires a direct stress-strain relationship, the concrete damage plasticity model in ABAQUS requires several variables (e.g., dilation angle, eccentricity, etc.) and the yield stress-inelastic strain relationship in addition to a meshing which can only make an approximation of the geometry. For these reasons, the constitutive model and the numerical model do not completely match.

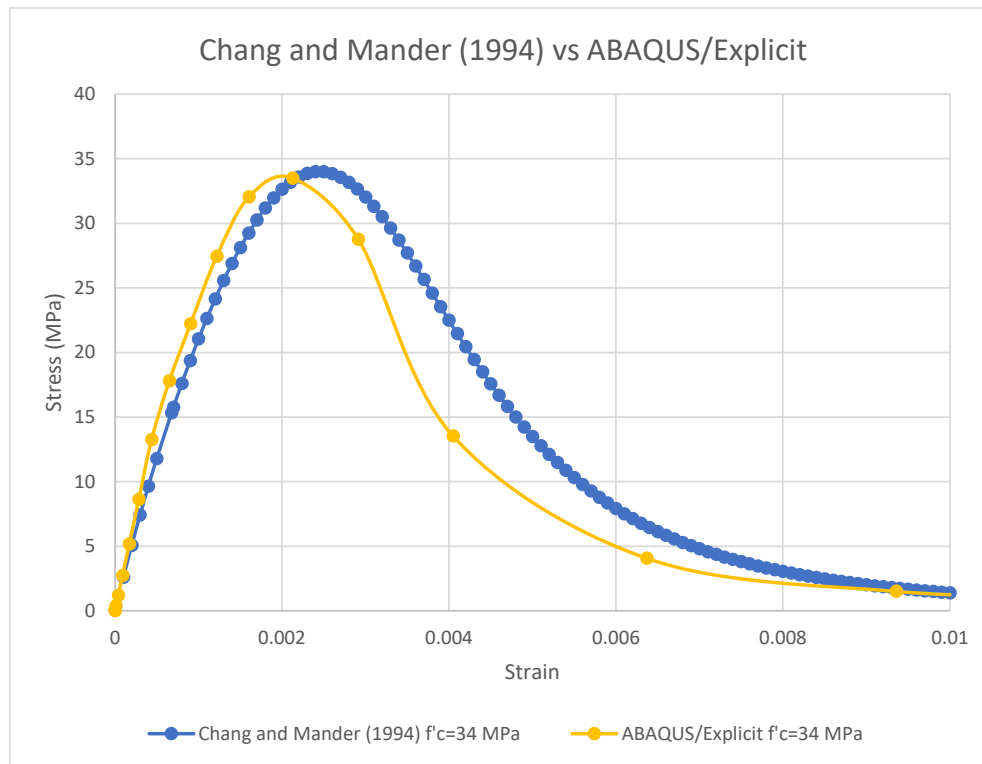


Figure 3.29 Comparison between Chang and Mander (1994) constitutive model vs ABAQUS explicit cylinder test, $f'_c=34$.

Overall model validation

The comparisons between the experimental and model results can be seen in Figures 3.30 and 3.31. The small differences between the experimental test or the FE model from the literature and the model developed herein using ABAQUS might be attributed to small differences in the cross-section geometry, the concrete behaviour and the interaction between the strand and the concrete. The comparison of the camber displacement due to the prestress at the end of the “prestressing step” is shown in Figures 3.30 and 3.31. The maximum difference between such displacements is 3%. The main difference between these two models is the type of element that is being used to model the prestressing strands. Specifically, this validation model built the prestressing strands using brick elements (3D), while Pachalla & Prakash (2018) built the strands with truss elements (2D). In the validation model, the Hoyer Effect can be seen at the end of the slab (bottom of the slab) which cannot be seen in Figure 3.31 since truss 2D elements cannot capture this effect.

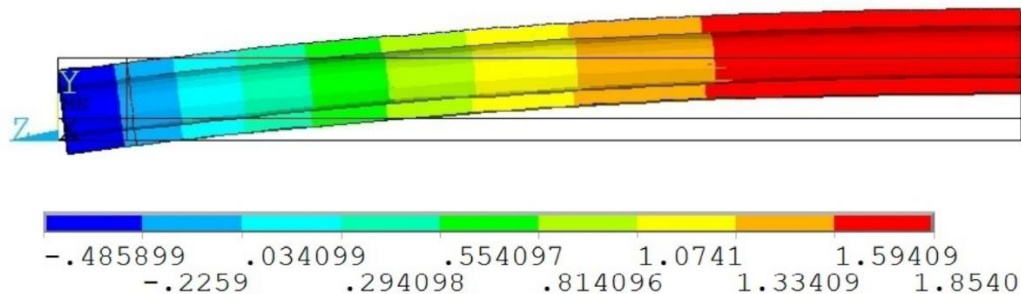


Figure 3.30 Camber displacement (mm) due to prestress (Pachalla and Prakash, 2018)

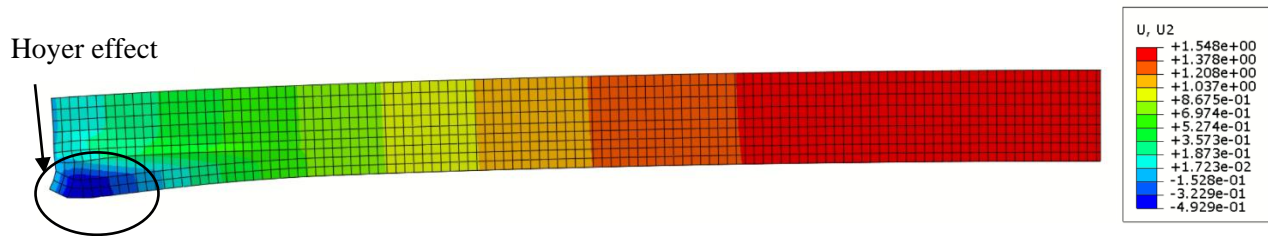


Figure 3.31 Camber displacement (mm) due to prestress (Validation Model)

The load-displacement relationship comparison is shown in Figure 3.32 until the peak load. The model remained almost elastic until a load of 100 kN and then started to have a nonlinear behaviour. This model had a peak load of 185 kN which has a difference of 2.2% relative to the experimental test. It was not of interest to capture the post-peak response during validation because the specimens in this thesis are investigated within the pre-peak response once cracks are initiated. Once the model showed a yielding area in the same pattern as the cracks in the experimental test (at the peak load stage), it had trouble converging (suggesting failure), and the model was terminated at that point.

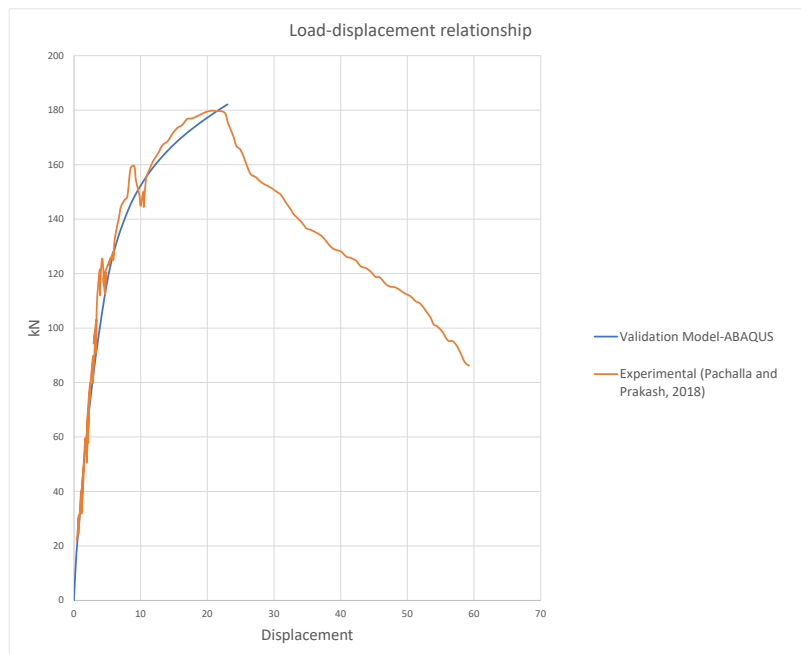


Figure 3.32. Load-displacement relationship comparison

Figure 3.33 compares the longitudinal stresses on the bottom of the slab due to the prestress between the theoretical values and the validation model at the end of the prestress step. The theoretical values were calculated using the Canadian Highway Bridge Design Code (CSA Group (1). (2019)). The maximum error is 15% with a difference of 0.7 MPa at a distance of 344 mm from the end of the slab.

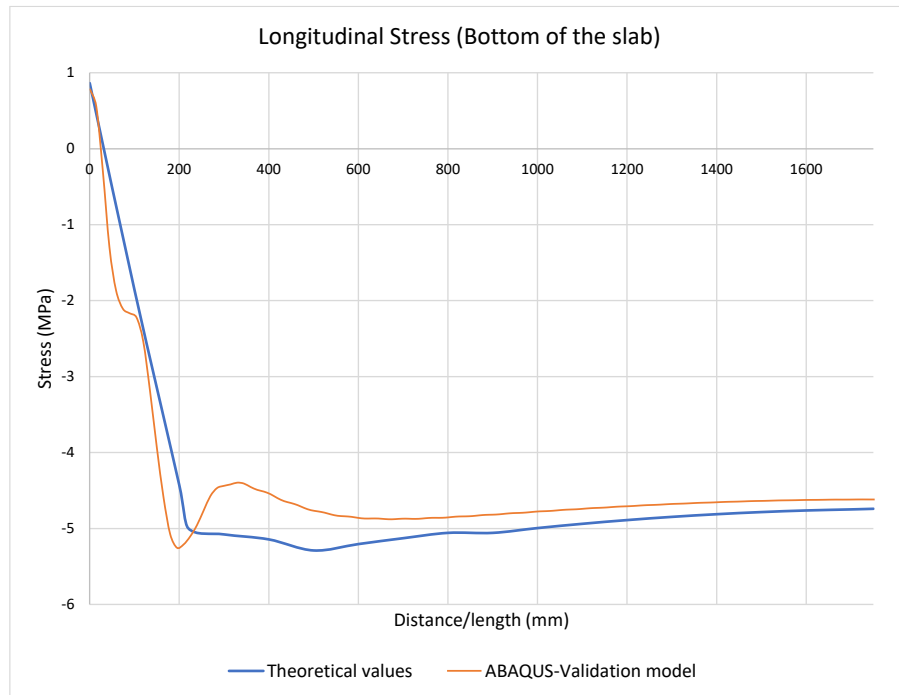


Figure 3.33. Longitudinal stresses at the bottom of the slab at the end of the prestress step (Theoretical values vs Validation model)

Viscosity parameter

Implicit analysis models such as the Concrete Damage Plasticity model (described in Section 3.2.4) can lead to convergence difficulties due to the softening behaviour and stiffness degradation (Demir, 2018). This model can be regularized by using the viscosity parameter (μ) when defining the material properties of the concrete. This parameter permits stresses to be outside of the yield

surface, ABAQUS (6.14). No suggested value for the viscosity parameter was found in the ABAQUS manual. Several different values were found in the literature when modelling a prestressed concrete element including 0.001 (Yapar et al. 2015) and 0.0005 (Meng, 2016; Demir, 2018). Four values for the viscosity parameter were compared in order to choose the most accurate parameter for the model: $\mu=0.0001$, 0.0002, 0.0003 and 0.0005. After the numerical investigation, the value of 0.0002 was considered to be the most accurate based on the available experimental results. The sensitivity of the model to different viscosity parameter values is shown in Figure 3.34.

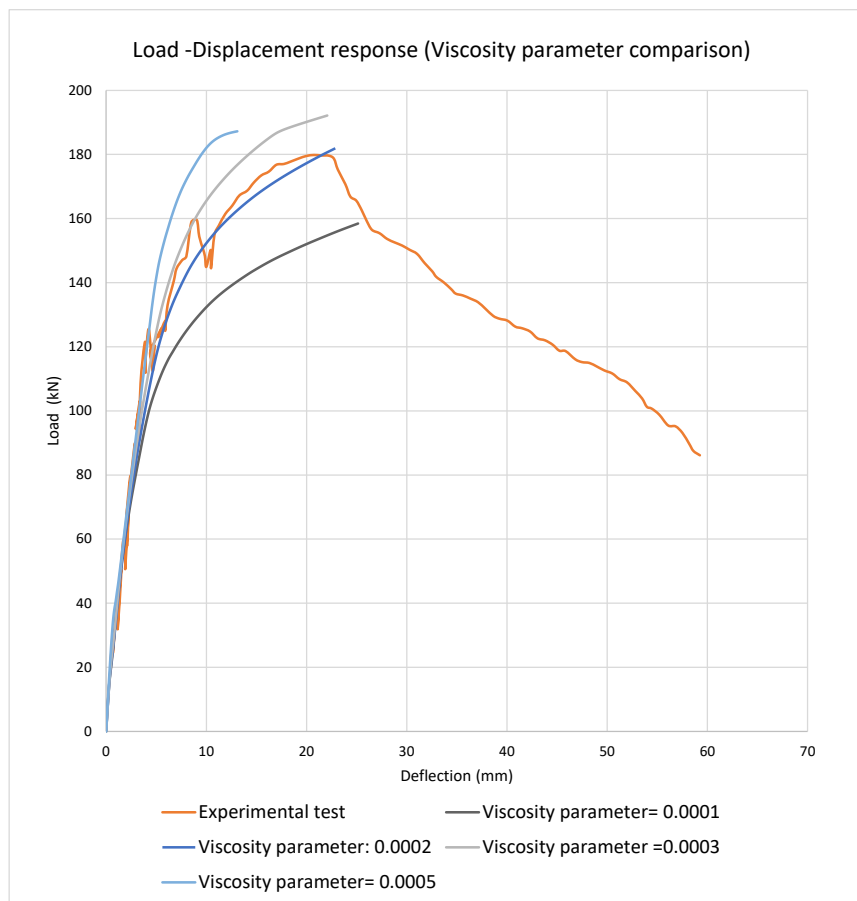


Figure 3.34 Load-Displacement response (Viscosity parameter comparison).

Chapter 4: Parametric Study

This parametric study investigates the behaviour of hollow-core slabs when subjected to a vertical displacement incompatibility, as described in Section 2.3. This investigation consists of using the FEM described in Chapter 3 with different variables including cross-section areas, configurations of prestressing and span lengths with the objective of capturing their modes of failure and displacement capacities. A total of 24 models are analyzed, as listed in Section 4.2.

This chapter describes the model parameters, the material properties of the models, and the results of the analysis. Section 4.1 gives an overview of the parametric study. Details of the model geometries and amounts of prestressing are organized in Section 4.2. Section 4.3 describes the material properties of the hollow-core slabs, prestress strands, topping and rebar. Subsection 4.4.1 presents one specimen that serves as a reference for understanding the behaviour of the complete set of models. Subsections 4.4.2 to 4.4.5 present the full results by comparing the effects that the different variables have on the slab. Subsection 4.4.6 details results for outlier cases. Finally, Subsection 4.4.7 presents tables of results for the 24 models.

4.1. Overview

This chapter presents the parametric study which captures the behaviour of a prestressed hollow-core slab under a displacement incompatibility with fixed ends (i.e., downward relative vertical displacement at one end). This parametric study consists of comparing the displacement capacities of hollow-core slabs with different parameters, including the span length, the amount of prestressing and the cross-section area. The results are categorized into five different damage stages: initial damage (also referred to as 0% damage), 10% damage (where 10% refers to the

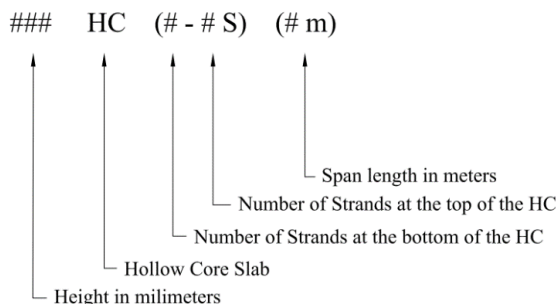
depth of the slab that has reached the damage criterion), 20% damage, 30% damage, and failure of the slab. The damage criterion of the concrete can be seen in ABAQUS as either plastic strain or elastic strain (ABAQUS outputs) at the peak of the curve in the tensile stress-strain relationship of the concrete, which is presented in Subsection 4.3.1. The damage criterion is observed in ABAQUS by setting a “max” limit to the selected strain. Both strains have one to one correspondance to each other when transformed from one to the other with equations (3.3, 3.13 and 3.14).

4.2 Hollow-core geometries and nomenclature

The chosen hollow-core cross-sections are taken from the load table specification details that are used in Ontario, Canada (Coreslab Structures, 2009). The following parameters were chosen for this study:

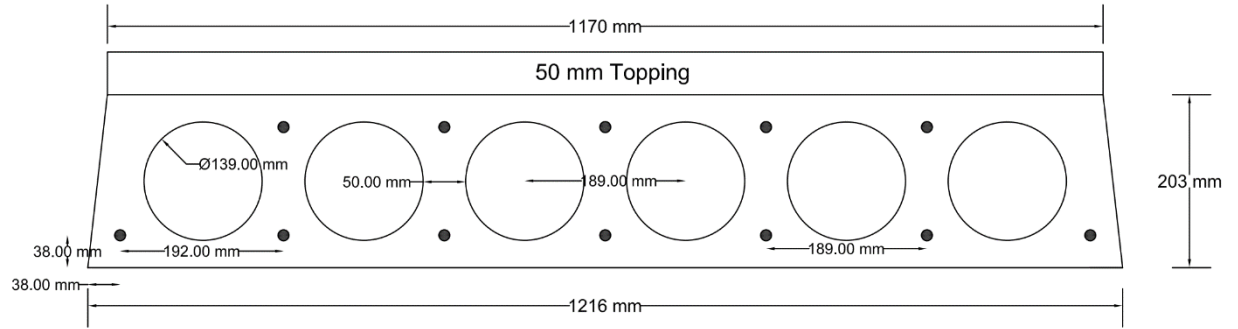
- Depths: 203, 254, 304 and 355 (all in mm)
- Prestress configurations: prestress at the bottom and prestress at both bottom and top
- Span lengths: 2, 5 and 8 (all in m)

The span lengths were chosen based on the typical layouts of masonry buildings (e.g., hallways and small and large rooms). The detailing of the cross-section geometries is presented in Section 4.2.1 with Table 4.1 which summarizes all the considered models. The nomenclature of the models is as follows:

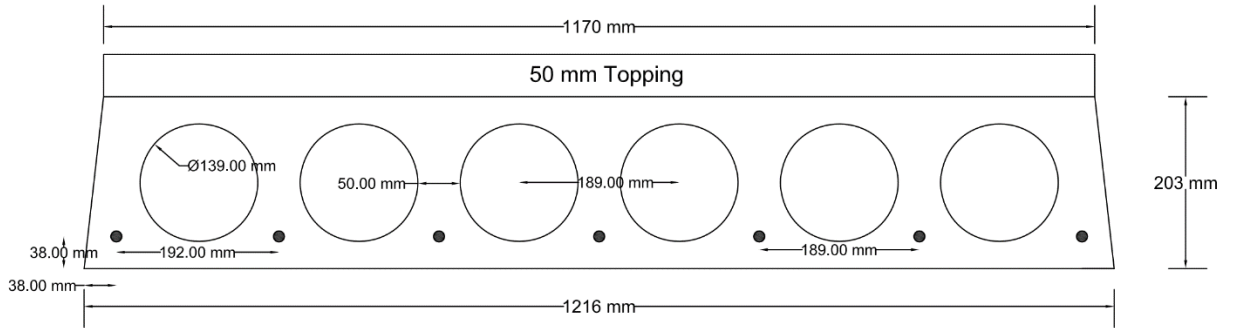


4.2.1 Hollow-core Geometries:

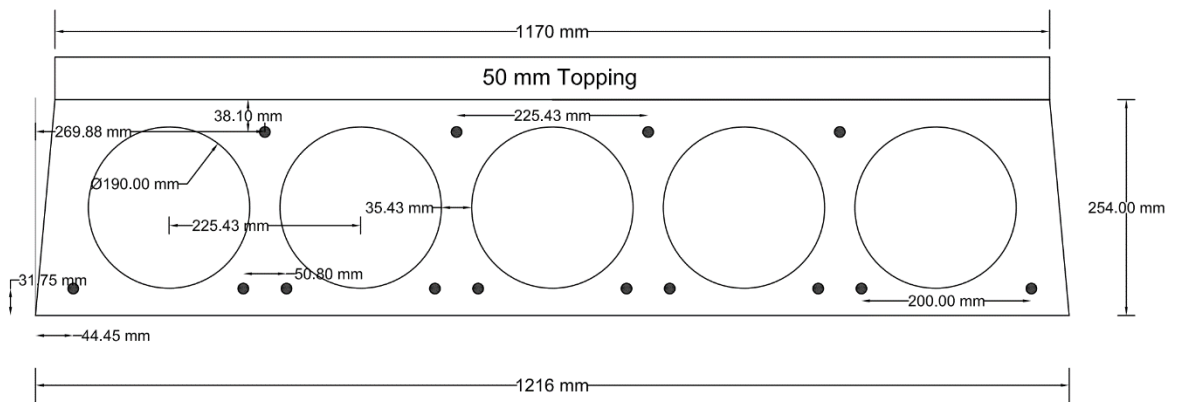
203HC (7-5 S)



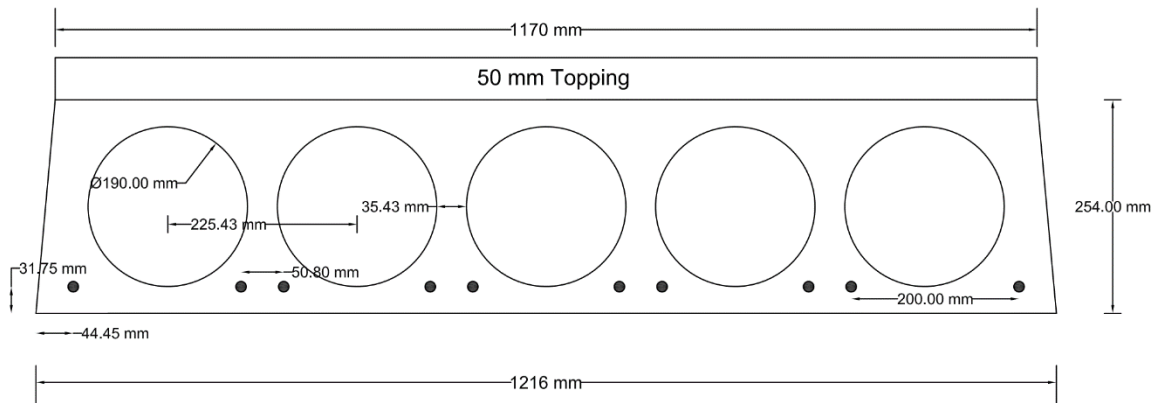
203HC (7-0 S)



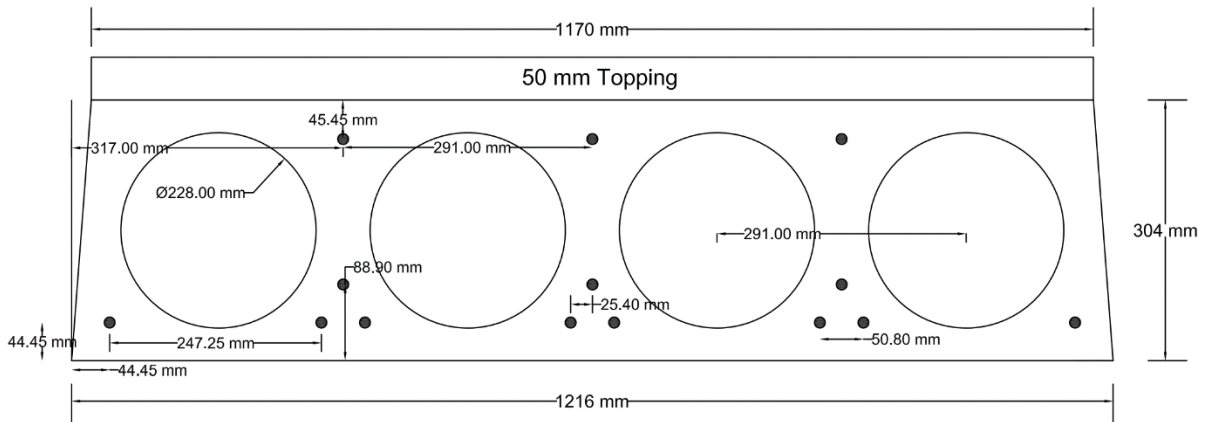
254HC (10-4 S)



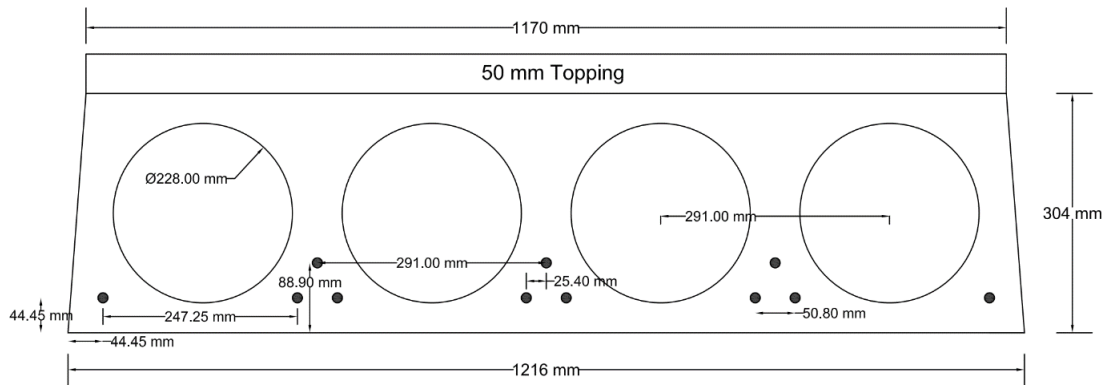
254HC (10-0 S)



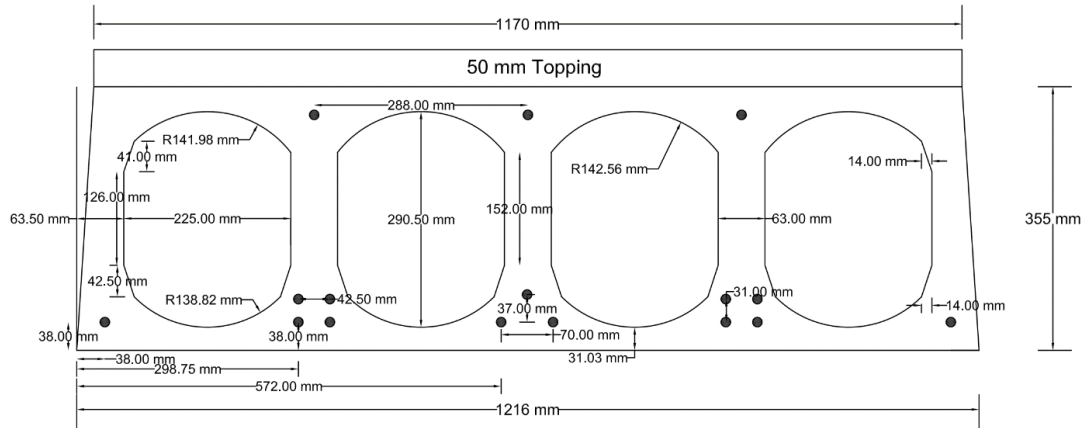
304HC (11-3 S)



304HC (11-0 S)



355HC (13-3 S)



355HC (13-0 S)

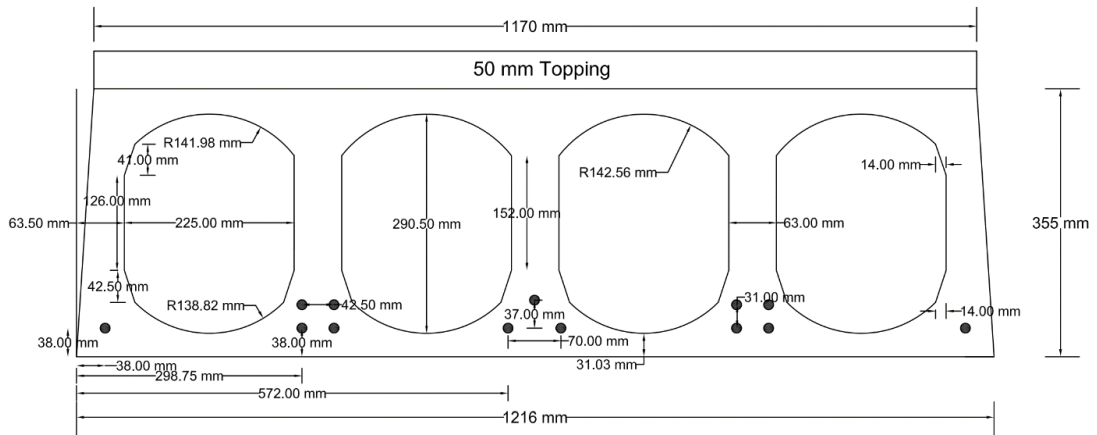


Figure 4.1. Hollow-core cross-sections. All geometries were obtained from Coreslab Structures (2009).

Table 4.1. List of Models in Parametric Study

Specimen Name	Height (mm)	# of strands at the bottom	# of strands at the top	Span length (m)
203HC(7-0 S)-2	203	7	0	2
203HC(7-0 S)-5	203	7	0	5
203HC(7-0 S)-8	203	7	0	8
203HC(7-5 S)-2	203	7	5	2
203HC(7-5 S)-5	203	7	5	5
203HC(7-5 S)-8	203	7	5	8
254HC(10-0 S)-2	254	10	0	2
254HC(10-0 S)-5	254	10	0	5
254HC(10-0 S)-8	254	10	0	8
254HC(10-4 S)-2	254	10	4	2
254HC(10-4 S)-5	254	10	4	5
254HC(10-4 S)-8	254	10	4	8
304HC(11-0 S)-2	304	11	0	2
304HC(11-0 S)-5	304	11	0	5
304HC(11-0 S)-8	304	11	0	8
304HC(11-3 S)-2	304	11	3	2
304HC(11-3 S)-5	304	11	3	5
304HC(11-3 S)-8	304	11	3	8
355HC(13-0 S)-2	355	13	0	2
355HC(13-0 S)-5	355	13	0	5
355HC(13-0 S)-8	355	13	0	8
355HC(13-3 S)-2	355	13	3	2
355HC(13-3 S)-5	355	13	3	5
355HC(13-3 S)-8	355	13	3	8

4.3 Material properties

The constitutive models used for this parametric study are identical to those presented in Chapter 3 during model validation. For the concrete behaviour, the model by Chang and Mander (1994) is used, while the ASTM A 416/A416M (2006) is used for the strand's behaviour, as described in Chapter 3. In the following sections, tables are provided to summarize the material properties, ABAQUS input (yielding stress – inelastic strain relationship), and the stress-strain relationship of each material.

4.3.1. Concrete

The concrete compressive strength f'_c is taken as 40 MPa and the tensile strength of the concrete as 4 MPa (10% of the compressive strength) (Lin et al. 2003). The assumed compressive and tensile stress-strain relationships are shown in Figure 4.2 and Figure 4.3, respectively. Table 4.2 presents the elastic compressive and tensile behaviour, while Table 4.3 shows the input data used in the ABAQUS model including the plasticity parameters, the inelastic compressive and tensile behaviour and a summary of the material properties. As mentioned before, the damage criterion is defined as a specific strain (plastic or elastic strain) at the peak of the curve in the tensile stress-strain relationship of the concrete with values of 0.00013 and 0.00026, respectively (see Figure 4.3 and Table 4.3). Since both strains have one to one correspondance, they are used to illustrate the damage in the concrete for clarity purposes. The plastic strain is calculated with equation 3.3 from Chapter 3 and the elastic strain is found in the tensile stress-strain relationship.

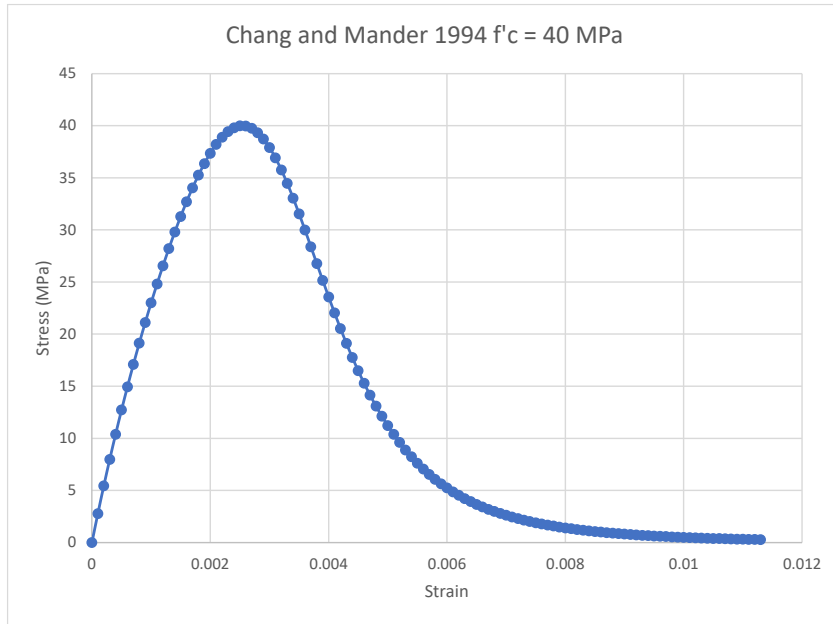


Figure 4.2. Compressive stress-strain relationship $f'_c=40$ MPa (Chang and Mander 1994)

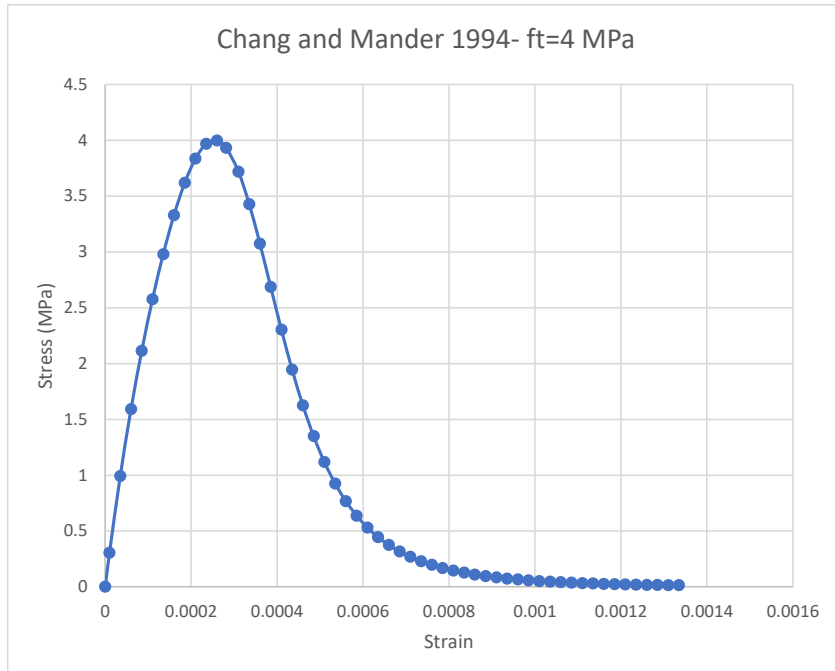


Figure 4.3. Tensile stress-strain relationship $f_t=4$ MPa (Chang and Mander 1994)

Table 4.2. Stress-strain relationship data for concrete $f'_c=40$ MPa and $f_t=4$ MPa.

Concrete compressive behaviour		Concrete Tensile behaviour	
Stress (MPa)	Strain	Stress (MPa)	Strain
2.78	0.0001	0.31	0.00001
7.96	0.0003	0.99	0.000035
12.71	0.0005	1.59	0.00006
17.08	0.0007	2.11	0.000085
21.10	0.0009	2.58	0.00011
24.80	0.0011	2.98	0.000135
28.20	0.0013	3.33	0.00016
31.29	0.0015	3.62	0.000185
34.03	0.0017	3.84	0.00021
36.36	0.0019	3.97	0.000235
38.19	0.0021	4.00	0.00026
39.44	0.0023	3.93	0.0002813
39.98	0.0025	3.72	0.00031
39.75	0.0027	3.43	0.000335
38.71	0.0029	3.07	0.00036
36.90	0.0031	2.69	0.000385
34.46	0.0033	2.30	0.00041
31.55	0.0035	1.94	0.000435
28.38	0.0037	1.62	0.00046
25.15	0.0039	1.35	0.000485
22.02	0.0041	1.12	0.00051
19.11	0.0043	0.92	0.000535
16.47	0.0045	0.77	0.00056
14.14	0.0047	0.64	0.000585
12.11	0.0049	0.53	0.00061
10.37	0.0051	0.45	0.000635
8.88	0.0053	0.37	0.00066
7.61	0.0055	0.32	0.000685
6.54	0.0057	0.27	0.00071
5.63	0.0059	0.23	0.000735
4.86	0.0061	0.20	0.00076
4.21	0.0063	0.17	0.000785
3.66	0.0065	0.15	0.00081
3.18	0.0067	0.13	0.000835
2.78	0.0069	0.11	0.00086
2.44	0.0071	0.10	0.000885
2.14	0.0073	0.08	0.00091

Table. 4.3 Material properties and ABAQUS input for the hollow-core slab and the topping (concrete)

Material Parameters		Plasticity Parameters	
		Dilation angle	30
f'c	40	Eccentricity	0.1
E (MPa)	31471	K	1.16
Poisson ratio	0.2	Viscosity parameter	0.0002
Concrete compressive behaviour		Concrete Tensile behaviour	
Yield Stress (MPa)	Inelastic Strain	Yield Stress (MPa)	Cracking Strain
12.71	0.00013	3.99	0
17.08	0.00033	4.00	0.00013
21.10	0.00053	3.93	0.00016
24.80	0.00073	3.72	0.00018
28.20	0.00093	3.43	0.00021
31.29	0.00113	3.07	0.00023
34.03	0.00133	2.69	0.00026
36.36	0.00153	2.30	0.00028
38.19	0.00173	1.94	0.00031
39.44	0.00193	1.62	0.00033
39.98	0.00213	1.35	0.00036
39.75	0.00233	1.12	0.00038
38.71	0.00253	0.92	0.00041
36.90	0.00273	0.77	0.00043
34.46	0.00293	0.64	0.00046
31.55	0.00313	0.53	0.00048
28.38	0.00333	0.45	0.00051
25.15	0.00353	0.37	0.00053
22.02	0.00373	0.32	0.00056
19.11	0.00393	0.27	0.00058
16.47	0.00413	0.23	0.00061
14.14	0.00433	0.20	0.00063
12.11	0.00453	0.17	0.00066
10.37	0.00473	0.15	0.00068
8.88	0.00493		
7.61	0.00513		
6.54	0.00533		
5.63	0.00553		
4.86	0.00573		
4.21	0.00593		
3.66	0.00613		
3.18	0.00633		

4.3.2 Strands

Each strand is a seven-wire steel strand with a grade of 1860 (ultimate stress, MPa), a diameter of 12.7 mm and a steel area of 98.7 mm². The stress-strain relationship is shown earlier in Figure 3.30 and Table 3.9 provides a summary of the material properties. The ABAQUS input (yield stress vs plastic strain) and the stress-strain relationship values are calculated with the constitutive model described in Section 3.2.4.

4.3.3. Reinforcement steel

The reinforcement steel is considered to be grade 400W mild steel with yielding stress of 400 MPa and ultimate stress of 525 MPa, as per the CSA G30.18:21. The stress-strain relationship is shown in Figure 4.4, while Table 4.4 provides a summary of the material properties used in the ABAQUS model. The stress-strain relationship values shown in Table 4.4 are calculated with the constitutive model discussed earlier in Section 3.2.4.

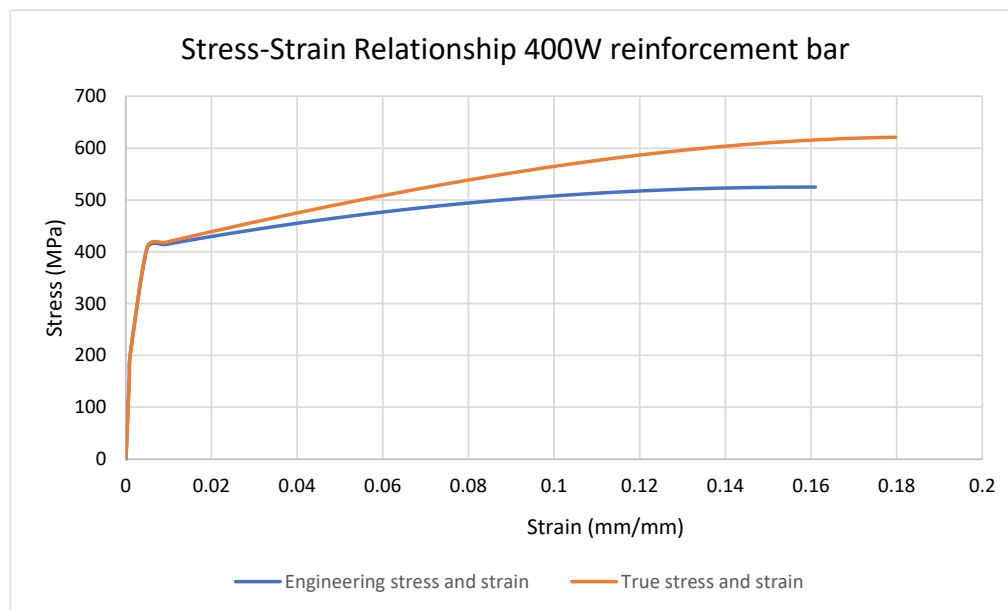


Figure 4.4. 400W - Reinforcement steel stress-strain relationship.

Table 4.4 Material properties and ABAQUS input for the prestressing strands.

Material Parameters			
Grade	400W	Type of Steel	Mild
E (MPa)	200000	Diameter of the strand	12.8 (mm)
Poisson ratio	0.3	Steel Area	129 (mm ²)
Strand behaviour		Strand plastic behaviour (Input ABAQUS)	
True Stress (MPa)	True Strain	True Yield Stress (MPa)	True Plastic Strain
20.16	0.0001	20.1602	0.0
100.84	0.0005	100.8404	0.0
201.76	0.001	201.7595	0.0
417.56	0.005	417.5566	0.006872
432.67	0.009	432.6710	0.014694
447.31	0.017	447.3075	0.022456
461.45	0.021	461.4516	0.030160
475.09	0.025	475.0889	0.037806
488.20	0.032	488.2049	0.045396
500.79	0.036	500.7854	0.052931
512.82	0.044	512.8164	0.060411
524.28	0.048	524.2838	0.067837
535.17	0.052	535.1737	0.075211
545.47	0.055	545.4727	0.082532
555.17	0.063	555.1673	0.089803
564.24	0.067	564.2444	0.097024
572.69	0.074	572.6913	0.104196
580.50	0.078	580.4956	0.111319
584.15	0.085	584.1531	0.114862
587.65	0.089	587.6456	0.118394
590.97	0.093	590.9719	0.121914
594.13	0.100	594.1306	0.125423
597.12	0.103	597.1207	0.128919
599.94	0.111	599.9411	0.132405
602.59	0.114	602.5912	0.135879
605.07	0.121	605.0704	0.139342
607.38	0.125	607.3791	0.142794
609.52	0.132	609.5200	0.146234
611.49	0.139	611.4949	0.149664
613.30	0.142	613.2955	0.153082
614.92	0.146	614.9174	0.156490
616.36	0.153	616.3569	0.159887
617.61	0.156	617.6110	0.163273
618.68	0.163	618.6768	0.166649
619.55	0.166	619.5516	0.170015

4.4 Results

To illustrate the different damage stages, this section first describes a reference specimen (203-HC-(7-0 S)-F (2-meter span) in Subsection 4.4.1. This specimen is provided as a reference to facilitate illustrating the overall behaviour of the specimens, and it should be noted that the behaviour is similar for all specimens but not the same since the type of crack and/or failure changes based on the cross-section, the amount and location of prestressing strands and the span length. Section 4.4.2 to Section 4.4.5 describe the observed trends and the differences in the displacement capacities when different parameters (span length, cross-section and prestress) are used. Section 4.4.6 describes outlier cases that have different damage/failure mechanisms than the ones observed most frequently. Finally, tables are presented with all the numerical results in Section 4.4.7.

4.4.1 Reference Specimen: 203-HC-(7-0 S) (2-meter span)

The slab has a 203 mm depth and 7 prestressed strands on the bottom flange. At the end of the prestress step, cracks can be seen at the bottom ends of the slab which are assumed to be linked by the splitting and bursting effects, as discussed earlier in Chapter 3. After the prestress step is finished (Figure 4.5), the downward vertical displacements are applied at the right end of the HC slab. A rigid connection with the walls induces a concentration of tensile stresses at the interaction between the edge of the wall and the slab when this imposed displacement occurs. The progression of the cracks at the non-displaced end of the slab is shown in Figures 4.6 to 4.9 and the different damage stages represent how deep the cracks have developed (e.g., 10% damage = 10% of the span's depth has been cracked). The cracks start at the top of the slab (at the interface between the

fixed wall and the slab) and they progress vertically, cracking the top flange and webs until it reaches the bottom flange.

This specimen suffers 10% damage, 20% damage, 30% damage and failure at 4.8 mm, 5.0 mm, 5.3 mm, and 9.53 mm of vertical displacements, respectively. The failure is defined when a crack is developed throughout the full depth of the cross-section, as shown in Figure 4.9. At the other end of the slab, where the downward displacement was imposed, the yielding area develops from the bottom to the top of the slab forming cracks. Such an area gets combined with the cracks that the Hoyer Effect induces in the slab, as seen in Figure 4.10. For each specimen, the areas with the most concentration of stresses are at the top of the slab (at the non-displaced end, representing relative upward motion) and at the bottom of the slab (on the end that displaces downward). The critical end of this slab is at the non-displaced end because the induced tensile stresses are at the top, where there is no prestressing.

Since the prestress applied on the hollow-core induces tensile stresses on the top of the slab, and the topping is placed after the prestress step is performed, the concrete topping does not crack/yield at the same displacement as the hollow-core. As seen in Figures 4.6 to 4.9, the principal strains are discontinuous from the top of the topping to the top of the slab. Therefore, extra models were used, where the topping was placed before the prestress step in order to ensure that the hollow-core and topping are behaving integrally. As seen in Figure 4.11, when the prestress is applied to the hollow-core and the slab together, the strains behave in a continuous way, indicating that they act as an integral system. Also, this figure was intentionally modelled with a “non-continuous” and “continuous” mesh configurations between the slab and topping in order to ensure that such configurations were not the potential cause for the discontinuity of the strain results.

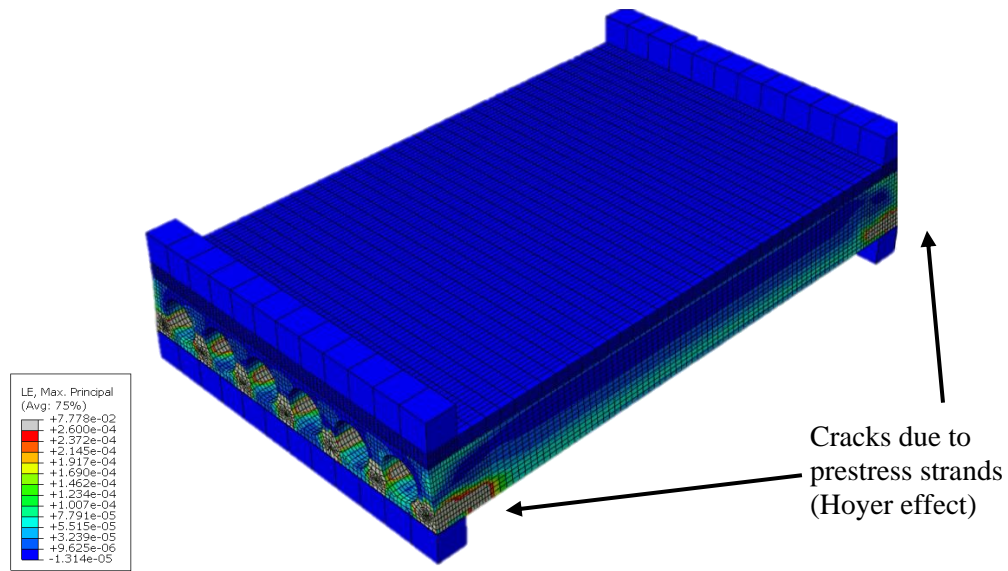


Figure 4.5. 203-HC-(7-0 S)-2 at the beginning of the incompatibility of the displacement step. The yielding areas are shown in gray colour.

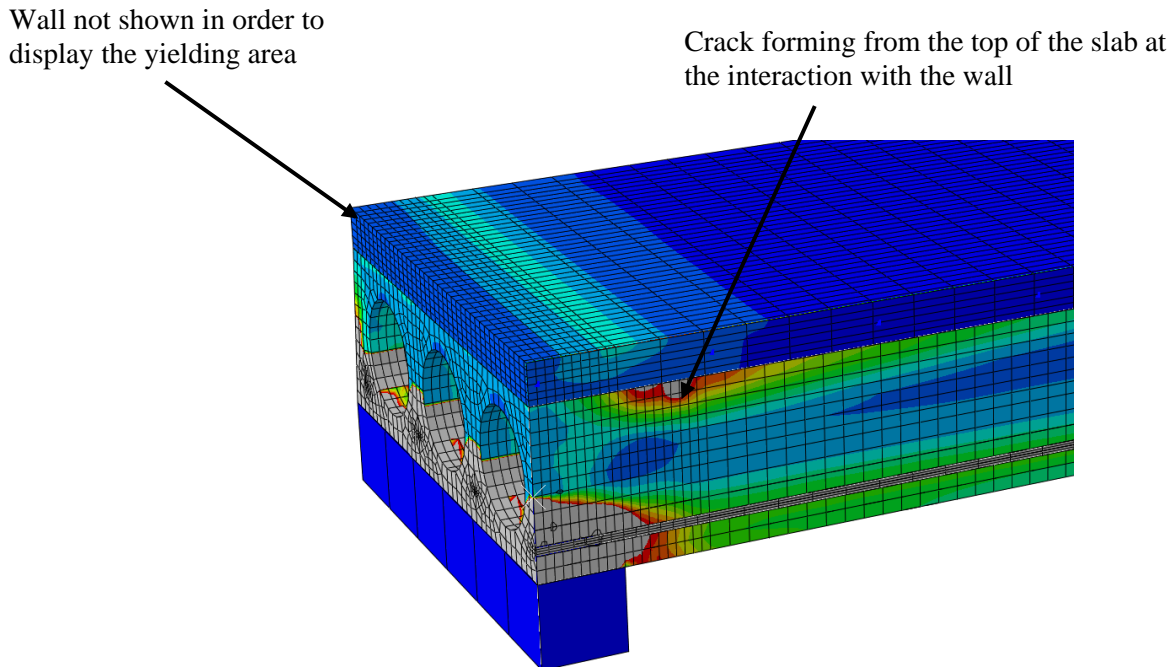


Figure 4.6. 203-HC-(7-0 S)-2 (at the non-displaced end, representing relative upward motion) at 10% damage. The yielding areas are shown in gray colour.

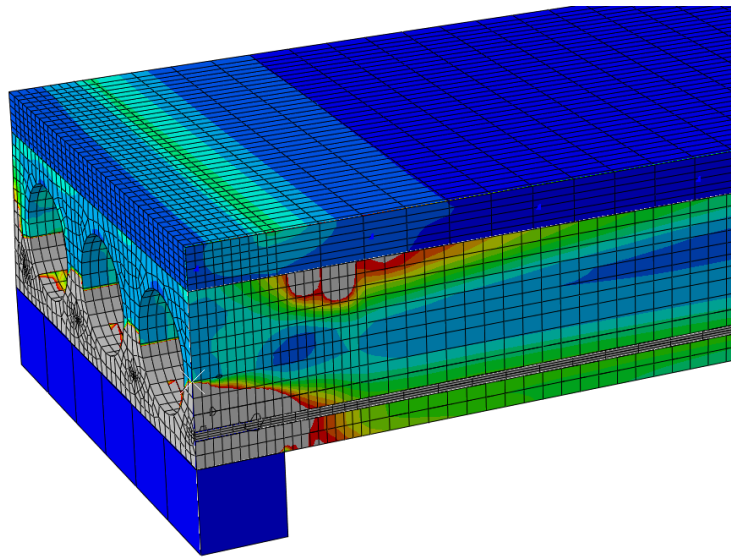


Figure 4.7. 203-HC-(7-0 S)-2 (at the non-displaced end, representing relative upward motion) at 20% damage. The yielding areas are shown in gray colour.

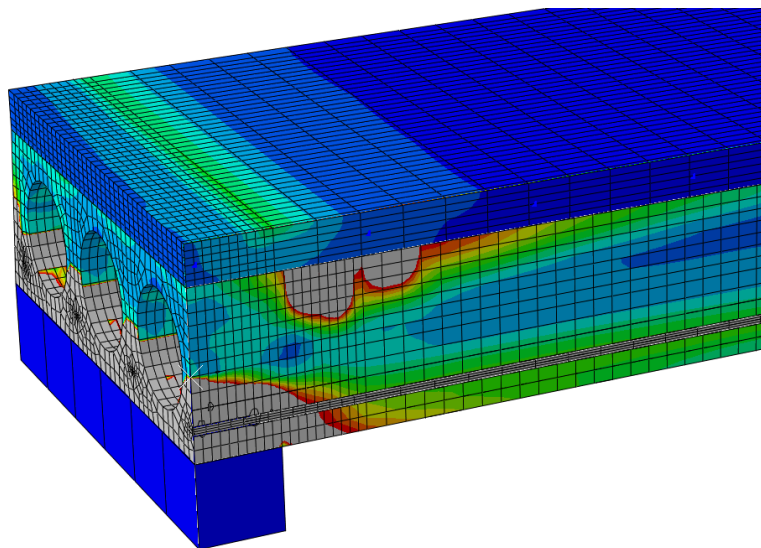


Figure 4.8. 203-HC-(7-0 S)-2 (at the non-displaced end, representing relative upward motion) at 30% damage. The yielding areas are shown in gray colour.

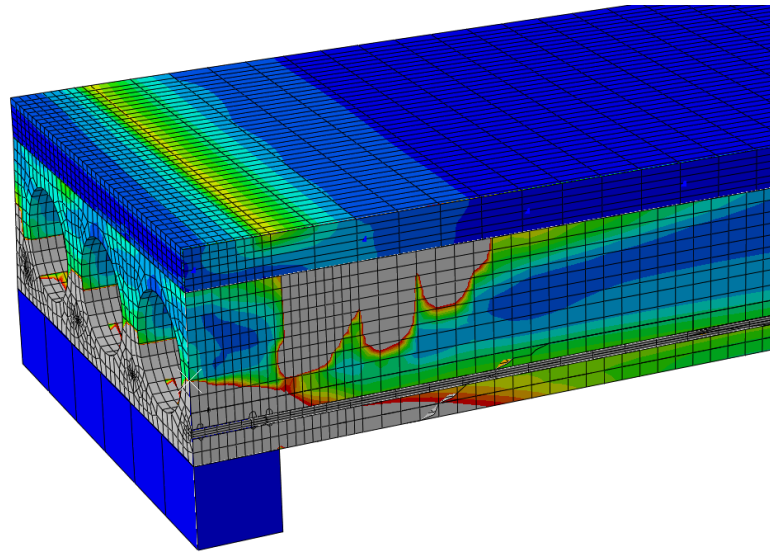


Figure 4.9. 203-HC-(7-0 S)-2 (at the non-displaced end, representing relative upward motion) at the failure stage. The yielding areas are shown in gray colour.

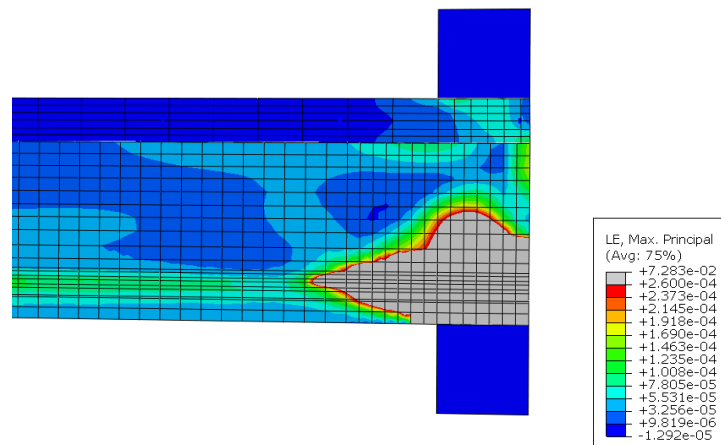


Figure 4.10. 203-HC-(7-0 S)-2 (displacement end, representing a relative downward motion) at the 30% damage stage. The yielding areas are shown in gray colour.

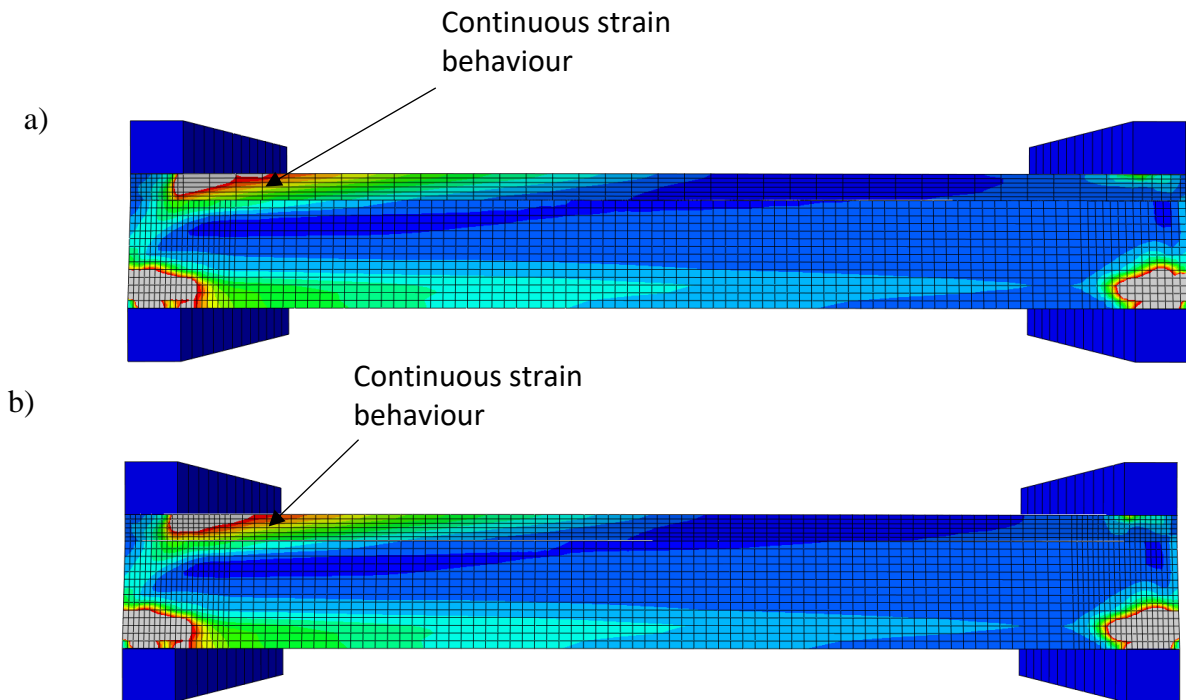


Figure 4.11. 203-HC-(7-0 S)-2 (prestress being applied at the hollow-core and topping) showing a continuous strain behaviour between the topping and the slab with a) “non-continuous” and b) “continuous” meshing configurations between them.

4.4.2. Effect of span length

Three different spans are applied in this investigation to evaluate the displacement incompatibility capacity. Considering that the spans in a masonry building are not usually longer than 9 m, the chosen slabs for this investigation are 2 m, 5 m, and 8 m. The development of the cracks on the slab shown in the previous section is meant to be used as a reference for all the specimens since the crack development for each span is generally similar but with a different starting point of the cracks, as shown in Figures 4.12 – 4.14. As shown in Figure 4.12, for spans of 2 meters, several yielding areas/cracks are developed vertically at the 30% damage stage. For 5 and 8-meter spans, a smaller and narrower yielding area is developed vertically at the 30% damage stage (Figures 4.13 and 4.14), but the 8-meter span had an offset of the yielding area of approximately 40 mm towards the center of the slab.

As shown in Figure 4.15, for the 2-meter span, the displacement capacity is 5.3 mm at 30% damage and 9.5 mm at failure. For the 5-meter span, the displacement capacity increases, allowing for 36.5 mm at 30% damage and 52.7 mm at failure, which means nearly 6.8 times more displacement capacity at the 30% damage and 5.5 times more displacement capacity at failure in comparison with the 2-meter span. Finally, for the 8-meter span, the displacement capacity increases further by allowing 77 mm and 103.6 mm at 30% damage and failure, respectively. Results show an increase in the displacement capacity on longer spans in comparison to shorter spans.

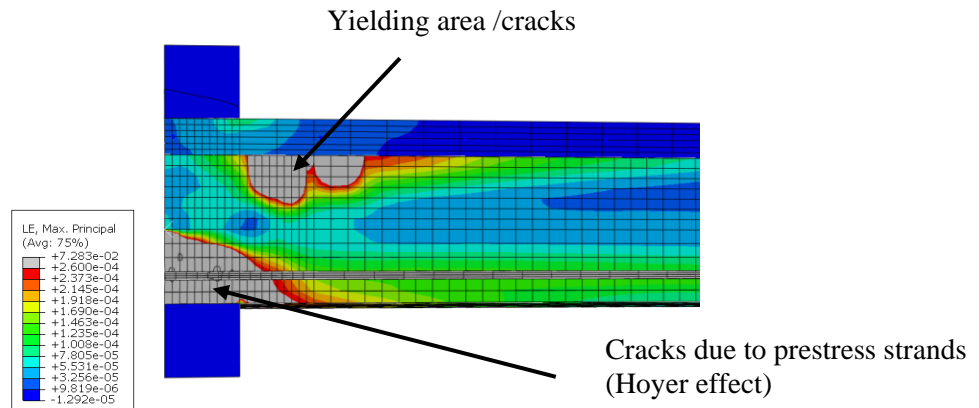


Figure 4.12. 203-HC-(7-0 S)-2 at 30% damage stage. The yielding areas (cracks) are shown in gray colour.

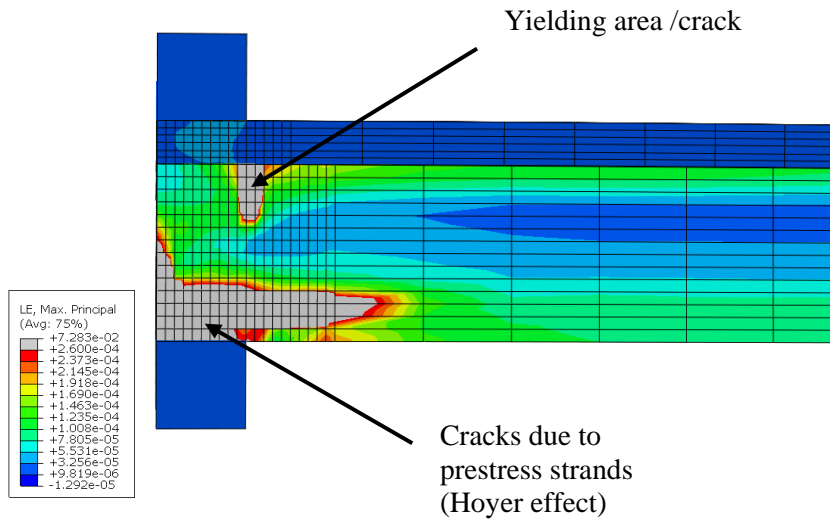


Figure 4.13. 203-HC-(7-0 S)-5 at 30% damage stage. The yielding areas are shown in gray colour.

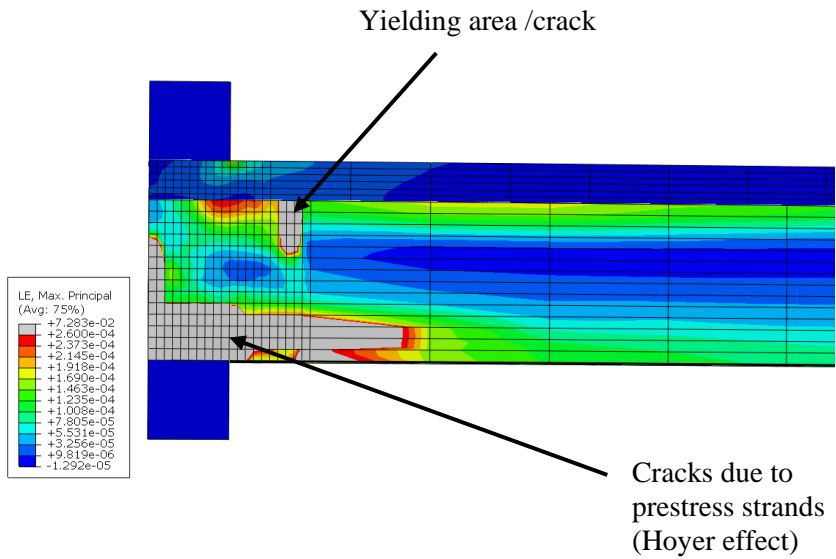


Figure 4.14. 203-HC-(7-0 S)-8 at 30% damage stage. The yielding areas are shown in gray colour.

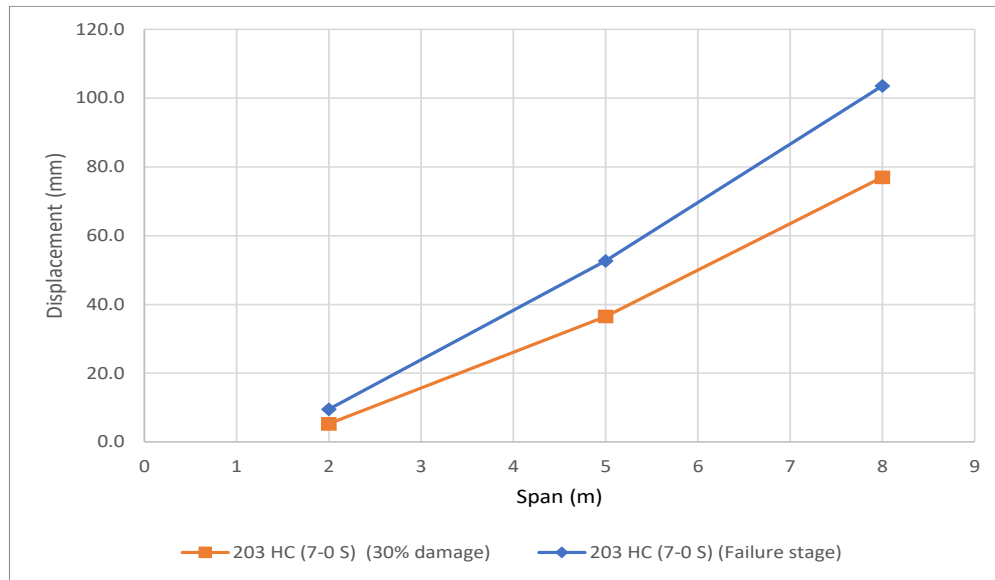


Figure 4.15. Displacement capacity by span length (203 HC (7-0 S)) at 30% damage and failure stage.

4.4.3. Effect of hollow-core depth

The displacement capacities for different hollow-core slab depths, but with the same span length, are relatively similar. For 2-meter spans, the displacement capacities are between 4.1 and 5.3 mm at the 30% damage state and between 7.4 and 9.5 mm at failure, as seen in Figure 4.16. For 5-meter spans, the displacement capacity increases, allowing between 36.5 to 46.9 mm at the 30% damage state and between 52.7 and 58.7 mm at failure (Figure 4.17). Finally, for 8-meter spans, the displacement capacity increases further by allowing 76 mm and 106 mm on average at 30% damage and failure stages, respectively, as seen in Figure 4.18.

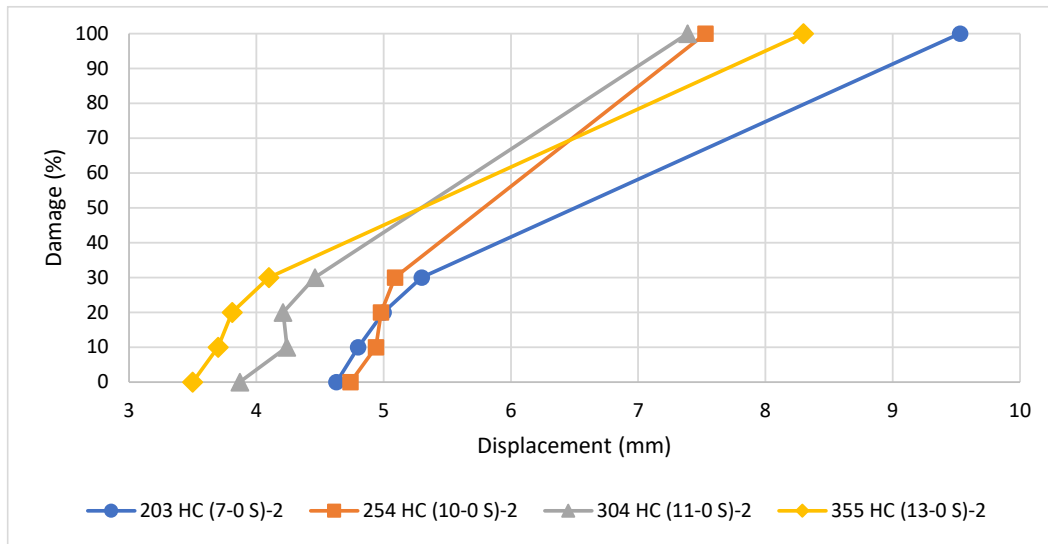


Figure 4.16. Displacement-damage relationship (HC with prestressing only at the bottom)-2-meter span.

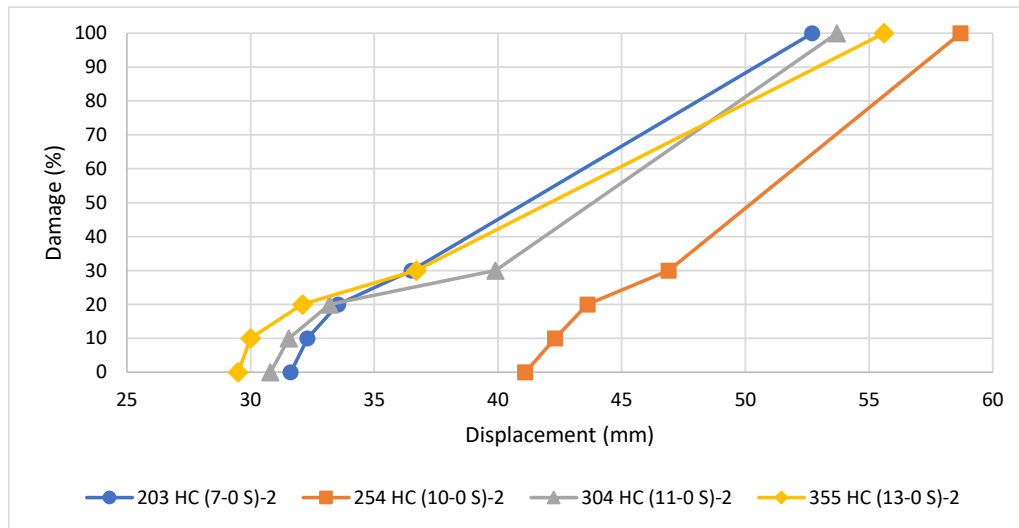


Figure 4.17. Displacement-damage relationship (HC with prestressing only at the bottom)-5-meter span.

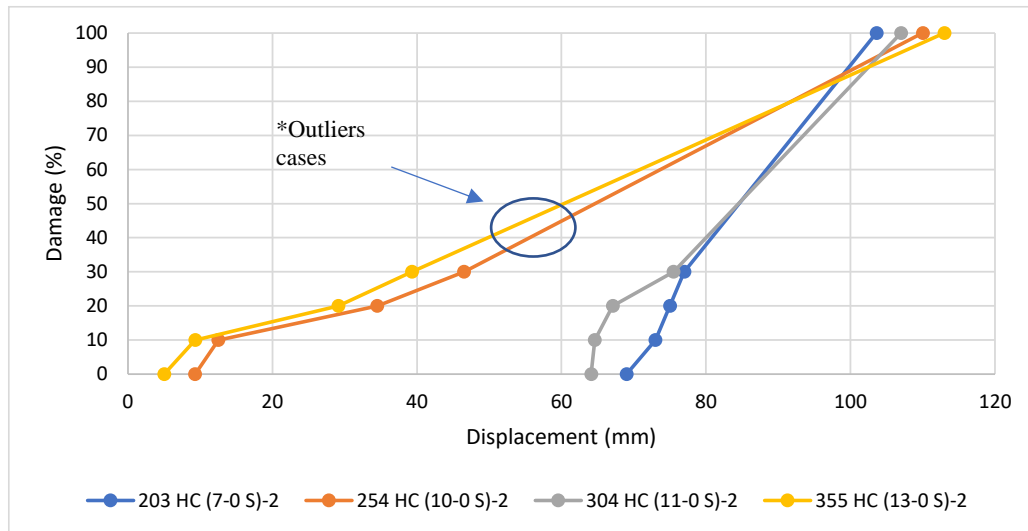


Figure 4.18. Displacement-damage relationship (HC with prestressing only at the bottom)-8-meter span. *

*The cross-sections 254-HC and 355 HC (8-meter span) had a different type of failure than the other cross-sections. The “Outlier Cases” subsection 4.4.6 describes and illustrates such failures.

4.4.4. Effect of adding top prestressing

The main objective of the prestress is to pre-compress the most critical areas in the slab in order to delay the appearance of tensile stresses in the concrete. The prestress is an important factor in this type of connection (and wall-diaphragm interaction) due to the tensile stresses at the top of the slab at the non-displaced end (representing relative upward motion) and at the bottom of the slab at the end that displaces relatively downward. Figure 4.19 shows an example of a slab with prestressing at the top and bottom in order to show that the critical end is still the non-displaced end, as was typical for all cases.

As seen in Figures 4.20 to 4.22, adding prestressing steel to the top flange allowed a higher displacement capacity than for the specimens with prestressing at the bottom only. For instance, when the prestress is provided at both flanges, specimens with a 2-meter span allow a

displacement capacity between 13.4 and 25.5 mm at 30% damage and between 33.7 and 52.3 mm at failure, which means an average of 4 times and 5 times higher capacity at the 30% damage and at the failure stage, respectively, than the only-bottom-prestressed specimens. For the specimens with a 5-meter span, the displacement capacity reached 55 to 79 mm at 30% damage and 91.3 to 118 mm at failure, which means an average of 1.6 times and 1.8 times higher capacity at 30% damage stage and failure stage, respectively, than the only-bottom-prestressed specimens. Finally, for 8-meter spans, the displacement capacity increases further allowing between 92 – 130 mm at 30% damage and 155 – 179 mm at failure, which means an average of 1.4 times and 1.6 times higher capacity at the 30% damage stage and at the failure stage, respectively, than the only-bottom-prestressed specimens. These results vary slightly depending on the cross-section as shown in Figures 4.20, 4.21 and 4.22.

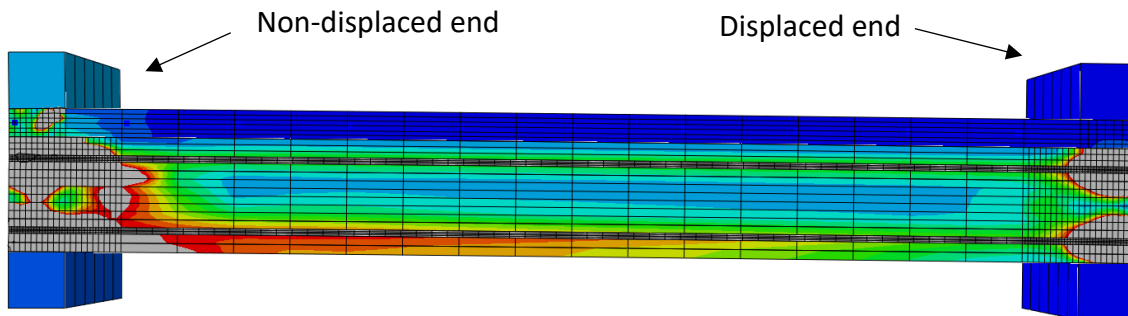


Figure 4.19. 203 HC (7-5 S)-2 at the failure stage.

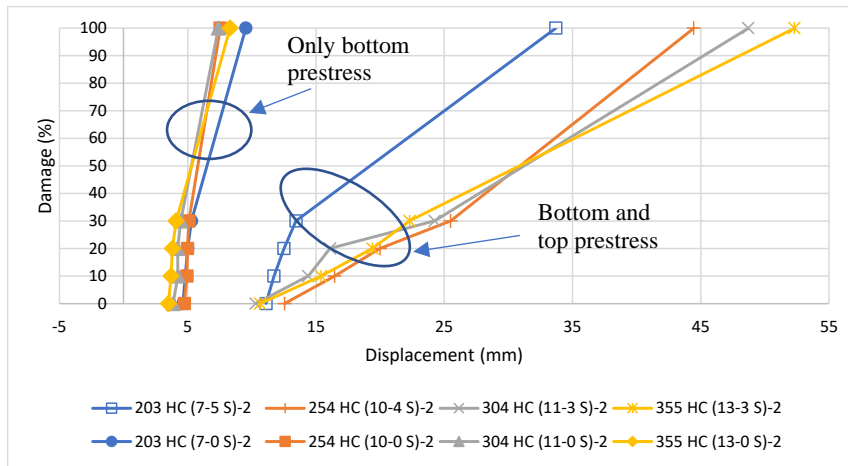


Figure 4.20. Displacement-damage relationship comparison between HCs with prestressing only at the bottom and HCs with prestressing at the top and bottom)-2-meter span.

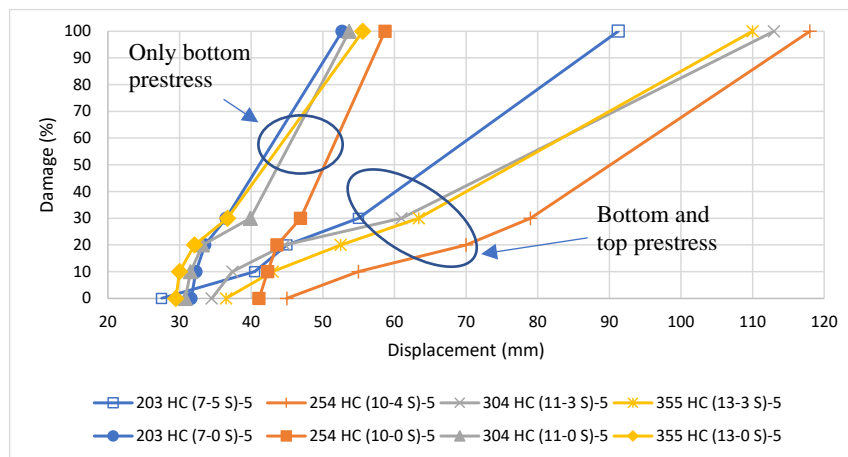


Figure 4.21. Displacement-damage relationship comparison between HCs with prestressing only at the bottom and HCs with prestressing at the top and bottom)-5-meter span.

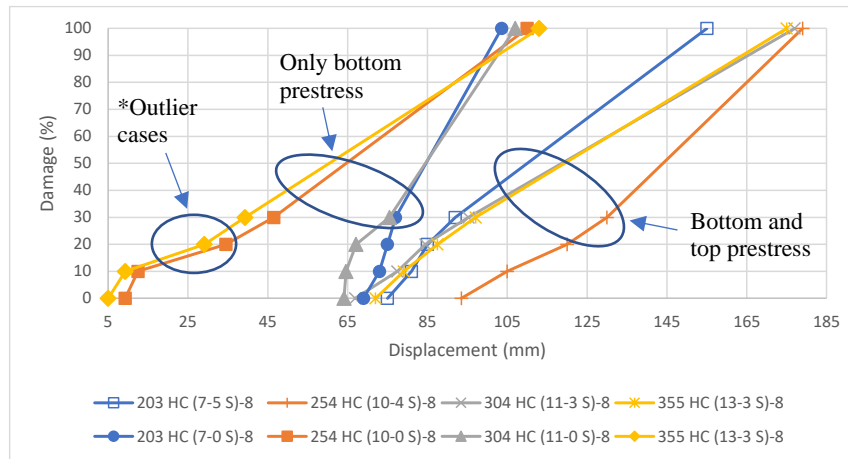


Figure 4.22. Displacement-damage relationship comparison between HCs with prestressing only at the bottom and HCs with prestressing at the top and bottom)-8-meter span.

4.4.5. Outlier cases

It is observed that two specimens (called “outlier cases”) have different types of failure. These cases are 254 HC (10-0 S) F (8 meters) and 355 HC (13-0 S) F (8-meters). These two specimens started yielding on the cross-sectional face instead of the typical vertical crack, as shown in Figures 4.23 and 4.24. For these specimens, the displacement capacity at 10%, 20% and 30% damage stage are much lower than specimens with the common cracking development. However, at the failure stage, the displacement capacity is similar to that of the non-outlier. Meshing was eliminated as the potential cause of such difference in the behaviour by creating a finer mesh for these two specimens, resulting in the same behaviour. However, at this time, it is not clear whether the surprising results represent a real difference in behaviour or an artificial modelling artifact. Therefore, these results are included with a note that experimental research is still required.

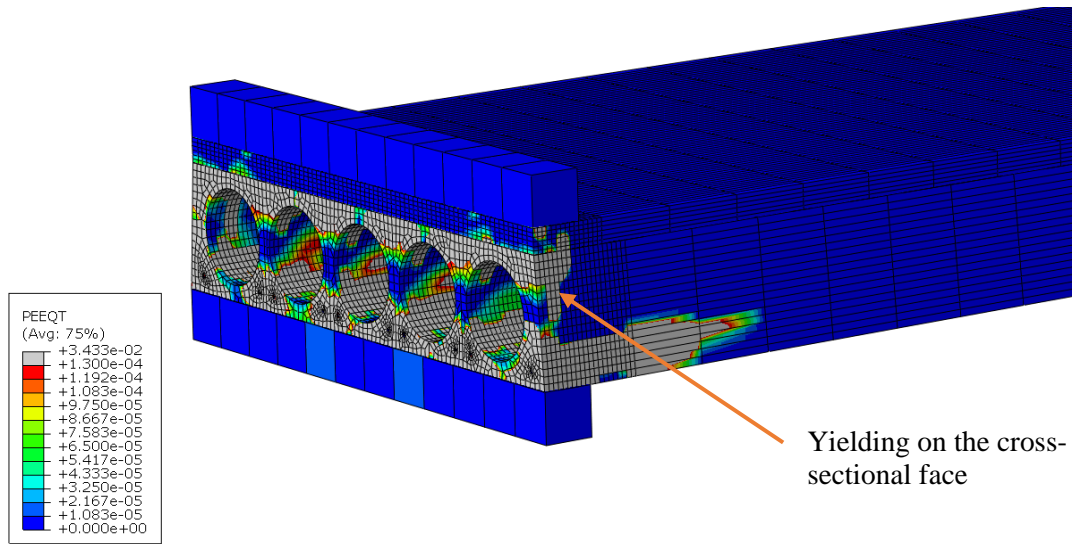


Figure 4.23. Yielding on the cross-sectional face at the failure stage (254-HC-(10-0 S)-8).

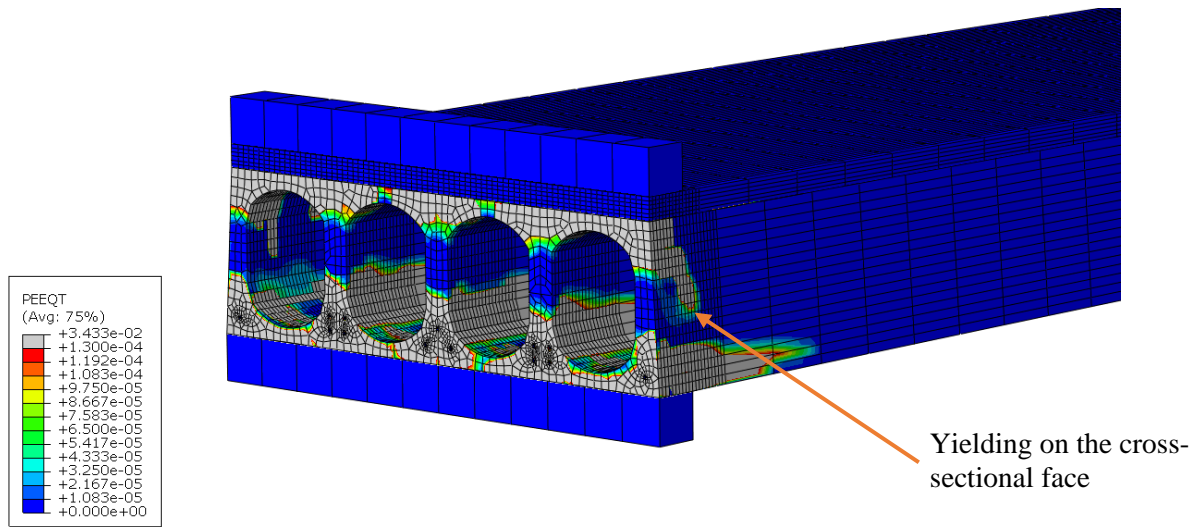


Figure 4.24. Yielding on the cross-sectional face and a downwards diagonal crack developing at 30% damage stage (355-HC-(13-0 S)-8).

4.4.6. Tables of results

Tables 4.5, 4.6 and 4.7 summarize the results for each specimen at the specific damage stages that this investigation focused on. The “outlier cases” are highlighted with an orange colour. A completely fixed connection is assumed in this investigation, but since the connection is not monolithic but rather an assembly with masonry, concrete and grout, it is possible that such a connection allows small rotations at the ends of the slab that could increase the displacement capacity. Therefore, the following tables are considered to contain conservative results that must be compared and verified with experimental testing.

After obtaining these results, it is not unreasonable to think that hollow-core slabs can be used in buildings with rocking walls. The vertical displacement demand will mostly depend on the walls' length, their relative position within each other and the drift percentage. For example, consider a case where wall A is an 8-meter-long rocking wall and wall B is a 2-meter-long rocking wall, which both support a 203 HC (7-0 S)-8 slab. As shown in Figure 4.25, the walls are parallel to each other and wall B is placed 3-meter offset from its longitudinal center (in the longitudinal direction) relative to one of the ends of wall A. When the walls rock in the direction of wall A's farthest end to wall B, and considering a 1.88% drift, the incompatible vertical displacements along the length of wall B will be 75.2 mm (making wall A higher relative to wall B by 75.2 mm). According to Table 4.7, this slab will be at a 20% damage state at such a displacement. As in the previous example, the displacement capacities results (summarized in Tables 4.5, 4.6 and 4.7) can help engineers to decide on the hollow-core slab with a specific amount of prestressing and a specific span length that allows the displacement demand of their design.

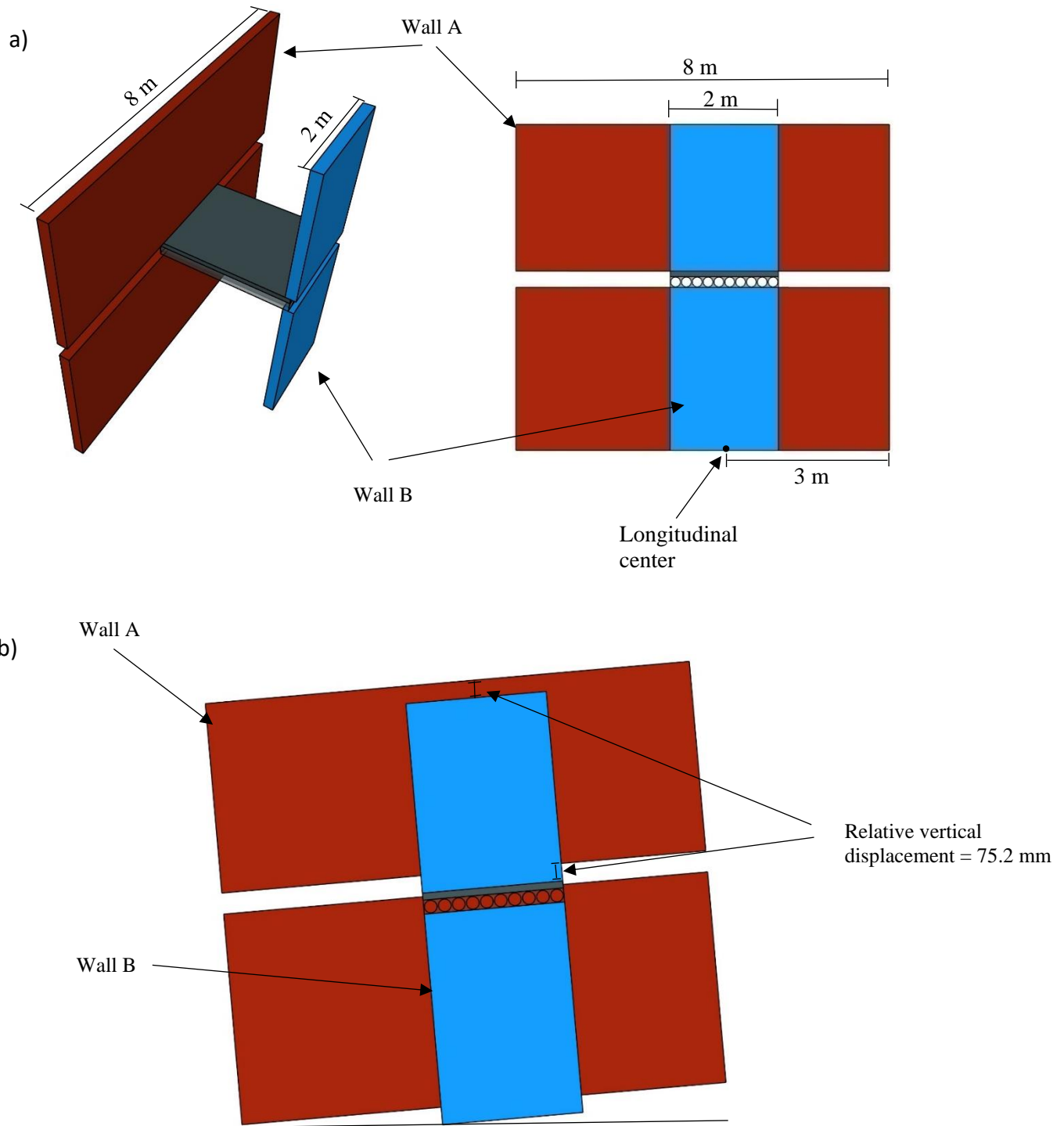


Figure 4.25. Example dimensions: a) Isometric and elevation view before rocking; b) Elevation view when rocking.

Table 4.5. Displacement capacities with 2 m span.

Displacement (mm) Span: 2 meters					
Specimen/Damage	0%	10%	20%	30%	Failure
203 HC (7-0 S)	4.6	4.8	5.0	5.3	9.5
254 HC (10-0 S)	4.7	4.9	5.0	5.1	7.5
304 HC (11-0 S)	3.9	4.2	4.2	4.5	7.4
355 HC (13-0 S)	3.5	3.7	3.8	4.1	8.3
203 HC (7-5 S)	11.1	11.7	12.5	13.4	33.7
254 HC (10-4 S)	12.6	16.5	20.0	25.5	44.5
304 HC (11-3 S)	10.3	14.4	16.1	24.3	48.7
355 HC (13-3 S)	10.7	15.4	19.4	22.3	52.3

Table 4.6. Displacement capacities with 5 m span.

Displacement (mm) Span: 5 meters					
Specimen/Damage	0%	10%	20%	30%	Failure
203 HC (7-0 S)	31.6	32.3	33.5	36.5	52.7
254 HC (10-0 S)	41.1	42.3	43.6	46.9	58.7
304 HC (11-0 S)	30.8	31.6	33.2	39.9	53.7
355 HC (13-0 S)	29.5	30.0	32.1	36.7	55.6
203 HC (7-5 S)	27.5	40.5	45.0	55.0	91.3
254 HC (10-4 S)	45.0	55.0	70.0	79.0	118.0
304 HC (11-3 S)	34.5	37.4	44.7	61.0	113.0
355 HC (13-3 S)	36.5	43.0	52.5	63.4	110.0

Table 4.7. Displacement capacities with 8 m span.

Displacement (mm) Span: 8 meters					
Specimen/Damage	0%	10%	20%	30%	Failure
203 HC (7-0 S)	69.0	73.0	75.0	77.0	103.6
254 HC (10-0 S)	9.3	12.5	34.5	46.5	110.0
304 HC (11-0 S)	64.1	64.6	67.1	75.5	107.0
355 HC (13-0 S)	5.0	9.3	29.1	39.3	113.0
203 HC (7-5 S)	75.0	81.0	85.0	92.0	155.0
254 HC (10-4 S)	93.5	105.0	120.0	130.0	179.0
304 HC (11-3 S)	66.9	77.5	84.5	95.3	177.0
355 HC (13-3 S)	72.0	79.1	87.5	97.1	175.0

*Orange highlight: Outlier cases

Chapter 5: Conclusion and Recommendations

5.1 Conclusion

Controlled rocking masonry walls have gained attention as a potential alternative to limit structural damage and residual drifts as seismic engineering moves towards developing resilient self-centering buildings. Even though recent research studies, discussed earlier in Chapter 1, have had positive results regarding the performance of controlled rocking masonry walls, the wall-diaphragm interaction has raised concerns due to potential displacement incompatibilities between the controlled rocking masonry wall and the slab for systems that rely mainly on the vertical gravitational loads for their self-centering performance, where the vertical movement between the structural components of such systems cannot be isolated. As described in Chapter 2, there are two main incompatibilities that can arise from such an interaction: angular displacement incompatibilities and vertical displacement incompatibilities. The angular displacement incompatibility occurs when two rocking walls support a hollow-core slab and rock with a different angle, while the vertical displacement incompatibility occurs when two rocking walls with different lengths support a hollow-core slab and rock with the same angle. The current thesis focused on quantifying the behaviour and damage of hollow-core slabs due to displacement incompatibility when such slabs are supported by rocking walls.

In order to understand the performance of hollow-core slabs and their ability to withstand vertical displacement incompatibilities, the parametric study compared different span lengths (2, 5 and 8 meters), cross-section geometries (203, 254, 304 and 355 depths), and amounts of prestress (only at the bottom flange and at both the top and bottom flange). The modelling techniques that were used to develop the finite element model in this investigation were validated with

experimental test results from Pachalla et al. (2016). Based on the validation described in Chapter 3, the finite element model was able to capture the behaviour of prestressed hollow-core slabs. Due to the varying parameters (cross-section, span length and amount of prestressing), 24 models were created and analyzed with ABAQUS 6.18 commercial software. The results were divided into five different damage states and the displacement capacity was reported at these damage states, namely initial damage, 10% damage, 20% damage, 30% damage and failure of the slab. The damage percentage represents how deep a crack has developed (e.g., 10% damage = 10% of the slab's depth has been cracked). In general, the cracking starts at the top of the hollow core unit (typically below the topping, which is added after the unit is prestressed) and develops vertically towards the bottom flange until failure occurs.

The span length has a significant impact on the displacement capacity. Results show that longer spans provide higher displacement capacities than shorter spans. For example, for spans with prestressing only at the bottom flange, the displacement capacity at the 30% damage stage increases by 8.4 times when the span length is increased from 2-meter to 5-meter and by 1.9 times when the span length is further increased from 5-meter to 8-meter span.

The different cross-section depths and geometries do not have a significant impact on the displacement capacities and the results did not follow any obvious trend regarding the cross-section geometries.

The prestress provides a pre-compression with the objective of delaying the appearance of tensile stresses in the concrete. Therefore, the location of the prestress plays an important role in this structural system since the areas with the greatest concentrations of stress are at the top of the slab (at the non-displaced end, representing relative upward motion) and at the bottom of the slab (at the displaced end, representing a relative downward motion). Results show that applying

prestress at the top and bottom flanges also provides a significant increment in the displacement capacity of the slab in comparison with slabs with prestressing only at the bottom flange.

The vertical displacement demand will mostly depend on the walls' length, their relative position within each other and the drift percentage. The results in Tables 4.5, 4.6 and 4.7 can help engineers to select a hollow-core slab, with a specific amount of prestressing, that accommodates the displacement demand and span length of their design. If these displacement capacities do not work for a specific system, the designer would need to consider a special connection (e.g., a connection that allows rotation at its ends).

The obtained results give positive and hopeful outcomes for the usage of hollow-core slabs on ED-CRMWs or similar systems that require this interaction since the range of capacities can accommodate vertical incompatibility of displacements in potential situations due to the rocking mechanism, providing a resilient wall-slab connection. However, experimental research is still needed to validate the results presented in this thesis.

5.2. Recommendations

Future research could be focused on the experimental testing of hollow-core slabs with vertical displacement incompatibilities at their ends in order to have the exact displacement capacities of this structural system and to validate the results presented in this thesis. Also, different amounts and locations of prestress of each hollow-core cross-section need to be investigated in order to optimize the design.

Research should also be focused on quantifying the vertical forces that might be imposed on the wall when the hollow-core is deformed by the incompatibility of displacements. Such forces are expected to increase the resistance of the walls to rocking.

Researching beyond the fixed connection can be an important step for the future of this structural system because having another type of connection (e.g., pin-pin connection) could potentially provide higher displacement capacities due to the rotational capability and different boundary conditions. A connection that allows rotation prevents flexural forces caused by vertical displacement incompatibilities. The testing and validation of this connection can provide an alternative option if a fixed connection cannot accommodate the displacement demand.

Finally, this thesis focused on vertical displacement incompatibilities; however, further research could focus on the effects that angular displacement incompatibilities (mentioned in Chapter 2) and the combination of both vertical and angular incompatibilities.

References

- ABAQUS User Manual 6.14, Dassault Systems Simula Corp. Providence, RI, United States, 2014.
- ACI (American Concrete Institute) Committee 318. 2011. Building Code Requirements for Structural Concrete (ACI 318-11) and Commentary (ACI 318R-11). Farmington Hills, MI: ACI.
- Arab, A., Badie, S., Manzari, M. (2011). A methodological approach for finite element modeling of pretensioned concrete members at the release of pretensioning, *Engineering Structures*, 33, 1918-1929.
- Ashour, A., & El-Dakhakhni, W. (2016). Influence of Floor Diaphragm–Wall Coupling on the System-Level Seismic Performance of an Asymmetrical Reinforced Concrete Block Building, *Journal of Structural Engineering ASCE*, 142(10), 0733-9445.
- ASTM. (2006). Standard Specification for Steel Strand, Uncoated 7-wire for Prestressed Concrete, *ASTM*, A 416/A416M – 06.
- Broo, H., Lundgren, K., Engstrom, B. (2005). Shear and torsion interaction in prestressed hollow-core units, *Magazine of Concrete Research*, 57, No. 9, 521–533.
- Broo, H., Plos M., Lundgren, K., Engstrom, B. (2007). Simulation of shear-type cracking and failure with non-linear finite element method, *Magazine of Concrete Research*, 59, No. 9, 673–687.
- Broo, H., Lundgren, K., Engstrom, B. (2007). Shear and tension in prestressed hollow-core units: finite element analyses of full-scale tests, Chalmers University of Technology.

- Buettner, D.R., and Becker, R.J. (1998). Manual For the Design of Hollow-core slabs 2nd Edition, Precast / Prestressed concrete Institute, Chicago Illinois.
- Bull, D., and Matthews, J. (2003). Proof of Concept Tests for Hollow-core Floor Unit Connections. The University of Canterbury, Department of Civil Engineering, Christchurch, New Zealand.
- Chang, G.A., and Mander, J.B. (1994) "Seismic Energy Based Fatigue Damage Analysis of Bridge Columns: Part 1 – Evaluation of Seismic Capacity," NCEER Technical Report No. NCEER-94-0006, State University of New York, Buffalo, N.Y.
- Chang, G.A., Mander, J.B., Cedeño, G.A., Dominguez, D.A. (1996). Fiber-Element Modeling of the Cyclic Biaxial Behaviour of R/C Columns, Eleventh World Conference on Earthquake Engineering, ISBN: 0 09 042822 3.
- Collins, M. P., and Mitchell, D. (1987). Prestressed Concrete Basics, Canadian Prestressed Concrete Institute.
- Coreslabs. (2009). Coreslabs Structures (ON) Inc. Load Tables, Coreslabs Structures.
- CPCI. (2017). CPCI Design Manual 5th Edition Precast and Prestress Concrete, Canadian Prestressed Concrete Institute.
- CSA Group (1). (2019). Canadian Highway Bridge Design Code S6:19, CSA Group.
- CSA Group (2). (2019). Design of Concrete Structures A23.3:19, CSA Group.
- CSA Group (3). (2021). Carbon steel bars for concrete reinforcement G30.18:21, CSA Group.

- CSA Group (4). (2019). Commentary on Canadian Highway Bridge Design Code S6.1:19, CSA Group.
- Dassault Systemes. (2018). ABAQUS Unified FEA, Version 6.18, Dassault Systemes.
- Demir, A., Ozturk, H., Edip, K., Stojmanovska, M., & Bogdanovic, A. (2018). Effect of Viscosity Parameter on The Numerical Simulation of Reinforced Concrete Deep Beam Behavior, TOJSAT, Volume 8, Issue 3.
- Derkowski, W., and Surma, M. (2015). Torsion of precast hollow-core slabs, Technical Transactions, April, 31-43, Cracow University of Technology.
- East, M., Li, J. Ezzeldin, M., & Wiebe, L. (2022) “Development of a Flexural Yielding Energy Dissipation Device for Controlled Rocking Systems.” *Journal of Structural Engineering ASCE*, DOI: 10.1061/(ASCE)ST.1943-541X.0003461.
- Expocrete. (2018). Hollow-core Concrete Solutions. Expocrete.
- Fenwick, R., and Gardiner, D. (2010). Assessment of hollow-core floors for seismic performance, Research Report, University of Canterbury.
- Hassanli, R., ElGawady, M., and Mills, J. (2016). “Experimental investigation of in-plane cyclic response of unbonded-posttensioned masonry walls.” *Journal of Structural Engineering*, 142(5), 04015171-1-15
- Hatzinikolas, M., Korany, Y., and Brzerv, S. (2015). *Masonry Design for engineers and architects*, 4th edition, Canadian Masonry Publications, pp. 428.

- Henry, R. S., Ingham, J., and Sritharan, S. (2011). Self-centering Precast Concrete Walls for Buildings in Regions with Low to High Seismicity, Ph.D. Thesis: The University of Auckland, NZ.
- Henry, R. S., Ingham, J., & Sritharan, S. (2012). Wall-to-floor interaction in concrete buildings with rocking wall systems, *NZSEE Conference*, Paper 72.
- Hognestad, E. (1951). Study of Combined Bending and Axial Load in Reinforced Concrete Members. Bulletin 399. Engineering Experiment Station, the University of Illinois at Urbana-Champaign.
- Jensen, J. (2006). The Seismic Behaviour of Existing Hollow-core Seating Connections Pre and Post Retrofit, MEng. Thesis: University of Canterbury.
- Khanal, A. (2019). Review of Hollow-core Floor Slab in New Zealand – History of Practice, Past Research, and Failure Modes Seen in Research and Recent Earthquakes, MSc. Thesis: The University of Toledo.
- Laursen, P. T. and Ingham, J. M. (2001). “Structural Testing of Single-Story PostTensioned Concrete Masonry Walls.” *The Professional Journal of Masonry Society*, 19(1), 69-82.
- Laursen, P. T. and Ingham, J. M. (2004a). “Structural testing of enhanced posttensioned concrete masonry walls.” *ACI Journal*, 101(6), 852-862.
- Laursen, P. T. and Ingham, J. M. (2004b). “Structural testing of large-scale posttensioned concrete masonry walls.” *Journal of Structural Engineering*, 130(10), 1497-1505.
- Lee Kim, D. (2019). Development of an Axial Yielding Energy Dissipation Device for Controlled Rocking Masonry Walls, MAsc Thesis: McMaster University.

- Li, J. (2019). Development of a Flexural Yielding Energy Dissipation Device for Controlled Rocking Masonry Walls, MAsc Thesis: McMaster University.
- Lin, Z., Wood, L. (2003). Concrete uniaxial Tensile Strength and Cylinder Splitting Test, *Journal of Structural Engineering ASCE*, 129(5), 692-698.
- Liu, Q. (2016). Study on Interaction between Rocking-Wall System and Surrounding Structure, Ph.D. Thesis: University of Minnesota, Minneapolis, MN.
- Matthews, J. (2004). Hollow-Core Floor Slab Performance Following a Severe Earthquake, Ph.D. Thesis: University of Canterbury.
- Marriott, D. J., Pampanin, S., Palermo, A., and Bull, D. (2008). Dynamic testing of precast, post-tensioned rocking wall systems with alternative dissipating solutions, The 14th World Conference on Earthquake Engineering 41:90–103.
- Meng, X. (2016). Shear Strengthening of Prestressed Hollow-core Slabs Using Externally Bonded Carbon Fiber Reinforced Polymer Sheets, University of Windsor.
- Pachalla, S.K.S., Prakash, S.S. (2016). Load resistance and failure modes of GFRP composite strengthened hollow-core slabs with openings, Precast/Prestress Concrete Institute.
- Parkhats, V. (2018). Problem of cracks in prestressed hollow core slabs. Silesian University of Technology.
- Priestley, M. J. N., Sritharan, S., Conley, J. R., & Pampanin, S. (1999). Preliminary results and conclusions from the PRESSS five-story precast concrete test building. *PCI Journal*, 44, 42–67.

- Priestley, M. J. N. (2000). Performance-based seismic design, *Bulletin of the New Zealand Society for Earthquake Engineering* 33(3), 325–347
- Ramberg, W., and W. R. Osgood. (1943). “Description of Stress-Strain Curves by Three Parameters.” Technical Note 902. National Advisory Committee for Aeronautics.
- Schoettler, M. J., Belleri, A., Dichuan, Z., Restrepo, J. I., & Fleischman, R. B. (2009) Preliminary results of the shake-table testing for the development of a diaphragm seismic design methodology. *PCI Journal*, 54(1), 100-124.
- Schultz, A. & Kalliontzis, D. (2017) Characterizing the In-Plane Rocking Response of Masonry Walls with Unbonded Posttensioning, *Journal of Structural Engineering ASCE*, 143(9), 0733-9445.
- SESOC, NZSEE, & NZCS. (2009). Seismic Performance of Hollow-core Floor Systems: Guidelines for Design Assessment and Retrofit, Preliminary Draft, Department of Building and Housing.
- Smith, A. H., Banting, B. R., Stubbs, D., Wierzbicki, J., Kasin, S., Guzman, M., & Crumb, B. (2020). Atlantic Canada Study: Building structure cost comparison. Canada Masonry Design Centre.
- Sritharan, S., Aaleti, S., Henry, R. S., Liu, K.-Y., & Tsai, K.-C. (2008). Introduction to PreWEC and key results of a proof-of-concept test. MJ Nigel Priestley Symposium, 95–106.
- Toranzo, L. A., Restrepo, J. I., Mander, J. B. & Carr, A. J. (2009). Shake-Table Tests of Confined-Rocking masonry Walls with Supplementary Hysteretic Damping, *Journal of Earthquake Engineering*, 13:6, 882-898

- Turon, A., Davila, C.G., Camanho, P.P., Costa, J. (2005) An Engineering Solution for using Coarse Meshes in the Simulation of Delimitation with Cohesive Zone Model, National Aeronautics and Space Administration (NASA).
- Watkins, J. (2017). Seismic Response of Buildings that Utilise Unbonded Post-Tensioned Concrete Walls, The University of Auckland.
- Yassin, A., Ezzeldin, M., Steele, T., & Wiebe, L. (2020). Seismic Collapse Risk Assessment of Posttensioned Controlled Rocking Masonry Wall, *Journal of Structural Engineering ASCE*, 146(5), 0733-9445.
- Yassin, A., Ezzeldin, M., & Wiebe, L. (2022a). Experimental assessment of controlled rocking masonry shear walls without post-tensioning. *Journal of Structural Engineering, ASCE*, 148(4), 04022018.
- Yassin, A., Wiebe, L., & Ezzeldin, M. (2022b). Seismic Design and Performance Evaluation of Controlled Rocking Masonry Shear Walls without Posttensioning. *Journal of Structural Engineering, ASCE* 148(6), 04022059.
- Yapar, O., Basu, P.K., Nordendale, N. (2015). Accurate finite element modelling of pretensioned prestressed concrete beams, Vanderbilt University.